Optimum Crashworthiness Design of Grid-Stiffened Composite Fuselage Structures

by

Mark David Sensmeier

Dissertation submitted to the faculty of the

Virginia Polytechnic Institute and State University

in partial fulfillment of the requirements for the degree of

DOCTOR OF PHILOSOPHY

in

Engineering Mechanics

O. Hayden Griffin, Jr., Chairman

Eric R. Johnson

Michael W. Hyer

Robert A. Heller

Scott L. Hendricks

September 1996

Blacksburg, Virginia

Keywords: Composites, Design, Fuselage, Grid-stiffened, Optimization

OPTIMUM CRASHWORTHINESS DESIGN OF GRID-STIFFENED COMPOSITE FUSELAGE STRUCTURES

by

Mark David Sensmeier

O. Hayden Griffin, Jr., Chairman

Engineering Science and Mechanics

(ABSTRACT)

In this study, a tool was developed for incorporating crashworthiness into the preliminary design of grid-stiffened composite fuselage structures. The crash analysis of a fuselage structure was simplified through the development of a global-local procedure, which reduces the computational requirements of a crash simulation while facilitating the calculation of local stresses. The method was implemented in concert with a progressive failure model to model the entire crash sequence, including failure events and subsequent response. Several examples were used to validate this method. This method was then implemented, along with simple models for assessing the ability of a fuselage to meet other load requirements, into a genetic algorithm optimization procedure. The resulting preliminary design tool permits a designer to optimize a fuselage for minimum weight, maximum crashworthiness or any combination of these parameters. An illustrative example was utilized to demonstrate the use of the tool for an aluminum fuselage as well as a composite fuselage. Several designs were found for both materials that substantially increased crashworthiness without a significant penalty on structural weight.

Acknowledgments

I would particularly like to thank my advisor Dr. O. Hayden Griffin, Jr., for encouraging me to return to graduate studies and for his valuable assistance during the course of this work. I would also like to thank Dr. Eric R. Johnson for his invaluable input and suggestions that guided the development of this project. I would like to thank Dr. Michael W. Hyer for agreeing to serve on my committee, and for my acceptance into the NASA-Virginia Tech Composites Program, which funded some of the early portions of this work. I would also like to thank Dr. Robert A. Heller and Dr. Scott L. Hendricks for agreeing to serve on my committee. Special thanks go to my parents, Dr. Paul and Susie Sensmeier, and to my in-laws, Jack and Ann Allison. Mostly, I would like to thank my wife, Laura, and my son, Steven, without whose patience, support, and escape, this work would not have been possible.

Table of Contents

List of Figures

List of Tables

1.0 Introduction and Objectives

1.1 Crashworthiness of Vehicle Structures

Perhaps since cavemen invented the wheel, vehicular accidents have been a part of human experience. As vehicle technology has progressed through the millennia from the wheel, to chariots, to horse-drawn wagons, to horseless carriages, to the modern automobile, to aircraft, and even to spacecraft, the vehicle system has become increasingly complex and the vehicle performance has improved dramatically. A nineteenth century collision between two Conestoga wagons was very unlikely to cause serious injury to the wagons' occupants due to the relatively slow speeds and low energies involved. However, a crash landing of a modern-day aircraft can occur at very high speed and correspondingly high energy. In order for even a fairly low-speed impact to be survivable for the occupants, the vehicle system must be designed in as crashworthy a manner as possible. Woodson[1] presented an excellent summary and literature survey of crashworthy design. The salient points of that discussion as they relate to the currently proposed project are summarized in this section.

Modern vehicles are typically very complex mechanical systems, involving many components which perform various functions towards the operation of that vehicle. Designing a vehicle for maximum crashworthiness can involve many different techniques applied to a number of these components with varying purposes and effectiveness. The U.S. Department of Defense has issued crashworthiness design standards for aircraft and helicopters. As part of these standards, five general "rules" for crashworthiness design are presented[2]:

Limit occupant accelerations - If the structure absorbs a sufficient amount of energy during a crash event, the resultant occupant accelerations (actually decelerations) can be kept below the limit which the human body can endure without serious injury or death.

Maintain a survivable occupant volume - The structure must be designed in such a way that during a crash event it will not collapse to the point where the occupant is injured or killed by the collapsing structure itself.

Retain high mass items - The attachments of large items, such as engines, stowage bins, etc. must be designed to remain attached during the crash event. Failure to do this could result in these massive items crashing into or through the passenger area causing significant distress to the occupants.

Minimize occupant environment hazards - Sharp and/or hard objects in the passenger compartment should be avoided or padded sufficiently so that collision with the passengers during crash is not overly harmful.

Minimize post-crash hazards - The use of highly flammable and toxic materials should be avoided in the design of the vehicle. Further, sufficient exit opportunities should be provided to facilitate passengers leaving a vehicle as quickly and safely as possible following a crash event. Many lives have been lost to otherwise survivable accidents because passengers were trapped in burning vehicles. Many of these fatalities are actually caused by exposure to toxic smoke rather than the fire itself.

The focus of the current effort was on the first of the above principles: limit occupant accelerations. By designing a structure to fail in a progressive manner in such a way as to maximize the amount of energy absorbed during impact, the acceleration experienced by the passengers (and the remaining structure and systems) can be kept to as safe a level as possible. This is the most critical of the five principles, as it is the first occurrence during the crash event and can have a substantial advantageous/deleterious effect on the remain-

der of the process.

During a crash scenario, the kinetic energy of motion of the vehicle is transferred, or absorbed, by deformation and failure of the vehicle structure. This can be expressed in a simple mathematical form as:

$$\int F(x)\,dx = \frac{1}{2}mV^2 \tag{1.1}$$

where F(x) is the stopping force, m is the mass of the vehicle, and V is the velocity of impact. The left-hand side of Eqn. (1.1) is essentially the area under the force-displacement curve of the failure process. Therefore, the goal of a crashworthy design is to maximize this area. However, an additional constraint arises as a result of Newton's Second Law:

$$F(x) = m \cdot a(x) \tag{1.2}$$

where a(x) is the acceleration of the vehicle. In order to maintain the occupant accelerations below a harmful level, the stopping force is constrained to stay below some critical value. Thus, maximizing the crashworthiness of a vehicle structure is accomplished by maximizing the energy absorbed by the structure (i.e. the area under the force-displacement curve), and at the same time keeping the peak stopping force below a critical value determined by the maximum amount of acceleration that the occupant can safely withstand

Since the focus of this effort was crashworthiness of aircraft, we must consider the parameters of a typical survivable aircraft crash. The key element here is the use of the

term survivable. Aircraft crashes which occur in a "head-on" manner, that is the aircraft nose collides with the ground or some other object, are almost always fatal; and the large energies combined with short stopping distances make these accidents virtually impossible to survive. Survivable crashes for most aircraft occur at relatively low flight speeds and low vertical descent rates[3]. Typically, a survivable crash scenario involves and aircraft moving in a forward and downward flight path while maintaining a relatively level aircraft attitude (e.g., +15° to -5° in pitch, 10° in ya w [2]). This situation is depicted schematically in Fig. 1.1. The key consideration for crashworthiness in this scenario is the vertical flight motion. Collision with the ground will result in a very short stopping distance with a correspondingly high vertical deceleration. Thus, the energy of vertical motion must be absorbed by the vehicle structure. The energy of forward motion will be less critical, as the aircraft will typically slide along the ground over a large distance, resulting in significantly lower deceleration. For this reason, this effort focused on the absorption of the energy of vertical motion.

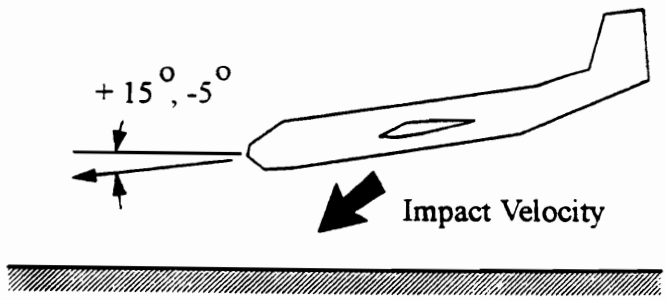

Figure 1.1 Typical survivable crash scenario [1]

To absorb this energy of vertical motion, aircraft rely on three primary structural mechanisms[2]. These mechanisms are (see Fig. 1.2):

- Stroking (deformation) of the landing gear
- Stroking of the seat support structure
- Crushing of the lower fuselage structure

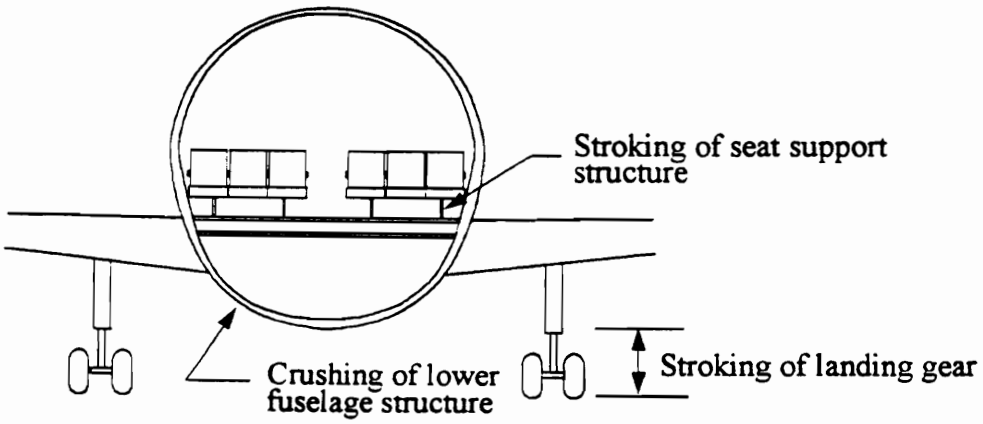

Figure 1.2 Mechanisms for energy absorption under vertical impact[1]

Designing the landing gear or the seat support structures is driven largely by the ability of these structures to handle the impact event. However, the fuselage structure, particularly the fuselage frames in a conventional skin-stringer design, are responsible for most of the strength and stiffness of the fuselage. Designing this structure for maximum crashworthiness is impossible without consideration of the other structural requirements of the fuselage. For this reason, this effort concentrated on the last of these mechanisms: crushing of the lower fuselage structure.

Woodson[1] considered the crushing response of composite skin-stringer fuselage assemblies. These composite fuselages are typically designed with stringers being thin-walled curved beams with an open cross section. These structures typically fail by brittle

fracture in the frames, resulting in the lower fuselage being broken into several segments[4]. This differs from conventional aluminum skin-stringer assemblies which absorb the impact energy by ductile yielding of the frame structures. This makes designing a crashworthy composite fuselage frame substantially more challenging than designing a crashworthy aluminum fuselage frame. The current effort focused on a fuselage structure reinforced with geodesic, continuous filament, stiffener geometries rather than the conventional circumferential stiffener frame-type structures. These types of structures will be discussed in the following section.

1.2 Grid-stiffened Fuselage Structures

Aircraft fuselage structures have typically been skins stiffened with open-section stiffeners. For metallic aircraft, this results in a lightweight, efficient fuselage. As composite materials began to see use in primary aircraft structures, similar designs were utilized. However, constructing composite fuselages and assembling the stiffeners with fasteners is generally not cost-effective and can lead to other design difficulties in the attachment areas. The idea of grid-stiffened structures, utilizing advanced filament-placing technology and co-curing of the grid-stiffeners to the skin, led to the development of new manufacturing processes. The Lockheed-Georgia Company developed a process to fabricate grid-stiffened fuselages with continuous-filament stiffeners[5]. This method was based on earlier pioneering work by McDonnell Douglas Astronautics Company, St. Louis, in utilizing stylus weaving to produce grid-stiffened flat panels[6].

The various types of grid-stiffener arrangements can be divided into three categories:

1. Orthogrid - All stiffeners are oriented either longitudinally (in the direction of

the fuselage axis) or circumferentially. In general, the size and spacing of the stiffeners in each direction may be different. This *general orthogrid* is illustrated in Fig. 1.3.a. If the stiffener spacing and sizes are uniform, the result is a special case of the general orthogrid, which for the purposes of this report shall betermed a *regular orthogrid* (see Fig. 1.3.b). Obviously, the conventional skin-stringer monocoque fuselage design is just a special case of a general orthogrid where the stiffeners are larger and spaced much farther apart than a typical continuous-filament orthogrid.

2. *Spiral grid* - Stiffeners are wound at an angle to the axial and circumferential directions. An example of a typical spiral grid is illustrated in Fig. 1.3.c. Typically, two orientations of stiffeners, each at equal and opposite angles from the orthogonal directions are utilized.

3. *General grid* - The above two classifications are actually just special cases of a general grid configuration. This is illustrated in Fig. 1.3.d. Practically all of the grid arrangements that have been considered are just special cases of this general grid. By considering each of the stiffener geometries and spacings to be a design variable, a huge assortment of grid-reinforcement designs can be generated. Reducing the size of a given grid section to zero (effectively eliminating that section) can result in even more available grid designs.

1.2.1 Isogrid

One special case of the general grid configuration that deserves special mention is the *isogrid*, which was developed by Dr. Robert R. Meyer of the McDonnell Douglas Astronautics Company-West in 1964[6]. The isogrid concept utilizes a repeating pattern of equilateral triangular stiffener configurations as shown in Fig. 1.4.a. To illustrate that this is just a special case of the general grid, the sections of the general grid which are kept in the isogrid are shown darkened in Fig. 1.4.b. In a global sense, an isogrid responds in a similar way as an isotropic material. This is the reason for the use of the prefix "iso-". [7].

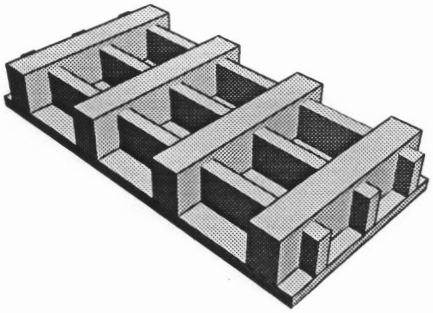

(a) General orthogrid

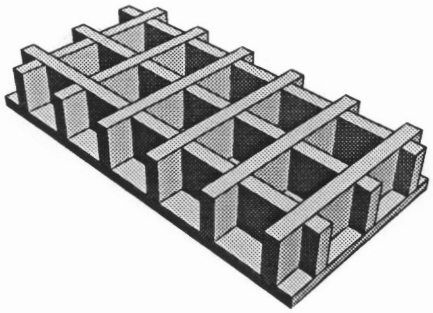

(b) Regular orthogrid

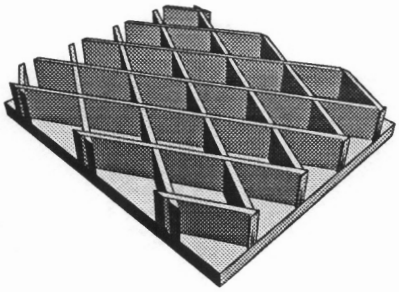

(c) Spiral grid

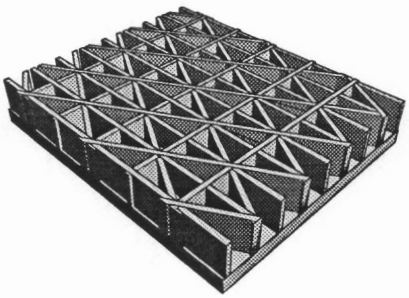

(d) General grid

Figure 1.3 Grid-stiffener configurations

Isogrids have an inherent advantage over orthogrids in that the isogrid configuration is stable. Therefore, the isogrid-stiffened structure does not rely on the skin to help maintain its shape in the way that the orthogrid-stiffened structure does. Isogrids also offer another distinct advantage. Due to its highly redundant nature, isogrid stiffening results in a very damage-tolerant structure[8]. Loads from locally-failed stiffeners are easily transferred to neighboring stiffeners. This ability to shift the load path allows the isogrid-stiffened structure to suffer numerous local damage events prior to a large drop in the global load-carrying capacity.

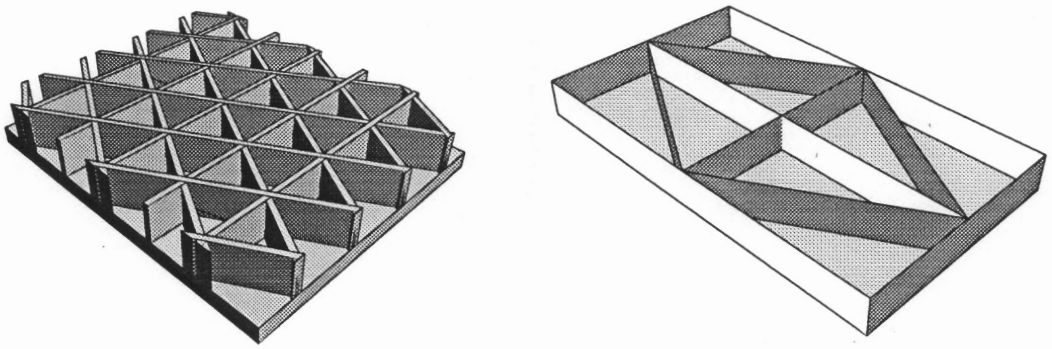

(a) Isogrid concept

(b) General grid unit cell with isogrid components shaded

Figure 1.4 Isogrid stiffening configuration

1.2.2 Design studies

Several investigators have performed design studies to attempt to determine which types of grid-stiffening offer the most promise. Hofmeister and Felton[9,10] studied a number of stiffening patterns, mostly variations on the orthogrid and isogrid concepts. Their study considered flat plates subject to uniaxial and biaxial compressive loads. The unique aspect of their design study was the use, in some cases, of a secondary reinforcement pattern of larger stiffeners spaced much farther apart than the smaller primary stiffeners. They utilized a minimization procedure to determine minimum-weight designs subject to buckling and yield constraints. The isogrid-type stiffener design was found to exhibit the most promise, and waffle plates with two sizes of ribs were found to be more efficient than those with a single stiffener size.

A study of spiral-type stiffened cylindrical shells by Pappas and Amba-Rao[11] showed that spirally stiffened shells may be quite inferior to orthogrid stiffened shells. They also concluded that local failure modes must be considered in any design analysis.

More recently, Reddy *et al* [5] performed design studies on isogrid, orthogrid and generalized orthogrid fuselage structures. They considered load cases of uniaxial compression and combined axial compression and torsion, and sought to minimize weight subject to constraints on general instability, rib crippling, and skin buckling. All three design concepts were found to be weight competitive. They concluded that the isogrid concept was the most attractive largely as a result of its superior damage tolerant nature.

1.3 Objectives

The primary objective of the current effort was to provide a preliminary design tool which would allow an aircraft designer to more effectively determine an optimum grid-stiffener configuration incorporating crashworthiness as a design criterion. The key element is the preliminary design motivation. It would certainly be possible to perform a detailed, non-linear dynamic analysis of a grid-stiffened fuselage to predict as exactly as possible the response during typical crash events. However, that approach, while it may provide some understanding into the crashworthiness of grid-stiffened fuselage structures, would not ultimately provide aircraft designers with a usable tool for their practice. This would contribute to what Haftka[12] terms the *"chasm between vigorous progress in research and development of new methods and relatively slow assimilation of these new methods in industrial practice."*

In addition to the motivation to provide designers with usable tools, there were other reasons for concentrating on the preliminary design stage. Aircraft are often designed with the primary flight loads and conditions governing the chosen design. Crashworthiness aspects are of second order consideration or added as an afterthought. By introducing

crashworthiness as a design criterion in the preliminary design phase, fuselage structures can be selected which, in addition to meeting all of the standard design criteria, are as crashworthy as is feasible given these other constraints.

In addition to the motivation for a preliminary design tool, there was a distinct need for a tool with direct application to grid-stiffened fuselage frames. Woodson[1] considered the similar problem for a composite fuselage frame, but with a conventional reinforcement configuration. A number of researchers have performed detailed analyses of the nonlinear postbuckling response of grid-stiffened structures (see Sec. 2.2). The vast majority of these analyses have looked primarily at axial or torsional loading of grid-stiffened cylinders. This type of loading, while of an interesting research nature, is not of direct interest for the type of survivable crash considered in this effort. There appeared to be a noticeable void in the body of available methods and printed literature for a preliminary design tool to optimize the crashworthiness of grid-stiffened fuselage structures.

2.0 Analysis and Design of Crashworthy Aircraft Structures

In Chapter 1, the fundamentals of aircraft crashworthiness and grid-stiffened fuselage structures were discussed, and objectives for the current effort were presented. In order to develop the preliminary design tool put forward in that description, it was first necessary to review the pertinent literature covering analysis and design of crashworthy aircraft structures. Again, Woodson[1] provides an excellent review of existing analysis methods, both for metallic structures as well as for composites. Rather than duplicate the literature review effort he put forward, it was decided to focus on literature covering specific analysis methods which were of potential use in the current effort. The results of this survey are presented in this chapter. After a brief discussion of the limitations of the available analysis tools as they apply to the problem of grid-stiffened composite structures, there follows summaries of literature covering buckling and postbuckling of stiffened panels or shells, energy absorption under progressive failure analysis of composite structures, and optimized design of fuselage-type structures.

2.1 Crashworthiness Analysis Methods

There are a number of existing analysis tools for crash simulation in use today. They range from the very computationally demanding non-linear dynamic finite element codes, such as DYCAST[13], DYNA3D[14], ANCS[15] and others, to the semi-empirical codes such as KRASH[16]. In between these two extremes are the traditional crush analysis models, which incorporate collapse through the use of "rivets"[17] or plastic hinges which fail at a prescribed load.

The detailed finite element codes have been applied with good success to a number of crash scenarios in many different vehicle structures. In the area of aircraft fuselages, Winter *et al*[18] used an early version of DYCAST to simulate a crash of both composite and aluminum helicopters. Composite energy absorption was included primarily through tube crushing in the fuselage subfloor. More recently, Jackson *et al*[19] have used both KRASH and DYCAST to model the crash responses of composite aircraft and helicopter fuselage sections. They were able to demonstrate the ability of these numerical tools to accurately simulate crash response and energy absorption capabilities for these types of structures. Further application of these methods for aircraft crash analysis can be found in the works of Hayduk *et al*[20], Haug *et al*[21], Tennyson and Hansen[22], Logan *et al*[23] and Thomson and Goetz[24] among others. Hansen and Tennyson[25] even used this approach to analyze a stiffened composite structure, although the stiffeners were limited to the stringer-type. While these investigations showed the promise of the finite element approach for simulating crashes, it is clear that this method is not feasible in the modern computing environment to incorporate this approach into a realistic optimization scheme.

The simpler lumped mass-spring type analyses have also been demonstrated with some success in simulating crashes of aircraft structures. For example, Wittlin and Caiafa[26] used KRASH85, an updated version of KRASH, to perform preliminary analysis of a fuselage. Bolukbasi[27] used KRASH to study the crash characteristics of a helicopter. This approach, while computationally simpler than the finite element approach described above, is better suited for a systems approach to crashworthiness. That is, constructing models of an entire structural system or vehicle and performing a dynamic crash simulation. Although this method could have been applied in the preliminary design sys-

tem in this project, it would have been difficult to accurately represent the grid-stiffener configurations expected.

The crush analysis approach has also been applied successfully to aircraft structures. Work by Murray[17] and Toi and Yang[28] among others have demonstrated their capability. By adding "rivets", or plastic hinges, to represent collapsing structural elements, this method can model the crushing of a structure without the intense computational requirements of the detailed non-linear finite element approach. If the current project involved only ductile metallic structures, this might have been the analysis tool of choice. However, the plastic hinge models are not suited well for analysis of composite structures which are expected to fail in a brittle, discrete manner.

2.2 Buckling and Postbuckling of Stiffened Panels

The work described in this section deals with the buckling and postbuckling analysis of stiffened panels and shells. For non-stiffened plates and shells, including composite materials, the analysis tools for buckling loads are well known and readily available[29]. Methods for postbuckling analysis of isotropic non-stiffened structures are also easily found. Zhao *et al*[30], for example, present a method based on the principle of minimum potential energy to determine the postbuckling response of end-loaded elastically supported columns. The postbuckling analysis of composite plates, however, has received less attention. Buskell *et al*[31] performed a series of postbuckling tests on composite panels and demonstrated substantial postbuckling strength, as much as twice the initial buckling load. Shin *et al*[32] used energy methods to obtain the postbuckling response of composite plates under axial compressive loading. They utilized their method to study the effect of bend-twist coupling on the response and showed examples for isotropic, orthotropic and

anisotropic plates. Kweon and Hong[33] used an arc-length method based on nonlinear finite elements to perform postbuckling analysis of cylindrical composite panels. Their finite element results show generally good agreement with experimental data.

Many investigators have considered both buckling and postbuckling of stiffened plates and shells as well. Jones[34] provided some pioneering work in the area of buckling of composite circular cylindrical shells with eccentric stiffeners. Using a Donnell-type shell theory along with classical stability theory, he was able to predict buckling loads without the erratic results of previous approaches which had neglected the coupling between bending and extension. Soong[35] used an averaging scheme to extend this work by studying the buckling of orthotropic cylindrical shells with spiral stiffeners. Soong showed good agreement with experimental data for waffle cylinders, and demonstrated that spiral-type stiffening might be stronger than conventional stiffening of equal weight. Steen[36] used an energy approach to extend the study of eccentrically stiffened plate to the postbuckling regime.

Sheinman and Frostig[37] used a combination of eigenfunction series expansion and finite differences to solve the equilibrium equations in terms of out-of-plane displacements and Airy stress functions of the buckling and postbuckling analysis of a curved, stiffened laminate panel. Not only did the analysis show good agreement with more detailed solutions, it was also found to be very computationally efficient when compared with finite element analyses. Wu and Zhang[38] analyzed a similar problem using virtual work for the buckling analysis and Huchinson's criterion for the postbuckling bifurcation analysis. Their model also included nonlinear material behavior (elastic-plastic behavior), transverse shear and initial imperfections. They also found good agreement with experimental

data and other known solutions.

Yoda and Atluri[39] developed a higher-order shear deformation theory and derived a displacement field which eliminates the need for the standard shear correction factors. They then applied the theory to postbuckling analysis of stiffened composite panels under compression using a finite strip method with finite element analysis. This approach was then validated with typical experimental results.

Several researchers have attempted to develop simplified analytical expressions. One particularly simple approach was developed by Moradi and Parsons[40] to predict the buckling load of stiffened composite shells. They utilized dimensional analysis with Donnell shell theory assuming smeared stiffeners (axial and ring). This particular approach, although lacking in detailed response information is well suited to preliminary design use.

Sherbourne and Bedair[41] used a numerical Ritz-type solution with minimization of total potential energy to predict the postbuckling behavior of plate-stiffener assemblies under axial compression. They developed analytical expressions for the strain energy for plates of different aspect ratio under a variety of boundary conditions.Boitnott *et al*[42] simplified the nonlinear problem by investigating the postbuckling and failure response of a pressurized composite panel. They developed a one-dimensional nonlinear model based on a shear deformable shallow shell theory with an approximate set of strain-displacement relations, then derived closed-form solutions. Using the general purpose shell finite element code STAGS, regions of the panel where the one-dimensional model was applicable were selected. Good correlation between analytical and experimental results required very accurate measurements of panel curvature and accounting for specimen slippage.

The previous analytical works all use a homogenization of the stiffener geometry to

perform the buckling and postbuckling analysis. The analytical method has been extended to model discrete stiffeners through the use of the finite strip method. Dawe *et al*[43] used a finite strip method in conjunction with an iterative Newton-Raphson procedure to predict post-local-buckling of stiffened panels under the same loading. They considered both classical plates as well as shear deformable plates. Several applications were demonstrated, including box- and hat-sections and blade-stiffeners. For a laminated box beam, good correlation with the results from the commercial finite element package LUSAS was obtained. Loughlan[44] applied a similar finite strip method to analyze the shear buckling of composite panels.

For complex geometries and analyses where local failure modes are important, finite element analysis serves as a useful analysis tool. Scott[45] demonstrated the capability of the general purpose finite element code MSC/NASTRAN for modeling buckling and postbuckling behavior of stiffened composite plates. This included a study of the effects of imperfection on the nonlinear response. Good correlation between the buckling predictions and the bifurcation point of the nonlinear analysis was achieved. However, Scott[45] concluded that "the prediction of postbuckling performance requires both specialist modeling skills."

Falzon and Steven[46] performed a nonlinear analysis using an Australian finite element package, Strand6, to predict the buckling and postbuckling response of a hat-stiffened composite plate. Strand6 used a co-rotational large rotation formulation with an incremental approach.They achieved good correlation between the predicted nonlinear response and experimental results.

Renze and Laananen[47] used the general purpose finite element code PATRAN to

predict the buckling load of bead-stiffened composite panels under uniaxial compression. A bead-stiffened panel consists of stiffeners which are formed integrally with the panel. Through a parameter study, Renze and Lannanen[47] determined that the bead height, bead corner radius, and panel size had the most substantial effects on the predicted buckling load. They then developed closed-form solutions for the buckling load which bound the results from the finite element analysis.

In an effort to reduce the computational cost of finite element analysis while still incorporating local effects, Chen *et al*[48] developed an approach for predicting buckling loads of orthogonally stiffened composite panels by limiting the analysis to the study of one or two individual cells. They show good agreement between these simpler analyses and buckling analyses of full structures. This type of approach has some promise for application to non-orthogonal grid buckling analysis.

Virtually all of the methods discussed above are limited to stiffeners parallel or perpendicular to the axis of a cylinder or direction of loading in a panel. Fewer references have been found on the subject of buckling or postbuckling analysis of geodesic-type stiffener configurations. The complex geometry of these types of structures generally make an analytical solution difficult and often require detailed finite element models. Much of the pioneering work in this area has been done by Sandhu[49]. This application of finite elements is clearly not suitable for application in a preliminary design optimization environment.

Although a detailed finite element solution for postbuckling is not useful in the proposed preliminary design tool, an item of particular interest to this effort has been investigated using finite element analysis. This issue is joint flexibility. In any stiffened structure

where stiffeners intersect, modeling this flexibility could have a significant effect on the ability to accurately predict the response. Sandhu *et al*[50] compared experimental data with finite element results for torsional buckling and postbuckling of geotectonically-reinforced composite cylinders and found that joint flexibility was a significant factor. Depending on the amount of expected "scissoring" at the joints, their finite element models were overstiff by from 10-15% (low scissoring) to as high as 70% (high scissoring). Two methods were proposed to add joint flexibility to the finite element model. The first method is to reduce the local bending stiffness near the joint. This method is arbitrary and, further, was not shown to be effective. The second method was to offset intersecting stiffeners and connect the offset nodes with a torsional beam element. This method produced significantly better correlation. Although selecting the torsional stiffness of the joining beams is still arbitrary, any finite value provides a better result than the rigid joint analysis.

Several methods for approximating, or "smearing", the stiffener effects have been presented. Analytical methods for calculating the stiffness of a regularly non-homogeneous corrugated surface are presented by both Parton and Kudryavtsev[51] and Kalamkarov[52]. A number of researchers have attempted to predict the buckling load of waffle-grid stiffened panels and cylinders. These models have in common the smearing of the stiffener effects over the shell reference surface.

Meyer[53] provided an early model for 45° eccentric-stiffened cylinder buckling. He assumed that a uniaxial stress prevails in each rib and developed closed-form expressions for buckling load, obtaining good agreement with experimental data. Lee and Lu[54] extended this analysis to consider variable orientation stiffeners and used a Ritz-type solution to predict the bending instability of a stiffened cylinder. Agreement with experimental

results was not as good, and the authors hypothesized that initial imperfections in the specimens led to the lack of correlation.

Hofmeister and Felton[9] present a method for prediction of buckling of waffle plates with different size ribs in each stiffening direction. Again, the ribs are smeared, and the minimization of total potential energy was used to derive the buckling relations. They achieved good agreement with other published solutions. Hayashi[55] presents a similar method and attempts to include the effects of joint flexibility through the shear rigidity of the skin. Rehfield *et al*[56] extend this type of theory to include non-classical effects of transverse shear and variation of axial stresses in the ribs. They obtain good correlation with experimental results.

A plastic-hinge type approach was proposed by Slysh *et al*[57]. The predicted beam-column buckling response for isogrids is used in this approach. Cylinder buckling analysis consists of modelling the instability of two tandem longitudinal grid members which are fixed together through linear and torsional springs. Additional models are used to determine the spring constants. Design knockdown figures were obtained from the model and agreed well with test results.

The problem of postbuckling of non-orthogonal grid-stiffened plates and shells has received even less attention than the similar buckling problem. However, recent advances in this area have provided some useful models. Zhimin *et al*[58] used a Ritz method for the nonlinear postbuckling analysis of composite cylinders with isogrid stiffening which includes the effects of initial imperfections. The solution is obtained numerically, but good agreement is obtained with test data using less computational resources than in the finite element method.

Recently, the Lagrange multiplier technique[59] has emerged as a promising tool for buckling and postbuckling analysis of geodesically-reinforced composite shells. The Lagrange technique applies a set of constraint equations which impose an out-of-plane deflection continuity along the skin-stiffener interface. This allows for the incorporation of discrete stiffener effects without the associated computational burden. Phillips and Gürdal[60] used this method to analyze geodesically stiffened panels subjected to inplane loads, and Gendron[61] then used the method to analyze geodesically stiffened composite cylinders subjected to axial compression and/or torsion.

2.3 Progressive Failure and Energy Absorption of Composite Structures

Progressive failure models for metallic structures focus on the elasto-plastic response character of most metals. For this reason, these models are generally not capable of handling the discrete load drops exhibited by composite materials during the failure process. Most of the progressive failure models for composites deal primarily with the failure of individual laminae within a laminate and the effects of these failures on the subsequent laminate behavior. Typically, the elastic constants of a failed ply are degraded by some arbitrary factor, then the laminate constitutive expressions are recalculated using these degraded properties[62]. While this approach often yields good correlation to experimental failure results and can be incorporated into the analysis of general structures, it becomes very cumbersome for more complex structures. An example of successful application of this method to a simple structure (uniaxially-loaded plate with a central hole) is presented by Chang and Chang[63]. By incorporating the lamina failure / property degradation method into a finite element code, they demonstrated the prediction of propagating damage away from the hole and determination of the ultimate strength of a plate with a

hole. More recently, Tolson and Zabaras[64] developed and applied a similar method based on a shear deformable plate theory to predict first ply failure (FPF) and last-ply failure (LPF) of a composite laminate.

While this method was suitable for a fairly simple analysis, its use in a general structure suggests other problems. Composite materials often suffer a number of minor matrix-related failure events prior to any significant loss of load-carrying capability. In an analysis of a complex structure, significant computational time could be expended on predicting and propagating relatively meaningless failure events. One promising remedy to this difficulty is a semi-empirical approach proposed by Bolukbasi and Laananen[65]. Combining classical laminated plate theory, elastic stability theory, and experimental nondimensional crippling data for composite stiffeners[66], they predict the energy absorption capabilities for different stiffener cross-sections. Good correlation is achieved between predictions and experimental data. However, the semi-empirical nature of this approach precludes its application to other material systems or laminate configurations without additional test data.

2.4 Design Optimization of Stiffened Composite Structures

As stated in Sec. 1.3, a motivation for the current research effort was to incorporate crashworthiness optimization into the preliminary design stage of an aircraft (or other vehicle). This needed to be done within the context of current preliminary design criteria. Ideally, the crashworthiness criterion would be inserted as an additional "module" to a current integrated design system. Hall[67] and Hall and Simpson[68] have assembled such an integrated system for advanced composite structures. Individual tools for analyzing interlaminar stresses, local/global buckling, mechanical and adhesive joints, environmen-

tal effects, and fatigue and damage tolerance have been merged into a single computer package. The vision for the proposed tool was to incorporate the crashworthiness estimation as an additional module to this type of design system, with an optimization scheme encompassing the entire system.

2.4.1 Optimization for Crashworthiness

Although structural optimization techniques[69] are often used in the preliminary design stage for many structures, crashworthiness is not usually incorporated into the process. Bennet *et al*[70] and Song[71], among others, have proposed methods for combining optimization with crashworthiness in the automotive industry.

Sen[72] performed tests to determine the energy absorbing capabilities of various composite subelements, then incorporated these results as building blocks in an overall helicopter design for crashworthiness. Bolukbasi[27] enveloped an optimization scheme around a combination of aircraft crash response analysis and a subsystem analysis for rotorcraft design. This system/subsystem approach is able to select a design for a helicopter with minimum weight given a crashworthiness standard. Both of these approaches utilize a potentially semi-empirical approach where the overall vehicle system is considered as a combination of individual subelements. These subelements can be analyzed separately, or experimental data can be used to represent their energy absorbing capabilities. Kecman *et al*[73] discuss a similar system analysis of energy absorption and load distribution for the design of various vehicles, including buses, cars, aircraft and railways. Lust[74] presents, in a more mathematical fashion, the optimization problem showing that more efficient designs can be obtained if crashworthiness is considered simultaneously with other design constraints rather than incorporated after the design has been fixed.

Lust[74] follows the building block approach as well, where each subcomponent is considered separately and then becomes a part of the system spring-mass-damper assembly. Sadeghi[75] adds yet another voice to the chorus of researchers and designers calling for incorporation of crashworthiness into the preliminary design optimization effort. His demonstration of this involved a database of empirical test data used in conjunction with coarse finite element idealization to model the collapse of an automobile

Given the intense media attention on aircraft crashes, the increased use of crashworthiness as an advertising point for automobiles, and the recent rash of railway accidents[76], there is likely to be a continued push for incorporation of crashworthiness as a fundamental part of the design process.

2.4.2 Optimization of Stiffened Plates and Shells

The range of optimization techniques available for stiffened plates and shells varies, just as in most other areas, from simple "brute-force" methods to the use of an existing optimization code to the relatively new genetic algorithm method. An excellent survey of the development of methods for stiffened plate and shell optimization is presented by Butler *et al*[77].

An example of the "brute force" method of optimization applied to stiffened composite shells is presented by Tripathy and Rao[78]. Using the finite element method for a linear buckling analysis of an axisymmetric composite shell, they computed the buckling load for every possible layup scheme within their selected design regime. Optimization is then accomplished by simply ranking the buckling loads for several cases of shells (axially compressed cylindrical shell, pressurized conical shell, pressurized clamped spherical cap, and axially compressed ring and stringer stiffened cylinder). Obviously, this method is

only of any interest for situations where the number of possible design variations is fairly small, or could be limited by some other method.

A number of existing codes are available that can be applied to optimization of stiffened panels. Butler *et al*[77] discuss several of these, including VICONOPT[79], PASCO[80] and PANDA[81]. Most of these codes consider a variety of design constraints, including buckling, postbuckling, stiffness and weight. Most of them are capable of analyzing composites with stiffeners. The most promising of these codes is PANDA, which is described in some detail by Bushnell[81]. PANDA is capable of incorporating constraints such as general instability, panel instability, local skin buckling, local crippling of stiffeners and stiffener rolling. PANDA utilizes CONMIN[82], a nonlinear constrained search algorithm to find the optimum design given an initial design concept and design parameters supplied by the user.

Phillips and Gürdal[60] used another optimization code, ADS[83] to determine a minimum weight design for geodesically stiffened composite panels subjected to inplane loads. The geodesic stiffeners were incorporated through a Lagrange multiplier technique[59] which imposes an out-of-plane deflection continuity along the stiffener skin interface. Gendron[61] then followed a similar approach to optimize the design of a geodesically-stiffened composite cylinder subjected to axial compression and/or torsion. Although this approach could have been applied to the problem considered in this project, it requires that a mesh be developed for the full structure for each possible design variation. Thus, it is much more difficult to consider a wide variety of stiffener configurations than using the approach defined in Sec. 4.4.

Yet another optimization process that can be applied to stiffened composite structures

is the genetic algorithm[84]. The genetic algorithm is based on a natural selection and reproduction process wherein the optimum design improves through generation of successive generations. Haftka and Gürdal[68] give an excellent summary of the genetic algorithm and its application to composite laminate design optimization. The genetic algorithm requires that the structural analysis be performed a large number of times, thus requiring a computationally limited analysis method. Kogiso *et al*[85] suggest some methods for reducing the number of analyses required in a genetic algorithm: a binary tree to store previous designs, and a local improvement scheme. Nagendra *et al*[86] have demonstrated improvements to the genetic algorithm approach for the design of stiffened composite panels. Another recent work by Rao[87] discusses methods for handling multiple criteria design with genetic algorithms. This was important in the current project, as weight and crashworthiness were both be treated as design criteria, or objectives.

3. Development of Global-Local Finite Element Approach

3.1 Introduction and Motivation

As stated in Sec. 1.3, the primary objective of this study was to develop a preliminary design tool to aid in the optimum design of grid-stiffened fuselage structures with crashworthiness constraints. This tool was to be based on approximate analytical methods to enable the computational efficiency required by the multiple analyses usually performed during the preliminary design phase. However, the nature of grid-stiffened structures, particularly isogrid, leads to a very nonuniform response field. That fact, along with the incorporation of local failure modes (necessary to accurately gauge the energy absorption characteristics of these structures), required an analysis method more sophisticated than a smeared-properties approach. To overcome these conflicting requirements, a global-local analysis approach was implemented. The approach is illustrated schematically in Fig. 3.1.

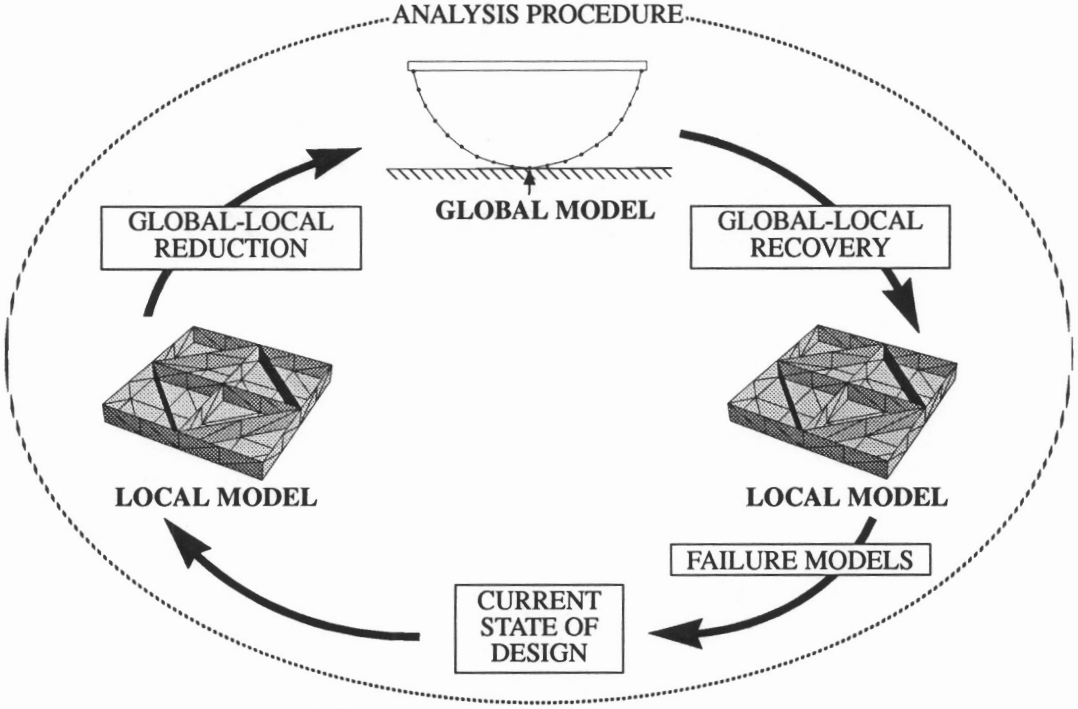

Figure 3.1 Schematic of the global-local analysis procedure

As is shown in the figure, there are three key features to the global-local design tool: a local model which incorporates the necessary details of the grid-stiffener configuration, a global model which utilizes a reduced-order version of the local model, and an optimization scheme which is used to determine and evaluate the best design given parameters input by the designer. The remainder of this chapter describes each of these features in detail, along with a summary of the selected approach for the necessary models.

3.2 Local Model

The purpose of the local model is to provide an analysis method which incorporates the necessary structural details of a particular grid-stiffening configuration, including the overall structural response, the local failure modes, and the effect of damage on subsequent behavior.

In order to accurately represent the behavior of a small, detailed portion of a grid-stiffened structure and predict both the occurrence of local failure events and their effect on the subsequent response, a fairly detailed local model was required. Due to the complex geometry of this structure, the finite element method was chosen as the analysis tool. It would have been natural to model this three-dimensional structure using three-dimensional solid elements. However, the computational requirements of such a detailed model are not justified given the preliminary design nature of this project. Since the grid components consist of a fairly thin composite skin with primarily blade-type stiffeners, a shell (or plate) type finite element method was selected. By building up the various skin and stiffener details using shell (or plate) elements, all of the above requirements for the local model were met.

These shell (or plate) elements, while two-dimensional in a finite element sense, can

be used to accurately represent the three-dimensional nature of the structure. Clearly, this approach used a simplification of the details of the skin-stiffener attachments, stiffener geometries, and stiffener intersections. These details could have been incorporated by using three-dimensional solid elements in a manner similar to that used by Hyer and Cohen[88] to calculate the local stresses at the skin-stiffener interface in stiffened composite panels. However, since the purpose of this effort was preliminary design optimization, it was anticipated that the simplifications inherent in the use of plate elements would yield results accurate enough to allow good comparisons of energy absorption in different design configurations.

The fuselage structure is essentially cylindrical. This fact would suggest the use of curvilinear shell elements. An abundance of shell elements are available in existing finite element codes and in the literature. Excellent summaries of shell finite element approaches are given by Morris[89] and Scoredelis and Lo[90]. A linear cylindrical shell element was presented by Bogner, *et al*[91] and numerous other investigators have presented various modifications to this type of element. However, many researchers have also used an alternate approach by modeling shell structures as an assemblage of flat plate elements. Although this method uses an approximate representation of a true curvilinear surface, it often is more computationally efficient than using a true shell element[92]. This approach is accurate as well, particularly for surfaces with only a mild degree of curvature.

Another important consideration in the selection of a finite element for the local model was the inclusion of transverse shear deformation. It is well known that the effects of transverse shear on composites can be significant. This is particularly true for thick composites. The stiffeners used in a grid-stiffened structure could be fairly thick relative to the

other dimensions of the grid segments. Thus, it was decided to use a shear deformable element in the local model. Including these transverse shear effects in shell theory yields a very complex set of equations. However, shear deformable plate elements, even for composite laminates, have been used extensively and are much easier to formulate. For this reason, a shear deformable plate element was selected as the basic building block for the local model[93]. A hybrid plate element with both inplane and bending effects was constructed.

The equilibrium equations for a shear deformable plate are:

$$\begin{aligned}
\frac{\partial N_x}{\partial x} + \frac{\partial N_{xy}}{\partial y} &= 0 \\
\frac{\partial N_{xy}}{\partial x} + \frac{\partial N_y}{\partial y} &= 0 \\
\frac{\partial Q_x}{\partial x} + \frac{\partial Q_y}{\partial y} + q &= 0 \\
\frac{\partial M_x}{\partial x} + \frac{\partial M_{xy}}{\partial y} - Q_x &= 0 \\
\frac{\partial M_{xy}}{\partial x} + \frac{\partial M_y}{\partial y} - Q_y &= 0
\end{aligned} \tag{3.1}$$

where: N_x, N_y and N_{xy} are the inplane force resultants; M_x, M_y and M_{xy} are bending moments; Q_x and Q_y are transverse forces; and q is the out-of-plane distributed force.

For a general, laminated composite plate, the constitutive relationships for inplane force resultants are given by:

$$
\begin{aligned}
N_x &= A_{11}\frac{\partial u}{\partial x} + A_{12}\frac{\partial v}{\partial y} + A_{16}\left(\frac{\partial u}{\partial y} + \frac{\partial v}{\partial x}\right) + B_{11}\frac{\partial \theta_y}{\partial x} - B_{12}\frac{\partial \theta_x}{\partial y} + B_{16}\left(\frac{\partial \theta_y}{\partial y} - \frac{\partial \theta_x}{\partial x}\right) \\
N_y &= A_{12}\frac{\partial u}{\partial x} + A_{22}\frac{\partial v}{\partial y} + A_{26}\left(\frac{\partial u}{\partial y} + \frac{\partial v}{\partial x}\right) + B_{12}\frac{\partial \theta_y}{\partial x} - B_{22}\frac{\partial \theta_x}{\partial y} + B_{26}\left(\frac{\partial \theta_y}{\partial y} - \frac{\partial \theta_x}{\partial x}\right) \\
N_{xy} &= A_{16}\frac{\partial u}{\partial x} + A_{26}\frac{\partial v}{\partial y} + A_{66}\left(\frac{\partial u}{\partial y} + \frac{\partial v}{\partial x}\right) + B_{16}\frac{\partial \theta_y}{\partial x} - B_{26}\frac{\partial \theta_x}{\partial y} + B_{66}\left(\frac{\partial \theta_y}{\partial y} - \frac{\partial \theta_x}{\partial x}\right)
\end{aligned}
\tag{3.2}
$$

where: u, v, and w are the displacements; θ_x and θ_y are the rotations; A_{ij} is the inplane stiffness matrix; B_{ij} is the coupling matrix; and D_{ij} is the bending stiffness matrix. The constituve relations for bending moments are:

$$
\begin{aligned}
M_x &= B_{11}\frac{\partial u}{\partial x} + B_{12}\frac{\partial v}{\partial y} + B_{16}\left(\frac{\partial u}{\partial y} + \frac{\partial v}{\partial x}\right) + D_{11}\frac{\partial \theta_y}{\partial x} - D_{12}\frac{\partial \theta_x}{\partial y} + D_{16}\left(\frac{\partial \theta_y}{\partial y} - \frac{\partial \theta_x}{\partial x}\right) \\
M_y &= B_{12}\frac{\partial u}{\partial x} + B_{22}\frac{\partial v}{\partial y} + B_{26}\left(\frac{\partial u}{\partial y} + \frac{\partial v}{\partial x}\right) + D_{12}\frac{\partial \theta_y}{\partial x} - D_{22}\frac{\partial \theta_x}{\partial y} + D_{26}\left(\frac{\partial \theta_y}{\partial y} - \frac{\partial \theta_x}{\partial x}\right) \\
M_{xy} &= B_{16}\frac{\partial u}{\partial x} + B_{26}\frac{\partial v}{\partial y} + B_{66}\left(\frac{\partial u}{\partial y} + \frac{\partial v}{\partial x}\right) + D_{16}\frac{\partial \theta_y}{\partial x} - D_{26}\frac{\partial \theta_x}{\partial y} + D_{66}\left(\frac{\partial \theta_y}{\partial y} - \frac{\partial \theta_x}{\partial x}\right)
\end{aligned}
\tag{3.3}
$$

and the constitutive relations for shear forces are:

$$
\begin{aligned}
Q_x &= kA_{45}\left(\frac{\partial w}{\partial y} - \theta_x\right) + kA_{55}\left(\frac{\partial w}{\partial x} + \theta_y\right) \\
Q_y &= kA_{44}\left(\frac{\partial w}{\partial y} - \theta_x\right) + kA_{45}\left(\frac{\partial w}{\partial x} + \theta_y\right)
\end{aligned}
\tag{3.4}
$$

where k is the shear correction factor.

These constitutive relations (Eqns. 3.2 to 3.4) were substituted into the equilibrium equations (Eqns. 3.1). A standard finite element formulation was then applied, resulting in

a system of equations of the form:

$$\begin{bmatrix} K_{11} & K_{12} & 0 & K_{14} & K_{15} & 0 \\ K_{21} & K_{22} & 0 & K_{24} & K_{25} & 0 \\ 0 & 0 & K_{33} & K_{34} & K_{35} & 0 \\ K_{41} & K_{42} & K_{43} & K_{44} & K_{45} & 0 \\ K_{51} & K_{52} & K_{53} & K_{54} & K_{55} & 0 \\ 0 & 0 & 0 & 0 & 0 & K_{66} \end{bmatrix} \begin{bmatrix} u \\ v \\ w \\ \theta_x \\ \theta_y \\ \theta_z \end{bmatrix} = \begin{bmatrix} 0 \\ 0 \\ 0 \\ 0 \\ 0 \\ 0 \end{bmatrix} \tag{3.5}$$

where: K_{ij} are submatrices of the overall element stiffness matrix; u, v, and w represent vectors of displacements at each node; and θ_x, θ_y, and θ_z represent vectors of rotation at each node. Here, the drilling degrees of freedom θ_z have been added, although they do not appear in the equilibrium expressions. This was done to enable easier directional transformation by the method described in the following paragraph.

To use this plate element for a three-dimensional structure, it was necessary to transform between the local and global degrees of freedom. To accomplish this, the transformation method presented by Zienkiewicz[92] was used. In this method, a transformation matrix **L** is formed by:

$$\mathbf{L} = \begin{bmatrix} \lambda & \mathbf{0} \\ \mathbf{0} & \lambda \end{bmatrix} \tag{3.6}$$

where λ is a 3×3 matrix of direction cosines of the angles formed between the global and element axes. The local plate element stiffness matrix, $\mathbf{K}'$ (after rearranging so that the degrees of freedom at a particular node are grouped together), can then be transformed into global coordinates by the expression:

$$\mathbf{K} = \mathbf{T}^{\mathrm{T}}\mathbf{K}'\mathbf{T} \tag{3.7}$$

where: **K** is the element stiffness matrix in global coordinates, and **T** is a transformation matrix given by:

$$\mathbf{T} = \begin{bmatrix} \mathbf{L} & 0 & 0 \\ 0 & \mathbf{L} & 0 \\ 0 & 0 & \mathbf{L} \end{bmatrix} \tag{3.8}$$

and built up of a number of **L** matrices equal to the number of nodes in the element.

The local model is a representation of a building block of the overall fuselage structure. For example, it may be a model of the unit cell (i.e.repeating unit) of the general grid configuration as illustrated in Fig. 3.2. Once the selection of a shear deformable plate ele-

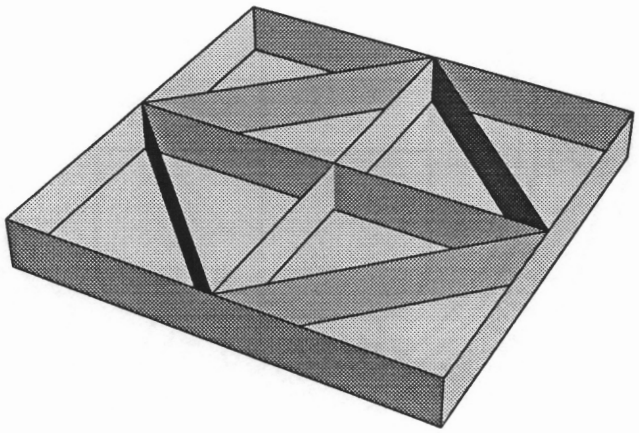

Figure 3.2 General grid unit cell

ment was made, the next step was to use that element to model the grid unit cell. A six-node triangular element was chosen since the triangular shape allows for easy mesh generation with varying spiral grid angles, and the quadratic interpolation functions provide a good degree of accuracy. A series of analyses were performed on a standard unit cell with increasing mesh sizes. As a test of the convergence of the solutions, the models were fixed

at the center point and a bending moment was applied to each side. In Fig. 3.3, the resulting average curvatures for each case are shown with the corresponding mesh. As can be seen in this figure, a large number of degrees of freedom is not necessary to provide a reasonably accurate solution.

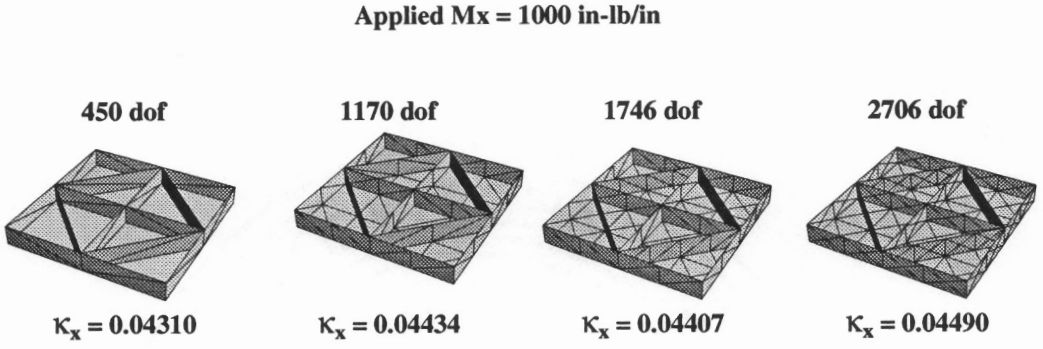

Figure 3.3 Grid unit cell mesh convergence

3.3 Global Model

The purpose of the global model was to provide an accurate analysis of the overall structure while reducing the numerical requirements relative to the local model. The global model must also relate to the local model, in that it must be equivalent to the local model in stiffness and be capable of providing information needed to determine, in conjunction with the local model, the stresses in various subregions. The global model is not limited to any particular type of element, but based on the assumptions for the fuselage crashworthiness problem that are explained in Sec. 4.1 , a planar beam-frame-type global model was chosen. This does not imply that the structure necessarily resembles a beam, it merely specifies which degrees of freedom are maintained in the simple model. A standard beam-type finite element has a total of six degrees of freedom, three at each node: horizontal translation, vertical translation, and rotation. The beam-type element is shown sche-

matically in Fig. 3.4. The challenge, then, is to relate the complex unit cell structure to this simple beam element, or determining the effective beam-like properties of this unit cell.

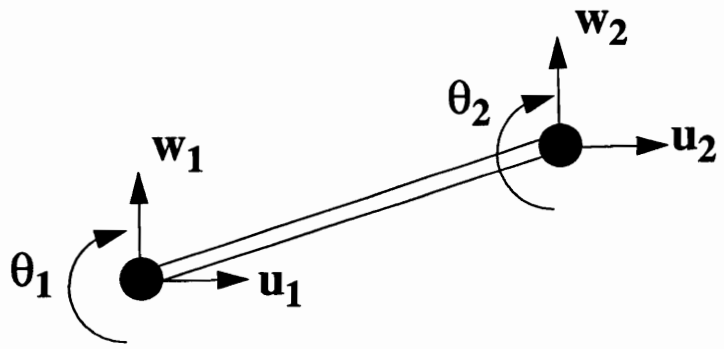

Figure 3.4 Schematic of beam-type element

The idea of replacing a lattice-like structure with a simple continuum analogy is not new. Analytical examples of this have been presented by Heki and Saka[94], Saka and Heki[95], Ozaki[96], Noor *et al*[97], and Noor and Nemeth[98,99]. An excellent discussion of the use of the global-local method in finite elements to model periodic structures has been recently presented by Voleti[100]. Using analogous beam elements allowed for the important structural response and failure characteristics to be incorporated, while maintaining the computational efficiency required for the multiple analysis runs needed during the optimization process.

Having reduced the more complex problem to a simple beam analogy, a model of any repeating unit structure (e.g. an aircraft fuselage) can be constructed using the conventional approach for beam finite elements. The application of this to a fuselage cross-section is discussed and shown in Sec. 4.2.

3.4 Reduction of Local Model to Global Model

The heart of the global-local approach is the method for connecting the plate-type local model to the conventional beam-type global model. This approach must provide both a means for reducing the order of the local problem to the global degrees of freedom as well as a means for recovering local stress details upon executing the global model. This was a significant task, and the applications of this type of approach are far-reaching. In this section, the methods chosen for accomplishing these two objectives are presented, discussed and validated.

3.4.1 Development of Reduced Beam-Like Stiffness Matrix

As mentioned above, a reduction method must be used to merge the complex local (plate) model with the global (beam) model. For a typical element in the global model (which represents a unit cell of the grid-stiffener configuration), we have the static response equations:

$$[K]\ \{U\} = \{F\} \tag{3.9}$$

where: $[K]$ is the 6x6 beam stiffness matrix, $\{U\}$ is the vector of 6 degrees of freedom (two translations and one rotation at each node), and $\{F\}$ is the vector of forces (two forces and one moment at each node). However, each global beam element will represent a local element with a large number of degrees of freedom, which will be represented by the larger set of equations:

$$[k]\ \{u\} = \{f\} \tag{3.10}$$

where:$[k]$ is the $N \times N$ local unit cell stiffness matrix, $\{u\}$ is the vector of N degrees of freedom, and $\{f\}$ is the vector of N forces. Thus, we require a transformation operator L, such

that:

$$[K] = L([k]) \tag{3.11}$$

The method chosen for achieving this involves static condensation and a degree of freedom reduction through transformation. This method follows these steps:

1. Selection of Appropriate Degrees of Freedom - A typical node of the two-node one-dimensional beam element has three degrees of freedom (two translations and one rotation). Each of these nodes represents the plate element nodes along one entire side of the grid unit cell model. However, each of these nodes has six degrees of freedom (three translations and three rotations). This is illustrated in Fig. 3.5. It was decided to have each beam degree of freedom represent an average of the corresponding degree of freedom along the appropriate edge. Thus, the horizontal displacement, vertical displacement and "y"-rotation degrees of freedom in the skin along the two opposing edges of the local model must be retained (see Fig. 3.5). Additionally, the horizontal displacements along the top of the ribs along those edges are also kept (see #3 below).

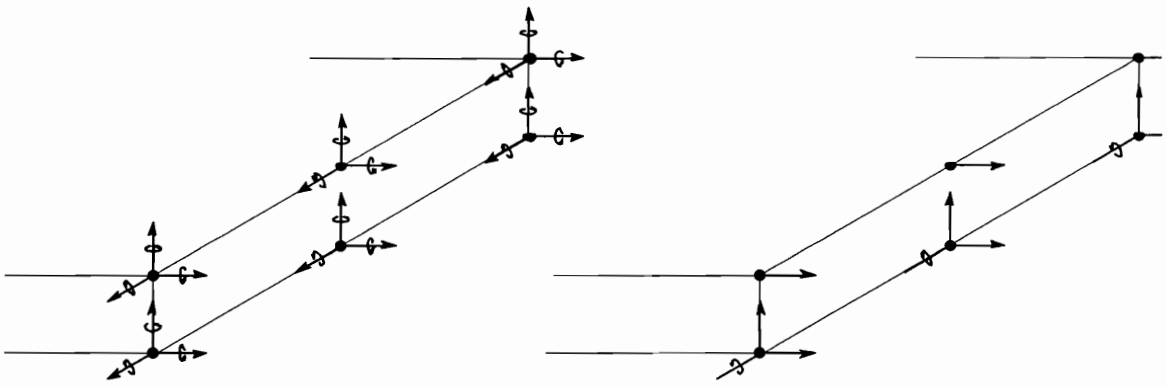

(a) Initial full set of d.o.f along edge *(b) Retained d.o.f. during initial condensation*

Figure 3.5 Reduction of degrees of freedom along edge of local model during initial condensation

2. Static Condensation of Unneeded Degrees of Freedom - Once the required degrees of freedom are selected, static condensation is used to eliminate the remaining degrees of freedom. This reduces the order of the stiffness matrix considerably (from 1170×1170 to 72×72 in our example). If we partition the solution vector into the required degrees of freedom and those to be condensed out, we obtain the system of equations:

$$\begin{bmatrix} K_{rr} & K_{rc} \\ K_{cr} & K_{cc} \end{bmatrix} \begin{bmatrix} U_r \\ U_c \end{bmatrix} = \begin{bmatrix} F_r \\ F_c \end{bmatrix} \tag{3.12}$$

where the subscript r denotes required degrees of freedom and the subscript c denotes degrees of freedom to be condensed. Solving the second system of equations for U_c yields:

$$U_c = K_{cc}^{-1} [F_c - K_{cr} U_r] \tag{3.13}$$

Substituting this expression into the first system of equations in Eqn. 4.1 yields the reduced system containing only the required degrees of freedom:

$$[K_{rr} - K_{rc} K_{cc}^{-1} K_{cr}] \{U_r\} = [F_r - K_{rc} K_{cc}^{-1} F_c] \tag{3.14}$$

This reduced system is exact, in that no effects from the original system have been eliminated.

3. Constraint of Edge Rotations for Ribs - For a single unit cell, the rib which runs along the edge corresponding to the beam edge represents only half of the actual rib (the other half of the rib would be on the adjacent unit cell). For this reason, simply joining the skin rotational degree of freedom at that edge is not sufficient. For each of the nodes along this edge, a multi-point constraint is added which enforces the following equation:

$$\theta_{skin} = \frac{u_{rib} - u_{skin}}{h} \tag{3.15}$$

where: θ_{skin} is the rotational degree of freedom in the skin node, u_{rib} is the horizontal translation at the node at the top of the rib, u_{skin} is the horizontal translation at the skin node, and h is the height of the rib. This is a straightforward geometrical relationship, but correctly joins the rib sections of adjoining reduced beam elements. During the implementation of these constraints, the horizontal displacement degrees of freedom in the rib are eliminated from the system of equations. Thus, the only remaining degrees of freedom are the horizontal and vertical displacements and rotations along the skin nodes on the two opposing edges. This process is illustrated in Fig. 3.6.

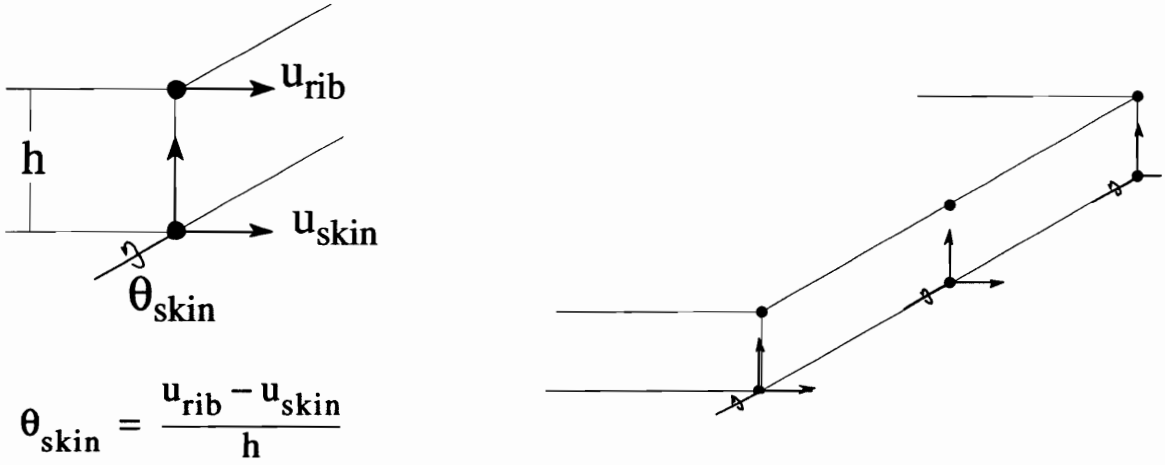

(a) Illustration of constraint on rib rotation *(b) Remaining d.o.f. after imposition of constraints*

Figure 3.6 Schematic of imposition of multi-point constraint

4. Final Reduction to Beam-Type System - Following the three steps mentioned above, we now have a condensed system of equations for the required degrees of freedom along the two edges of the unit cell:

$$[K]\ \{U\}\ =\ \{F\} \tag{3.16}$$

The desired system of equations for a one-dimensional beam-type element are of the

form:

$$[k]\ \{u\} = \{f\} \tag{3.17}$$

where $\{u\} = \lfloor u_1\ w_1\ \theta_1\ u_2\ w_2\ \theta_2 \rfloor^T$, $\{f\} = \lfloor N_{x1}\ Q_1\ M_1\ N_{x2}\ Q_2\ M_2 \rfloor^T$, and [k] is a 6×6 beam stiffness matrix. As stated above, it was decided to represent the beam degrees of freedom as averages of the corresponding unit cell edge degrees of freedom. Thus, if we define a transformation matrix [H] in the following manner

$$\{U\} = [H]\ [u] \tag{3.18}$$

where the matrix [H] is a rectangular transformation matrix containing a number of ones which define which edge degrees of freedom are averaged to obtain each beam degree of freedom (see Fig. 3.7). The corresponding transformation equation for the forces is:

$$\{F\} = \frac{1}{J}[H]\ \{f\} \tag{3.19}$$

where J is the number of nodes along the edge to be averaged. This term is present because the terms in the beam force vector represent a sum, not an average, of the forces along the edges.

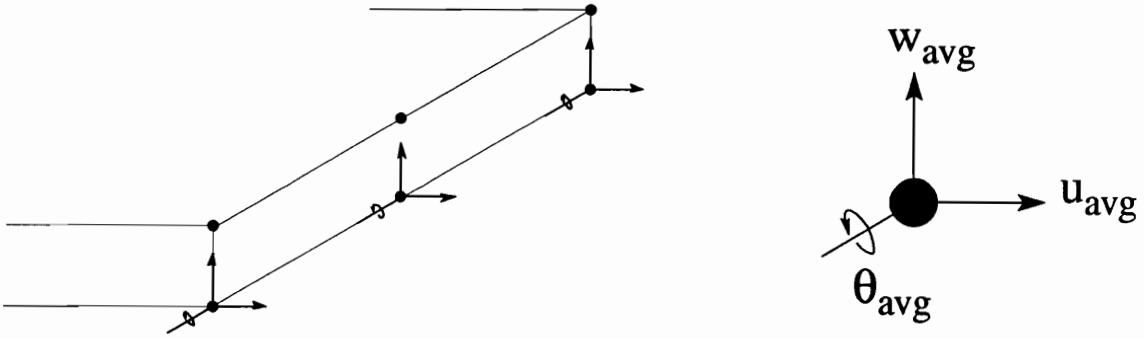

(a) Final retained local model d.o.f. *(b) Global model beam-type d.o.f.*

Figure 3.7 Final reduction of local model to global model degrees of freedom

After some manipulation, the equation expressing the beam-type stiffness matrix in terms of the condensed unit cell stiffness matrix is determined to be:

$$[k] = [H]^T [K] [H] \tag{3.20}$$

Following the four steps outlined above, it is possible to reduce a very large stiffness matrix for the unit cell finite element model constructed from shear deformable composite plate elements to a simple one-dimensional beam-type stiffness matrix. Thus, when exercising the global model for a fuselage cross-section, this reduced stiffness matrix is used as the element stiffness matrix rather than generating a stiffness matrix by conventional methods. Other than this substitution, the beam-type finite element analysis is conducted exactly like a conventional analysis.

3.4.2 Recovery of Local Stresses Using Global Model Results

In the preceding section, a method was presented for determining the effective stiffnesses of the local unit cell to be used in the beam-type global model. This global model could then be analyzed to determine the response of the overall structure. However, in order to accurately predict local failure modes, a method for recovering local stresses from these global results was required.

The main aspect of the global-local reduction process, as explained in the preceding section, is the static condensation algorithm. Recall that the degrees of freedom in the local model were re-ordered so those which were to be retained (the beam-type degrees of freedom) were at the top of the displacement vector (see Eqn. 3.12). For static condensation procedures, recovery of the condensed degrees of freedom is a well-known process (see Cook *et al*[101]). Static condensation is accomplished by performing a Gaussian

elimination on the stiffness matrix. This produces the reduced stiffness matrix in the first N rows and columns, where N is the number of retained degrees of freedom. Neglecting these first N rows, the remainder of the operated matrix is of the form:

$$\begin{array}{l} \\ \text{Row corresponding to:} \end{array} \begin{array}{c} \text{Column corresponding to:} \\ \begin{array}{cccccccc} & u_1 & u_2 & u_3 & u_4 & u_5 & u_6 & \\ u_4 & C_{41} & C_{42} & C_{43} & 0 & 0 & 0 & \dots \\ u_5 & C_{51} & C_{52} & C_{53} & C_{54} & 0 & 0 & \dots \\ u_6 & C_{61} & C_{62} & C_{63} & C_{64} & C_{65} & 0 & \dots \\ & \dots & \dots & \dots & \dots & \dots & \dots & \dots \end{array} \end{array} \tag{3.21}$$

Recovery of the condensed degrees of freedom is then obtained by performing back substitution. That is, the first condensed degree of freedom is obtained simply by multiplying the stiffness terms in its corresponding row by the known (retained) displacements. For example, in the above illustration u_1 through u_3 are the retained displacements. The condensed displacement, u_4, is obtained using the relationship:

$$u_4 = C_{41}u_1 + C_{42}u_2 + C_{43}u_3 \tag{3.22}$$

Now that u_4 is know, u_5 may be obtained using:

$$u_5 = C_{51}u_1 + C_{52}u_2 + C_{53}u_3 + C_{54}u_4 \tag{3.23}$$

and so on until all displacements have been obtained. These displacements can then be used by conventional means to obtain derivatives and stresses, if desired.

Performing this back substitution, however, can generally be computationally time-consuming. It would also require storing the Gauss-eliminated stiffness matrix. With a little forethought, though, this process can be greatly simplified. The process utilized in this

study can be described by the following steps:

1. *Partitioning of System of Equations.* Prior to the static condensation procedure, the set of equations is re-ordered in a manner similar to equation 3.12, with the addition that any degrees of freedom required for calculation of local stresses are placed immediately following the retained degrees of freedom, but just prior to the other degrees of freedom to be condensed. This results in a system of equations like:

$$\begin{bmatrix} K_{rr} & K_{rs} & K_{rc} \\ K_{sr} & K_{ss} & K_{sc} \\ K_{cr} & K_{cs} & K_{cc} \end{bmatrix} \begin{bmatrix} U_r \\ U_s \\ U_c \end{bmatrix} = \begin{bmatrix} F_r \\ F_s \\ F_c \end{bmatrix} \tag{3.24}$$

where as before, the subscript r denotes required, or retained, degrees of freedom, subscript c denotes degrees of freedom to be condensed, and subscript s denotes degrees of freedom required to compute local stresses. (Note that for each element in which stresses are required, there are 36 degrees of freedom necessary: six at each of the six nodes.)

2. *Static Condensation of Stiffness Matrix.* The static condensation procedure discussed in the preceding section is then applied to the stiffness matrix. This results in the triangularized form as shown in Eqn. 3.21.

3. *Combination of Averaged Degrees of Freedom.* The columns in the Gaussian-eliminated stiffness matrix corresponding to displacements which are being averaged via the method described in the preceding section are combined, since these displacements are prescribed to be equal.

4. *Recovery of Degrees of Freedom Needed for Local Stress Calculation.* The back substitution process is performed on the revised stiffness matrix as described above. How-

ever, in this case the global model displacements are not know a priori. So rather than compute a scalar value for each displacement, a row vector of coefficients of the retained degrees of freedom is constructed. For example, if the revised stiffness matrix in its lower triangularized form is given by Eqn. 3.21, then the expression for required degree of freedom u_4 is given by:

$$u_4 = \begin{bmatrix} C_{41} & C_{42} & C_{43} \end{bmatrix} \begin{bmatrix} u_1 \\ u_2 \\ u_3 \end{bmatrix} \tag{3.25}$$

and, thus the expression for u_5 would be:

$$u_5 = \left[C_{51} + C_{54}C_{41} \middle| C_{52} + C_{54}C_{42} \middle| C_{53} + C_{54}C_{43} \right] \begin{bmatrix} u_1 \\ u_2 \\ u_3 \end{bmatrix} \tag{3.26}$$

Therefore, to calculate a stress (or stresses) in a given element, this process is repeated for each of the 36 degrees of freedom in that plate element. This leads to a set of 36 equations relating these degrees of freedom to the 6 retained beam-type degrees of freedom from the global model. These equations may be expressed as:

$$\{u_e\} = [S] \{u_r\} \tag{3.27}$$

where: u_e are the 36 degrees of freedom in the plate element for which stresses are required, u_r are the 6 beam-type degrees of freedom, and [S] is made up of the 36 row vectors derived as above.

5. *Derivation of Constitutive Matrix for Computation of Local Stresses.* The [S] matrix obtained in Step 4 is the essential part of the stress recovery process. Once this matrix is

obtained, the stress computation is achieved in a manner identical to that used in the standard plate finite element procedure, with the exception that the displacements, $\{u_r\}$, are treated as unknown variables rather than as known numerical quantities. The first step is to transform the $\{u_e\}$ vector to the plate element local coordinate system. This is accomplished by the transformation method described in Sec. 3.2 using:

$$\{\hat{u}_e\} = [T]\{u_e\} \tag{3.28}$$

where: $\{\hat{u}_e\}$ are the 36 transformed displacements and $[T]$ is the 36×36 transformation matrix which depends on the orientation of the plate element in the local model.

The local midplane strains and curvatures in the plate element are computed from these transformed displacements by the expression:

$$\{\varepsilon\} = [D]\{\hat{u}_e\} \tag{3.29}$$

where: $\{\varepsilon\}$ are the 6 midplane strains and curvatures for a plate (i.e. ε_x^0, ε_y^0, γ_{xy}^0, κ_x, κ_y, and κ_{xy}) and $[D]$ is a 6×36 operator matrix whose terms are derivatives of the finite element shape functions.

The local stresses are then computed from the strains and curvatures by use of the standard composite constitutive relationships:

$$\{N\} = [ABD]\{\varepsilon\} \tag{3.30}$$

where: $\{N\}$ are the local stress resultants and bending moments (i.e. N_x, N_y, N_{xy}, M_x, M_y, and M_{xy}) and $[ABD]$ is the classical 6×6 constitutive matrix for a layered plate.

If Eqns. 3.27 through 3.30 are combined, the stresses in the local element can be com-

puted by:

$$\{N\} = [A]\ \{u_r\} \tag{3.31}$$

where: $[A]$ is a 6×6 matrix which is given by:

$$[A] = [ABD]\ [D]\ [T]\ [S] \tag{3.32}$$

For any given desired local stress, it is only necessary to utilize the corresponding row of the $[A]$ matrix. The significance of this result is that, using only a small portion of the back substitution process just once and storing 6 numbers, any local stress may then be computed easily for any set of global solutions. The importance of this fact on minimizing the required computational effort cannot be overstated. The ramifications of the process could reach far beyond the application being exercised in the current study.

3.5 Validation of Global-Local Approach

To validate the approach described in this chapter, a simple example was chosen. The standard grid unit cell shown in Fig. 3.8 was selected for the analysis. Three of these unit cells were placed in sequence and assumed to be cantilevered at the left edge as shown in Fig. 3.9.a. Three different types of loads were applied at the free edge of the cantilever: a transverse force Q, a moment M, and an axial load, P. (These represent the three types of loads possible in a beam-type analysis).

As a point of comparison, the detailed mesh used in the local model was duplicated three times and analyzed using the three different loading conditions described above. The mesh for this model is shown in Fig. 3.9.a. The global-local reduction method was then applied to a single unit cell to derive a beam-type stiffness matrix, which was used for a

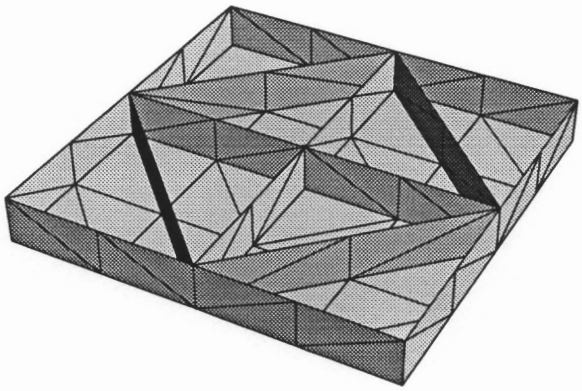

Figure 3.8 Finite element mesh of general grid unit cell

simple 3-element global analysis. The mesh for this model is shown in Fig. 3.9.b. In Figs.

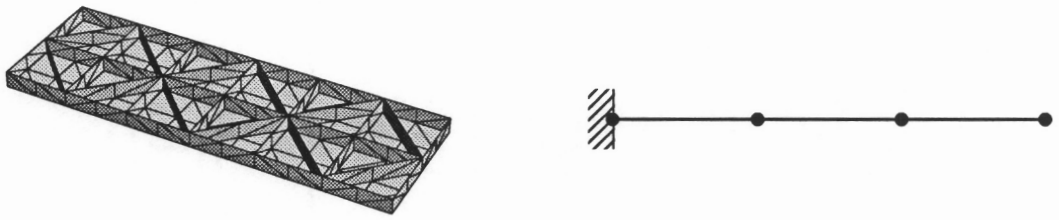

(a) Full analysis *(b) Reduced analysis*

Figure 3.9 Finite element meshes for analysis of 3-unit cell cantilever problem

3.10 through 3.12, the displacement predicted by the two models are compared for each of the three loading cases. As shown in these figures, the global-local approach performs exceptionally well in representing with an extremely simple model the behavior of a very complex system. Excellent agreement was also found with the local stress resultants. Further validation of both deflection and stress accuracy will be given in Sec. 4.3 specifically for the fuselage cross-section model.

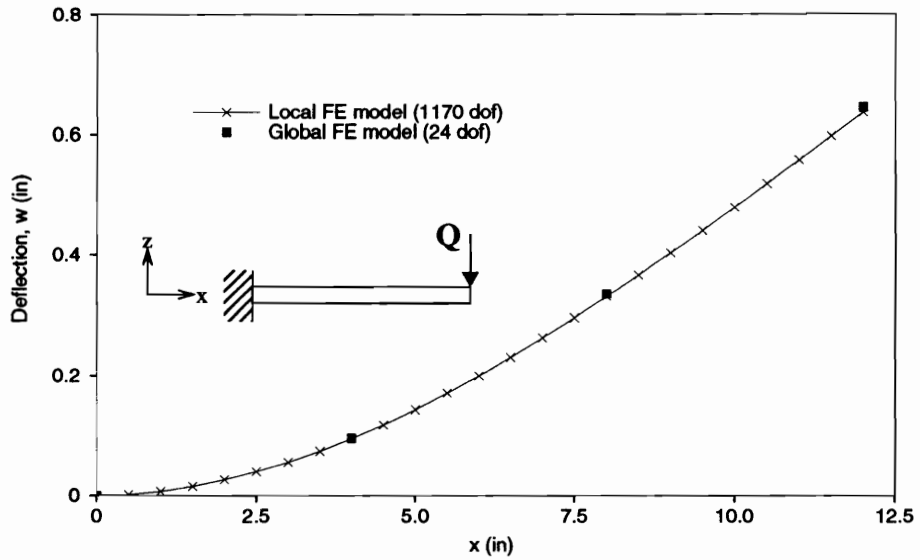

Figure 3.10 Comparison of local and global models for 3-unit cell cantilever with end load

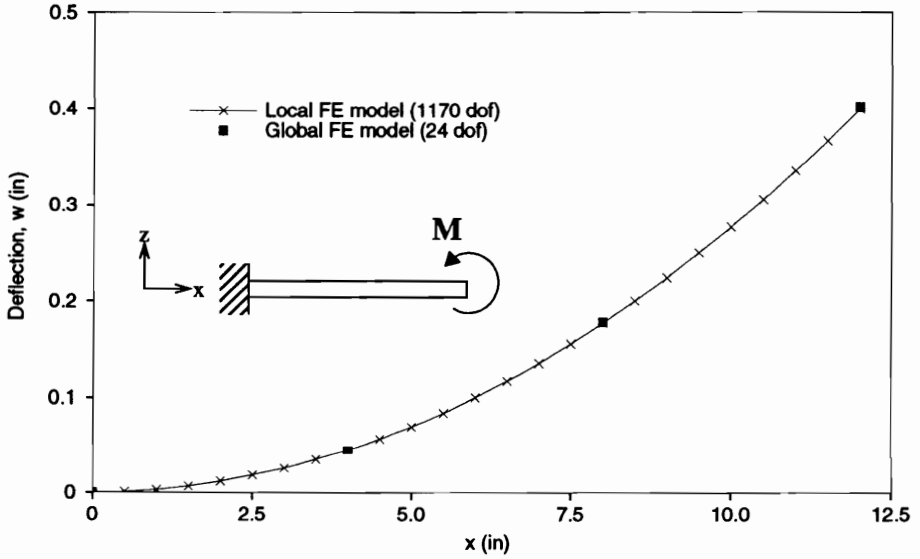

Figure 3.11 Comparison of local and global models for 3-unit cell cantilever with end moment

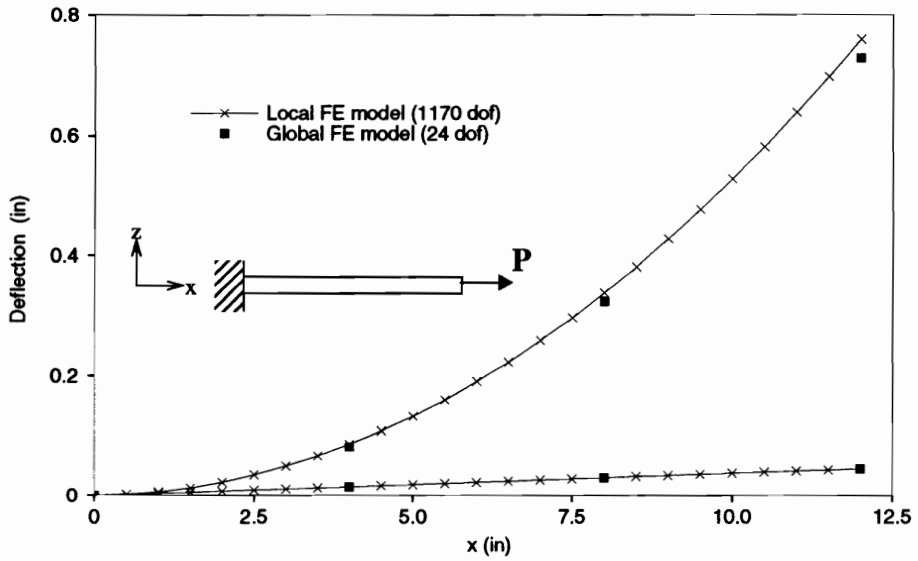

Figure 3.12 Comparison of local and global models for 3-unit cell cantilever with axial end load

4.0 Application of Global-Local Approach to Fuselage Crashworthiness

In Chapter 3, a method was developed, described and validated for reducing the cumbersome analysis of a grid-stiffened shell structure to a simpler beam-type model. This reduction of order was necessary to enable the estimation of energy absorption during an impact event, in which local elements of the structure may fail at various times. While tools exist for analyzing the full structure in this manner (primarily finite element analysis), they are computationally demanding and not suitable for use in preliminary design, when many different designs must be considered and analyzed. Thus, the current global-local procedure was developed to meet this need for efficient analysis. In Chapter 3, this method was described in a general manner. In this following sections, the procedure by which this method was implemented for the specific problem of grid-stiffened fuselage crashworthiness will be described and validated.

4.1 Key Assumptions

The global model of the fuselage frame must accurately represent the structural response and allow for accurate calculation of the local failure modes upon recovery. However, it must be kept in mind that the global model forms the analytical backbone of the preliminary design optimization algorithm. Thus, computational efficiency is of primary importance in selecting an analysis method. Pursuant to this requirement and the discussion of fuselage structures in Sec. 1.1, The following assumptions were made (for preliminary design purposes);

1. Only the fuselage subfloor need be modeled. Boitnott[102] has shown in frame tests

that the structure above the fuselage floor does not contribute significantly to the energy absorption capability of the fuselage.

2. Modeling a cross-section of the fuselage is sufficient. Woodson[1] analyzed just one cross-sectional frame of a fuselage. Since he considered a conventional reinforcement configuration, he was able to utilize the fact that there is little interaction between the neighboring frames. However, in a grid-stiffened structure, this is no longer obvious. However, a typical fuselage structure is fairly long in the axial direction. Therefore, one would not expect to see a large variation in response in that direction. Thus, if we consider a cross-section remote from either the fuselage nose, tail or bulkheads, the effect of axial variations in response is probably of little consequence in terms of energy absorption characteristics of the fuselage sub-floor.

3. Dynamic effects can be neglected. Farley[103] conducted both static and dynamic crushing experiments on composite (epoxy matrix with graphite, Kevlar, and glass fibers) and aluminum tubes. Total energy absorption was essentially the same for the static and dynamic tests, as were the failure modes and post-crushing integrity.

It should be noted here for completeness sake that in the initial stages of this study, it was assumed that geometric nonlinearity could be neglected. The results of Woodson[1] suggest that fuselage frames built up from composite materials are subject to brittle failure modes. Thus, it is expected that these modes would occur with significant enough load reductions that the bulk of energy absorption would occur prior to any substantial large deformations of the frame structure. However, for grid-stiffened fuselage structures, this was often found not to be the case. Thus, this assumption had to be discarded, and an approximate method for incorporating nonlinear effects was implemented. This method is

described in detail in Sec. 4.6.

4.2 Description of Fuselage Sub-floor Model

Based on the assumptions listed above, the global model was chosen to be a linear static finite element model of a cross-section of the fuselage sub-floor built up of one-dimensional beam frame elements. The global model is illustrated schematically in Fig. 4.1. The impact force between the aircraft and the ground is idealized by a concentrated radial load at the bottom of the fuselage. This load is assumed to act directly toward the fuselage center, thus symmetry allows consideration of only one half of the subfloor cross-section. The upper end of the beam was considered to be fixed, representing the connection to the relatively rigid passenger deck floor structure. The vertical deflection of the point at which the load is applied was considered to be the measured displacement and was used along with the predicted load to estimate the energy absorption during the impact sequence. This will be discussed in more detail in Sec. 4.4.

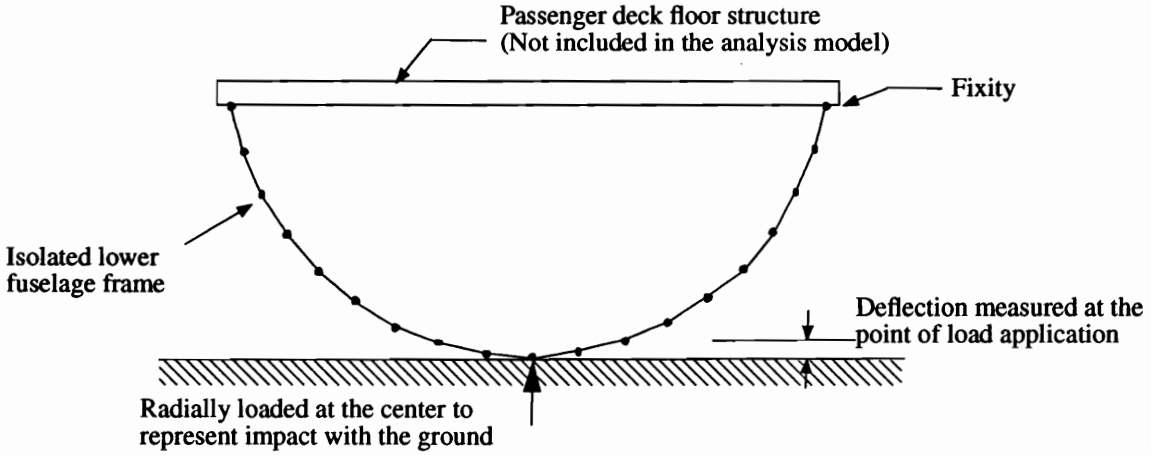

Figure 4.1 Example of proposed global model configuration (follows Woodson[1])

The global-local procedure developed in this study and described in Chapter 3 reduces

the complex problem of a grid unit cell to a simple beam-type stiffness matrix. Thus, each unit cell of the fuselage structure was represented by one beam element in the global model. The number of elements in the global model thus depends on the grid spacing, which was chosen to be one of the design variables in the optimization phase. Manufacturing limits and weight constraints place an upper bound on the number of grid unit cells that may be placed along the circumference of the fuselage. This will be discussed in Chapter 5. However, it should be noted that if grid spacing is chosen to be too large, there will only be a small number of beam-type elements in the global model which may result in some inaccuracy in the predicted behavior. This places an effective lower bound on the number of unit cells that may be contained in the quarter-fuselage.

The local model for the grid unit cell could be as complex as the general grid (see Fig. 1.3.d). However, for the purposes of demonstration in this study, the analysis and design were limited to just the isogrid-type unit cell (see Fig. 1.4.a). This does not necessarily limit the designs to actual isogrid structures. True isogrids are comprised of equilateral triangles, while in the present study the angle formed by the ribs was allowed to change.

The local model was analyzed using the plate assemblage method described in Chapter 3. The dimensions of the unit cell were permitted to vary, as they are affected by the design variables (e.g. rib angle and grid spacing). In addition, assumptions were made regarding the nature of the skin and rib materials. These assumptions were:

1. *Skin material is isotropic.* Conventional fuselage skins are typically constructed of an isotropic metal, usually aluminum or titanium. As aircraft designers give further consideration to the use of advanced composite materials in the construction of fuselages, it is conceivable that skins could be fabricated which are not isotropic. However, most conceptual designs for composite fuselages cur-

rently utilize quasi-isotropic layups or a layup very nearly isotropic. Since the purpose of the present study was to develop and demonstrate the preliminary design tool, it was felt that adding such a complication to the design was better left to subsequent investigators.

2. *Rib material is isotropic or orthotropic.* A metal grid-stiffened fuselage would consist of isotropic ribs, but the use of composites to construct the fuselage most certainly would result in ribs that are no longer isotropic. The manufacturing methods developed to fabricate these composite ribs, though, in most cases limit the fiber orientation to coincide with the axial direction of the ribs. Thus, the ribs would almost certainly be unidirectional and at most orthotropic. This is not a significant limitation, though, as the ribs' task of adding stiffness and strength to the fuselage skin are best suited by aligning the fibers in that direction.

4.3 Validation of Global-Local Approach for Fuselage Sub-floor Analysis

In Sec. 3.5, several example cases were shown which validated the global-local method developed in this project. Although these examples displayed excellent correlation between the global-local approach and a full detailed model, an additional validation was performed to further increase confidence in the global-local approach. Specifically, it was desired to validate the approach for the fuselage sub-floor geometry. Also, since accurate prediction of local stresses is crucial to correctly predict the response during impact, it was desired to validate the stress recovery method for the fuselage-type problem.

The geometry selected for the validation problem was identical to that described above, with the following parameters:

- Isogrid unit cell (equilateral triangles)
- Fuselage radius = 129.36 inches

- 16 unit cells along quarter-circumference
- All-aluminum construction
- Skin thickness = 0.04 inches
- Rib thickness = 0.36 inches
- Rib height = 0.875 inches

The global-local approach was used to predict the deflection and stresses due to a radial load of 50 pounds. As a check to these results, a finite element model was constructed using a commmercial code, MSC/NASTRAN for Windows. The full quarter-circumference was modeled with a total of 3419 nodes and 5008 NASTRAN plate elements, resulting in a total of 20,514 degrees of freedom. A portion of the mesh used is shown in Fig. 4.2. The predicted deflections for the global-local and NASTRAN models are shown

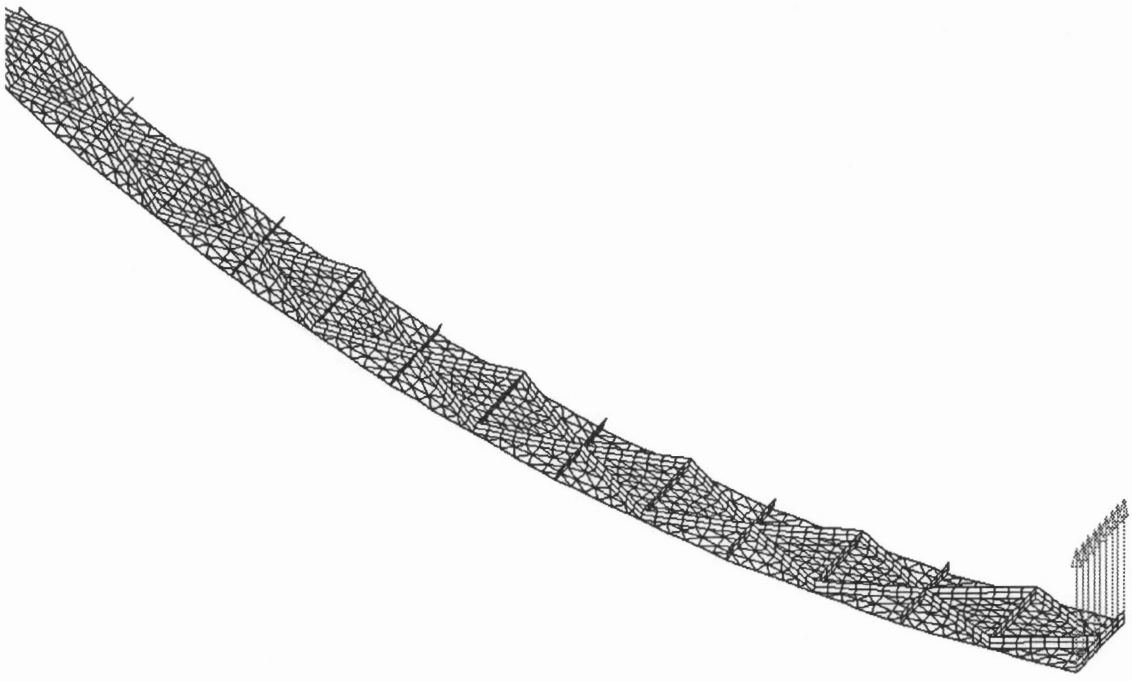

Figure 4.2 Portion of NASTRAN mesh for fuselage sub-floor validation problem

in Table 4.1 for two different mesh densities of the local model in the global-local approach. As is evident from these results, both global-local meshes correlated very well with the NASTRAN model.

Table 4.1 Comparison of deflections for global-local and NASTRAN models

Model	Vertical deflection at bottom (in)
Global-Local coarse mesh (378 dof per unit cell)	4.416
Global-Local refined mesh (954 dof per unit cell)	4.629
NASTRAN (20,514 dof total)	4.565

In Fig. 4.3, the rib forces along the circumference of the models are plotted for the global-local and NASTRAN models. Again, there is excellent correlation between the models. This was an encouraging result, as it provided justification to use the more coarse local mesh in the global-local model, thus reducing computational requirements significantly.

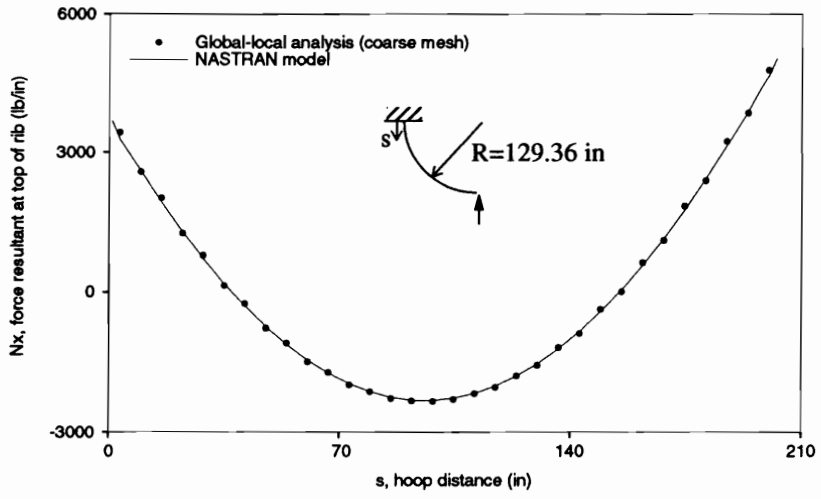

Figure 4.3 Comparison of global-local and NASTRAN results for rib forces

4.4 Progressive Failure Approach and Crashworthiness Estimation

During an impact event, much of the energy of vertical motion is absorbed by deformation and failure of the fuselage structure. It is desirable to maximize this energy absorption capability, as it leaves a smaller amount of energy to be transferred to the passengers and their seat structure. In order to accurately estimate the capability of the fuselage to absorb energy, it is necessary to be able to predict when and where the structure fails, and to incorporate these failures into the subsequent behavior of the structure.

Grid-stiffened composite structures, due to the presence of multiple redundant load paths, can typically sustain several failure events before a significant loss of load-carrying capability occurs. Reddy *et al*[104] demonstrated this phenomenon for isogrid wide columns by successively cutting different stiffener segments and determining the subsequent effects on buckling loads. Thus, an analysis which seeks to determine the energy absorption capability of this type of structure must be capable of predicting damage events, determining the effect of this damage on the response, then modeling the damaged structure. In Sec. 3.4.2, the method for incorporating these capabilities in the detailed local model was discussed. In this section, the method for employing these features in the global fuselage model will be presented.

After an extensive review of progressive failure literature, Woodson[1] concluded that no suitable progressive failure model for a composite beam-type frame existed. Existing progressive failure models for metallic structures could not be applied, as they are unable to handle the discrete load drops typical of composite structures. Also, existing progressive failure models for composites only apply on a simple laminate level. Woodson remedied this by utilizing a step-wise approach in combination with his finite element model of

the fuselage frame. After the model predicted one or more failure events, discrete stiffness changes were made to the damaged elements. Another analysis was then performed on the revised structure. This analysis was assumed to take over at the displacement at which the failure occurred, with the revised stiffness providing the estimated discrete load drop at that failure event. A fuselage crash sequence can be represented well by a displacement-controlled event. For this reason, these discrete load drops are assumed to occur at a constant displacement. This process is illustrated schematically in Fig. 4.4.

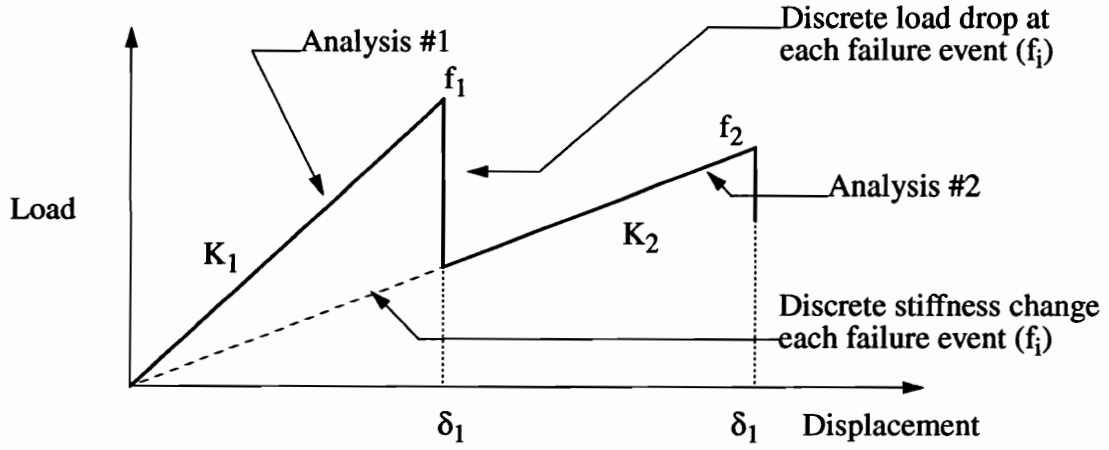

Figure 4.4 Schematic of progressive failure sequence [1]

The progressive failure model used by Woodson was selected to be applied to the grid-stiffened composite structures considered in this effort. Since the stiffeners and skin will be constructed from filamentary composites, their failure mechanisms should be brittle and be represented by discrete load drops. The local failure modes, which are described in Sec. 4.5 below, all fit within the limits of the step-wise stiffness modification approach. The rib crippling, skin buckling, and rib or skin failures are all incorporated by discrete reductions in the stiffnesses of the affected segments. The general procedure for the progressive failure analysis consists of the following steps:

1. Apply initial load to the structure.
2. Predict regions of local failure.
3. Incorporate effect of failed region(s) on subsequent structural response.
4. Re-analyze the structure with effect of previous damage.
5. Repeat until end criterion is achieved.

In the remainder of this section, these steps will be discussed in more detail. Following that, the measure of crashworthiness used in this study will be explained.

The first step in the above procedure is to apply the initial load to the fuselage structure. This is done using the global fuselage sub-floor model described in Sec. 4.2. A unit radial load is applied to the model, and the deformation and local stresses are determined using the global-local approach. Using the local stresses in each unit cell region within each element, local failure models are utilized to predict which region(s) will be the first to fail. For the isogrid-type grid arrangement used in this study, the unit cell is divided into nine regions; five rib regions and four skin regions. These are identified schematically in Fig. 4.5. The models used to predict the local failure modes and events will be discussed in the following section.

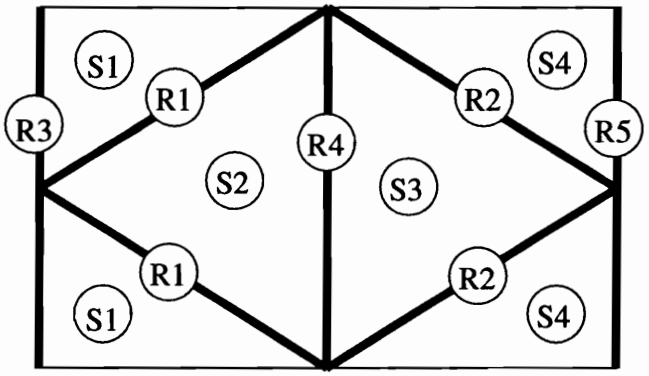

Figure 4.5 Location of rib and skin regions on isogrid-type unit cell

Once the local failure events have been predicted, the effects of this damage must be incorporated into the subsequent behavior of the structural model. The approach chosen for the current study was to degrade the stiffnesses of the plate elements in the local model for the regions which were predicted to have failed prior to a step. This is a common approach in composite failure models, but there is no general agreement on the amount of degradation that should be utilized. Since the purpose of this project was to develop a tool for preliminary design, there was no necessity for predicting the exact value of the remaining load-carrying capability of a failed region. Further, it would be conservative to assume that a failed region is not capable of carrying additional load. For these reasons, it was decided to fully degrade the stiffnesses of the failed regions. For numerical reasons, it was not feasible to set the stiffnesses to exactly zero, so they are reduced by 99.9% of their original values.

Once the properties of the failed regions have been modified to account for existing damage, the global-local procedure is used once again to predict the global response of the fuselage sub-floor. Since the stiffness of one or more regions has been reduced, the stiffness of the overall structure will also be reduced. A unit radial load is applied, and again the local stress components are determined using the global-local recovery procedure. The local failure criteria are again used to predict the next local failure occurrence(s). Occasionally, the next failure event is predicted to occur at a displacement that is less than the displacement at the previous failure event. Since the impact scenario is assumed to be a displacement-controlled load situation, these failure events are neglected and are assumed to have occurred in concert with the other failing regions during the previous failure event.

The above procedure can theoretically continue until all regions in the model have

failed. However, there are two factors which allow the analysis to be stopped before this occurs. These factors are:

Substantial load reduction. After a sufficient number of critical regions have failed, the stiffness of the overall model can become so small that the load is negligible relative to the prior load history. At this point, the structure is no longer capable of absorbing an appreciable amount of energy. Thus, it is no longer necessary to continue the analysis.

Geometric nonlinearity. After a certain amount of displacement has occurred, the assumption of small-deformation theory are no longer valid. This leads to a significant error in the predicted load-displacement relationship. So a criterion for stopping the analysis at a point beyond which it is no longer accurate is necessary. This factor proved to be important in the current study, and the approximate means by which it was approached will be discussed in Sec. 4.6.

To simplify the analysis algorithm, it was decided to use the second factor above in terminating the impact analysis. From the results described in Sec. 4.6, the crash scenario analysis was truncated when the displacement, w, at the load application point reached the value:

$$w_{final} = \frac{1}{4} \cdot L \tag{4.1}$$

where L is the quarter-circumference of the fuselage.

Although a number of designs were still capable of carrying a finite amount of load at this level of deformation, it was assumed that the bulk of energy absorption had occurred prior to that point. Since, for preliminary design purposes, it was not necessary to predict the exact value of energy absorbed, it was felt that this assumption would allow various

designs to be ranked in a relative sense. Further, as the geometric nonlinearity increases, the axial load in each beam element increases. This would lead to earlier failure events than would be predicted using just the linear model. Thus, catastrophic failure of the entire structure could occur at a displacement close enough to the value shown in Eqn. 4.1 above that this assumption would be reasonably accurate.

Since crashworthiness in this effort was defined by the energy absorption capability of the fuselage sub-floor cross-section, the result of the progressive damage analysis provided all the information necessary to determine this. A simple integration of the force-displacement curve up to the termination point defined the energy absorption of the structure. That is:

$$E = \int_0^{w_{final}} F \cdot w dw \tag{4.2}$$

The second constraint, the limit on the peak load (see Sec. 1.1) can also be obtained directly from the force-displacement curve. Thus, the two crashworthiness parameters were easily obtained and were then available to evaluate the goodness of each design under consideration or the determine whether the design met the minimum criteria for crashworthiness.

4.5 Local Failure Modes

As discussed in the previous section on progressive failure, a key element of the crashworthiness analysis is the ability to accurately predict the failure of key skin or stiffener regions in the local model. The global model, having already been significantly reduced in detail from the local model, is not capable of accurately predicting local failure modes. By using the recovery process described in Sec. 3.4, the results from the global model are uti-

lized to determine the local stress state in each region within each global beam-type element. The local failure modes which were anticipated to be critical to the response of the fuselage structure are:

1. Rib Crippling
2. Rib Tensile Failure
3. Skin Buckling
4. Skin Failure
5. Skin-Stiffener Separation

In the remainder of this section, the models chosen to predict each of these local failure modes will be presented, and their implementation in the global-local analysis will be discussed.

4.5.1 Rib Crippling

This failure mode represents a local instability in a particular segment of a rib. The geometry of each rib segment can be reasonably approximated as a rectangular plate that is free along one side and elastically supported along the other. In order to simulate with reasonable accuracy the rib configurations to be considered in this study, the solution needs to incorporate the following features:

Orthotropic material properties - The manufacturing methods required for integrally-stiffened panels typically result in stiffeners in which the fibers are oriented parallel to the skin surface. Thus, the ribs will be specially orthotropic ($D_{11}=D_{22}$, $D_{16}=D_{26}=0$).

Combined bending-compression loading - The primary types of loading which could result in rib buckling are longitudinal bending and longitudinal compression. Thus, the solution must allow for any arbitrary combination of these

loads.

Elastic support at skin-stiffener interface - Since the boundary condition along the edge of the rib which intersects the skin are not exactly represented by either simply-supported (SS) or clamped (CL), it is desirable to have a solution which allows for some intermediate amount of fixity.

Free edge at top of rib - There is no fixity along the top, or free, edge of stiffener.

Simple supports on loaded sides - Although the actual fixity on the loaded transverse edges is neither simply-supported or clamped, it will be assumed for the purposes of this study that these edges are simply-supported. This is a conservative assumption, and allows a Levy-type buckling solution which simplifies the analysis considerably.

A schematic of the problem to be considered is shown in Fig. 4.6. A large number of researchers have considered buckling problems which incorporate some subset of the features mentioned above [105,106,107]. However, the author was unable to locate a solution incorporating all of these features in the available literature. This necessitated the development of a suitable solution for this problem.

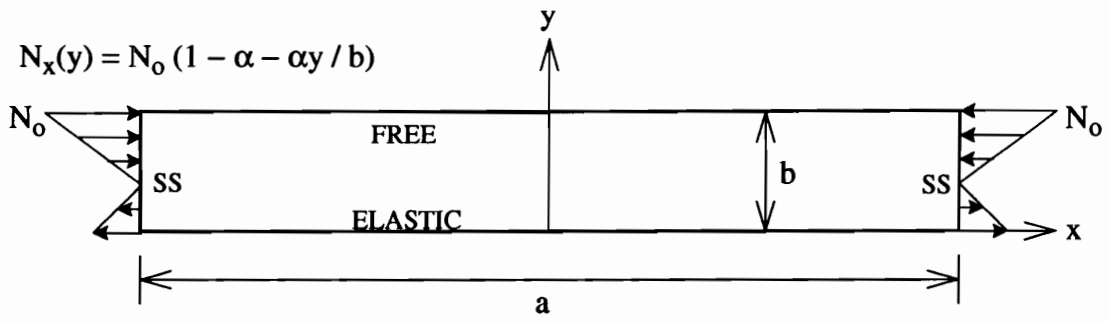

Figure 4.6 Schematic of rib buckling problem

It was decided to solve the problem using an energy-based approach coupled with the

Rayleigh-Ritz method. First, since the loaded ends of the rib ($x=0$ and $x=a$) are assumed to be simply supported, a Levy-type solution of the form

$$w(x, y) = f(y) \sin \frac{m\pi x}{a} \tag{4.3}$$

can be used. This fulfills automatically the simply-supported boundary condition at the loaded edges. It is then only necessary in the Rayleigh-Ritz method to choose a suitable function $f(y)$ in order to solve the buckling problem. In using energetic methods, it is only required to fulfill the geometric boundary conditions on the edge $y=0$. That is, the function need not fulfill exactly the free edge force-type boundary conditions on the top edge $y=b$.

The elastic rotational support at the skin-rib interface must be incorporated into the boundary condition along that edge. The first boundary condition is that no deflection occurs along that edge, or

$$w(x, 0) = 0 \tag{4.4}$$

Following the method discussed by Timoshenko[108], we can consider the skin-rib interface to be a torsion member with a torsional rigidity of C. Thus, the twisting moment at any cross-section of this interface along the x-axis is

$$C \cdot \frac{\partial^2 w}{\partial x \partial y} \tag{4.5}$$

The rate of change of this twisting moment is equal to the bending moment, M_y per unit length of the lower edge of the rib. Thus, the boundary condition along this rib edge ($y=0$) becomes for an orthotropic material:

$$-D_{12}\frac{\partial^2 w}{\partial x^2} - D_{22}\frac{\partial^2 w}{\partial y^2} = C \cdot \frac{\partial^3 w}{\partial x^2 \partial y} \tag{4.6}$$

If we substitute the expression for $w(x,y)$ from Eqn. 4.3 above and take advantage of the other boundary condition at that edge (Eqn. 4.4), we obtain the following form (at $y=0$):

$$D_{22}\frac{d^2f}{dy^2} = \left(\frac{m\pi}{a}\right)^2 C\frac{df}{dy} \tag{4.7}$$

After some trial and error, a final form for the function $f(y)$ was selected to be:

$$f(y) = K_1 y + K_2 y^2 + K_3 y^3 \tag{4.8}$$

This function fulfills automatically the deflection boundary condition $w(x,0)=0$. Upon substitution of this function into the elastic constraint boundary condition (Eqn. 4.6) it is found that the first two constants are not independent. The application of this boundary condition results in the final form of the displacement function as:

$$w(x,y) = \left[K_1\left(y+\varepsilon\frac{m^2\pi^2}{a}y^2\right)+K_3y^3\right]\cdot\sin\frac{m\pi x}{a} \tag{4.9}$$

where:

$$\varepsilon = \frac{1}{2a}\cdot\frac{C}{D_{22}} \tag{4.10}$$

Now that a suitable expression for the deflection $w(x,y)$ has been chosen, it can then be substituted into the strain energy formula. For an orthotropic plate, the strain energy is given by [109]:

$$U = \frac{1}{2}\iint\left[D_{11}\left(\frac{\partial^2 w}{\partial x^2}\right)^2 + 2D_{12}\frac{\partial^2 w}{\partial x^2}\cdot\frac{\partial^2 w}{\partial y^2} + D_{22}\left(\frac{\partial^2 w}{\partial y^2}\right)^2 + 4D\left(\frac{\partial^2 w}{\partial x\partial y}\right)^2\right]dxdy \tag{4.11}$$

As is shown in Fig. 4.6, the applied loading on the edges x=0 and x=a is assumed to be

a linear distribution given by:

$$N_x(y) = N_0(1 - \alpha - \alpha\frac{y}{b}) \tag{4.12}$$

Thus, by varying the parameter α, any combination of uniform compression and bending can be represented. For example, $\alpha=0$ would represent uniform compression, while $\alpha=2$ would represent pure bending. The work of external loads can then be computed by substituting this distribution of N_x into the expression:

$$W = \frac{1}{2}\iint N_x(\frac{\partial w}{\partial x})^2 dxdy \tag{4.13}$$

After substituting expressions for $w(x,y)$ and $N_x(y)$ into the formulae for strain energy and external work and carrying out the integration, the Total Potential Energy can be computed by the expression:

$$\Pi = U + W \tag{4.14}$$

Obtaining a solution for the buckling problem can be achieved by applying the Principle of Stationary Potential Energy, or

$$\delta\Pi = 0 \tag{4.15}$$

Performing this operation leads to a set of two simultaneous linear homogeneous equations in the unknown constants K_1 and K_3 in the form:

$$\begin{bmatrix} A - B(b^2N_0) & C - D(b^2N_0) \\ C - D(b^2N_0) & E - F(b^2N_0) \end{bmatrix} = \begin{bmatrix} 0 \\ 0 \end{bmatrix} \tag{4.16}$$

where:

$$A = D_{11}R^3(m\pi)^2 G - (D_{12} - 4D_{66})R^2\varepsilon(m\pi)^2\left[1 + \frac{2}{3}R\varepsilon(m\pi)^2\right] + 2D_{22}R\varepsilon^2(m\pi)^2 + 2D_{66}R$$

$$B = \frac{1}{24}R(4-\alpha) + \frac{1}{20}R^2\varepsilon(m\pi)^2(5-\alpha) + \frac{1}{60}R^3\varepsilon^2(m\pi)^4(6-\alpha)$$

$$C = D_{11}R^3(m\pi)^2\left[\frac{1}{10} + \frac{1}{12}R\varepsilon(m\pi)^2\right] - (D_{12} - 2D_{66})R - (D - 3D)R^2\varepsilon(m\pi)^2 + 3D_{22}\varepsilon$$

$$D = \frac{1}{60}R(6-\alpha) + \frac{1}{84}R^2\varepsilon(m\pi)^2(7-\alpha)$$

$$E = \frac{1}{14}R^3 D_{11}(m\pi)^2 - \frac{6}{5}(D_{12} - 3D_{66})R + \frac{6}{R(m\pi)^2}D_{22}$$

$$F = \frac{1}{112}R(8-\alpha)$$

$$G = \left[\frac{1}{6} + \frac{1}{4}R\varepsilon(m\pi)^2 + \frac{1}{10}R^2\varepsilon^2(m\pi)^4\right]$$

One solution to Eqns. 4.16 is $K_1=K_3=0$. This would lead to the result that $w=0$ everywhere which corresponds to the nonbuckled solution. Thus, the buckling solution is obtained by solving the eigenvalue problem, or forcing the determinant of the coefficient matrix to be zero. Thus, for a given number of buckled wavelengths (i.e. m), the buckling load can be determined from:

$$b^2 N_{0_{cr}} = \frac{AF + BE}{2} - CD \pm \sqrt{\frac{1}{4}(2CD - BE - AF)^2 - (BF - D^2)(AE - C^2)} \qquad (4.18)$$

where the lower value is chosen. The critical buckling load is obtained by determining the value of m which produces the lowest value for buckling load.

The predicted value for buckling load is then compared to the actual value of N_o in the global-local model. This value is obtained by using the recovery process described in Chapter 3 to find N_x at two or more heights along the rib. It is assumed that N_x varies linearly across the

height of the rib, so the values of N_o and α are determined in this manner.

4.5.2 Rib Tensile Failure

This failure mode represents an actual tensile failure of the rib material, resulting in a loss of load-carrying capability for that region. Since rib crippling is likely to occur under compressive loading, material failures are more likely to occur in areas subject to tensile or bending loads. As in the case of rib crippling discussed above, the local values of N_x are obtained from the global-local recovery process, and in conjunction with an assumption of linear variation, the maximum value of N_x at any point in the rib region is calculated. The tensile stress due to this load is then calculated and compared to the ultimate tensile strength of the rib material (in the axial direction of the rib) using:

$$(N_x^{rib})_{max} = \sigma_{ult}^{rib} \cdot t_r \tag{4.19}$$

The load required to cause the above criterion to be satisfied would be the rib tensile failure load, and is then compared to the other local failure loads to determine which, if any, failure modes will occur next.

4.5.3 Skin Buckling

As in the case of rib crippling, this mode represents a local instability in a particular segment of skin enclosed by the surrounding rib configuration. Since the present study focused on an isogrid-type or general unit grid-stiffened structure, the skin regions were strictly triangular. In fact, the skin regions can be classified as either isosceles triangles or right triangles, depending on the nature of the grid-stiffening (see Fig. 4.7). Bruhn[105] presents several design curves for triangular skin buckling of isotropic materials, most of which is based on the work of Wittrick[110] and Cox and Klein[111]. However, none of

these results proved directly applicable to the present model, as they were fairly limited to certain geometries and did not provide the generality required for the present design model. Thus, it was decided to use a numerical approach to generate a set of buckling curves for isosceles and right triangular isotropic skin sections.

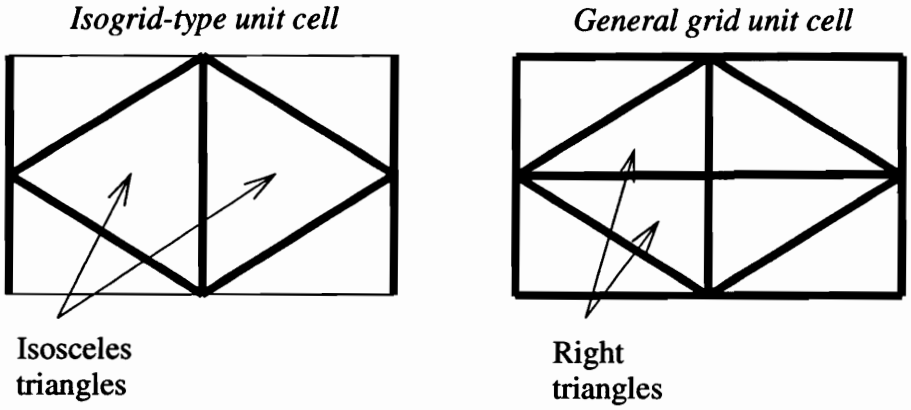

Figure 4.7 Triangular skin regions in isogrid and general grid unit cells

The commercial finite element analysis program MSC/NASTRAN for Windows was used to create models of both isosceles and right triangles of varying included angles. A typical mesh is illustrated in Fig. 4.8. Since most stresses generated during the crash event would be oriented along the hoop direction of the fuselage, the loads applied to these finite element models was limited to uniaxial loading in the directions shown schematically in Fig. 4.8. The edges of the triangles were assumed to be clamped. Although the true nature of the rib/skin connections is less rigid than that and the skin regions may in fact buckle at loads less than the predicted loads using clamped edges, it was felt that this would be partially or completely offset by the progressive failure model assumption of total reduction in stiffness. So, in terms of energy absorption, treating a region as failing later but losing all stiffness is roughly comparable to an earlier failure with some remaining stiffness.

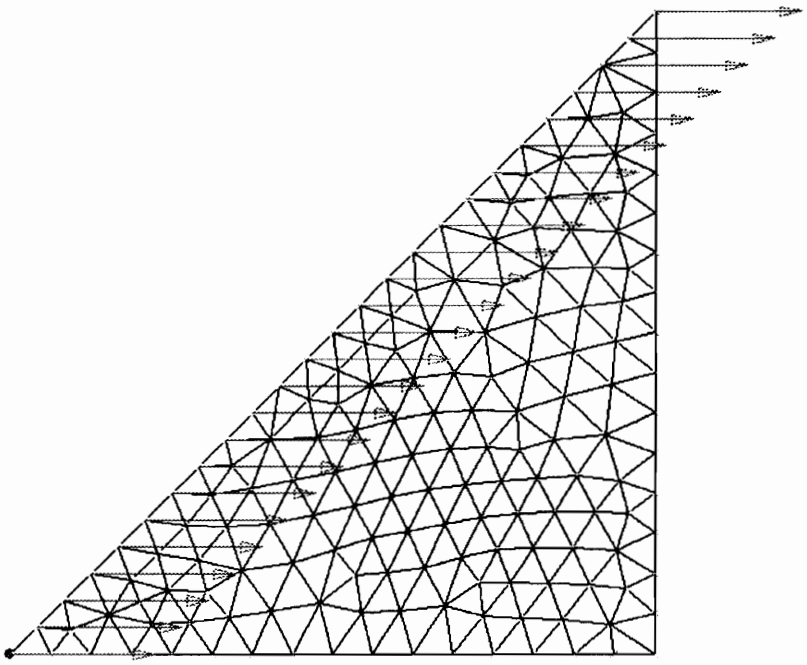

Figure 4.8 Typical mesh used in NASTRAN triangular buckling analysis

A number of different aspect ratio triangles were analyzed using the procedure described above. The resulting expression for buckling load for the two triangle types is:

$$(N_x)_{cr} = \frac{\beta D}{ah} \tag{4.20}$$

where the non-dimensional parameter β is shown for each case in Fig. 4.9.

4.5.4 Skin Failure

As in the case of rib tensile failure, this failure mode represents a material failure in a skin segment. Since skin buckling is likely to occur under compressive loading, skin failure is expected to occur in areas subject to tensile or bending loads. The method chosen for this failure model is a simple plate approach. Again, for the crashworthiness problem, only the axial load and bending in the hoop direction are considered. The global-local recovery process is used to calculate the axial load, N_x, and the bending moment, M_x near

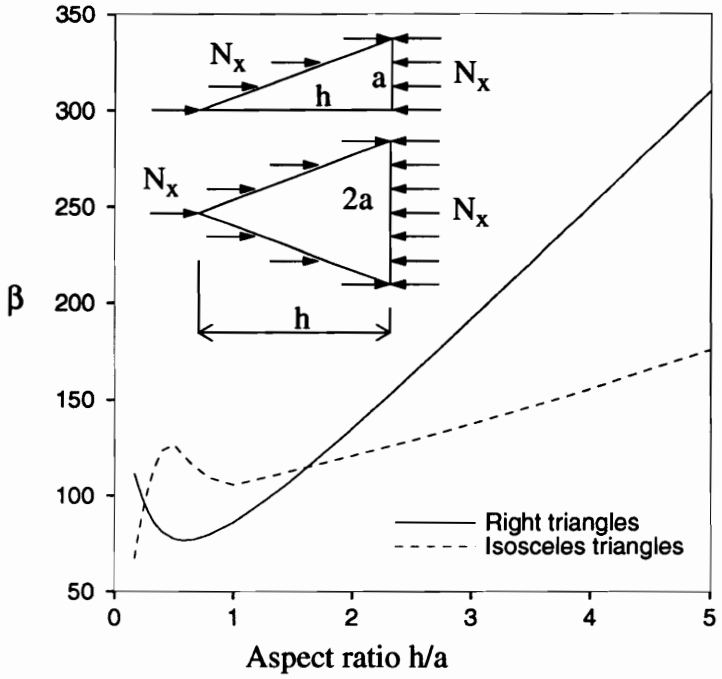

Figure 4.9 Buckling parameters β for triangular buckling

the center of each skin region. Then, simple plate stress expressions were used to calculate the maximum tensile stress in the skin. This was then compared to the ultimate tensile strength of the skin material to determine the required load to cause skin failure. This process is summarized by the criterion:

$$\frac{N_x}{h} + \frac{M_x(\frac{t}{2})}{D} = \sigma_{ult} \tag{4.21}$$

Again, the load required to cause this failure mode is then compared to the load factors for each of the other local modes to determine which, if any, will occur .

4.5.5 Rib/Skin Separation

This mode represents the tendency of the stiffeners to "peel" off of the skin surface.

This failure mode may be the most common, yet hardest to predict of these local failure modes. Again, since this effort was aimed at preliminary design, a fairly approximate method was assumed. Since the local model was built up of two-dimensional plate elements, there was already a significant simplification to the actual skin-stiffener interface. As in the case of rib crippling, the local stress (in this case perpendicular to the axial stiffener direction) was determined at two different heights within the stiffener. Using the assumption that this stress varies linearly, the local transverse stress in the rib in the neighborhood of the skin/rib interface is estimated. The ribs were assumed to be fabricated with the fibers all oriented parallel to the rib direction, so at least for composite ribs the strength perpendicular to the rib direction is fairly low. This strength is compared to the predicted local transverse stress to predict occurrence of rib separation using the criterion:

$$(N_y^{rib})_{max} = (\sigma_{ult}^{rib})_{trans} \cdot t_r \tag{4.22}$$

As above, this criterion is compared to each of the other local criteria to determine which, if any, are expected to occur.

4.6 Approximation of Geometrically Nonlinear Response

The global beam-type model and the local plate finite element model are both predicated on the assumption that deformations are small. Although certainly a crash event can involve significant large deformations of the fuselage structure, it was originally assumed for this study that most failure events, and therefore the bulk of the energy absorption, would occur at deformations where this assumption would be reasonable valid. The application of this approach to fuselage frames by Woodson[1] bore out this assumption. However, upon implementation of the progressive failure model described above, it was found

that for grid-stiffened structures, significant rigidity was sustained well into the large deformation regime. Thus, some method for incorporating these effects into the analysis was necessary. A full geometrically nonlinear analysis would have greatly increased the complexity and computational requirements of the crashworthiness analysis and would have made it somewhat impracticable for preliminary design purposes. Some means of approximating the important aspects of the geometric nonlinearity, particularly on the load history, was required.

To quantify the nature of the nonlinearity, a method presented previously by Sensmeier *et al*[112] and Griffin *et al*[113] was applied. This method uses a 22-degree-of-freedom wide-beam finite element for the large deflection analysis of layered beams. A finite element model identical to that used in the global model for the fuselage sub-floor was created. The predicted displacement-load response of a graphite-epoxy beam for a cylinder radius *R=85 in* are presented in Fig. 4.10. The displacement-load response for four radi-

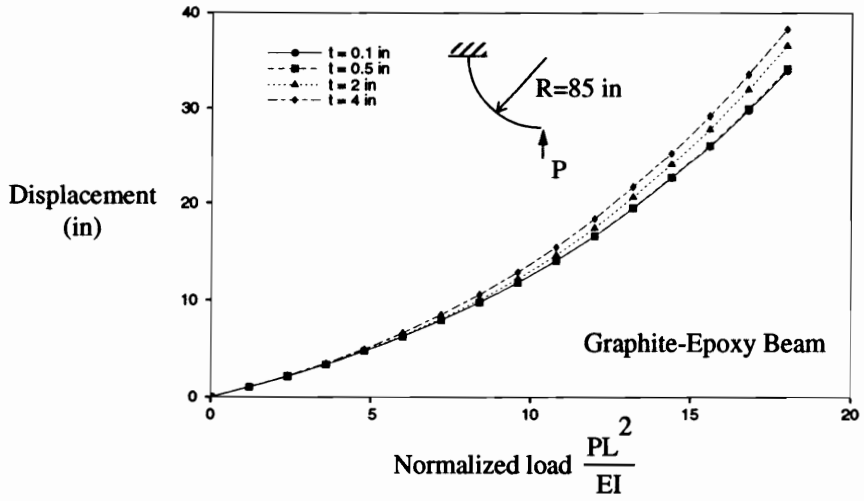

Figure 4.10 Nonlinear displacement-load relationship for graphite-epoxy beams.

cally different beam thicknesses collapse essentially onto one curve if one uses a load normalization of:

$$P_{norm} = \frac{PL^2}{EI} \tag{4.23}$$

where P is the applied load, L is the quarter-circumference of the fuselage, E is the elastic modulus of the material, and I is the section moment of inertia. For a thickness t=*0.1 in*, the displacement-load curve is shown for four radically different cylinder radii in Fig. 4.11. From these results, it is apparent that if the load normalization shown above is used in conjunction with a displacement normalization of

$$w_{norm} = \frac{w}{L} \tag{4.24}$$

the displacement-load response of any continuous beam structure can be predicted.

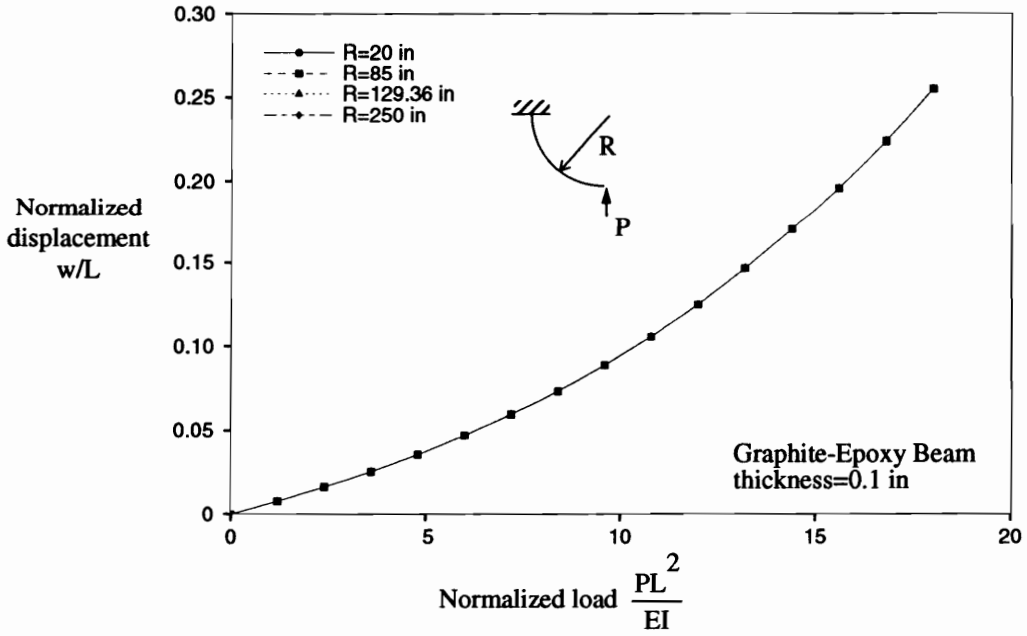

Figure 4.11 Nonlinear displacement-load relationship for graphite-epoxy beams.

For any displacement value, this method predicts the applied load for the geometrically nonlinear problem. The ratio of this nonlinear load to the expected linear load is plotted as a function of the normalized displacement in Fig. 4.12. Using this normalized

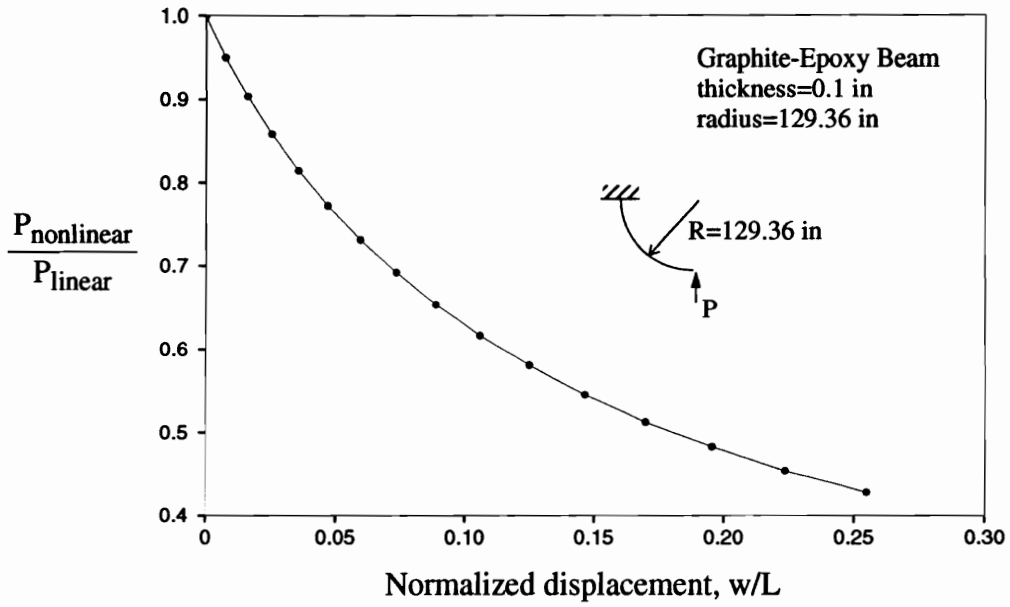

Figure 4.12 Ratio of nonlinear load to linear load for a graphite-epoxy beam

displacement, this relationship is unchanged for all continuous beams, regardless of the thickness or the radius of curvature of the initial shape. From this plot, it is apparent that at a normalized displacement of about 0.25, the error in the load prediction between the linear and nonlinear results is around a factor of two. To use this relationship as an approximation to the nonlinear problem in the current study, a few assumptions were made. They are:

A grid-stiffened fuselage structure behaves similarly to a continuous beam. The nonlinear method is specifically geared for a conventional layered beam. It is assumed that, at least in terms of nonlinear load response, that the grid-stiffened fuselage behaves in a similar beam-like fashion. This assumption is

already inherent in the global-local procedure. Local failure events will cause variations in the nonlinear response, but are not likely to affect the response to a significant extent prior to reaching the cutoff point of $w/L=0.25$.

Failure events are not affected by the nonlinear response. In the displacement regime considered, it is felt that the increase in axial load in each element due to nonlinearity will not appreciably alter the predicted occurrence of failure events.

Failure events will occur quickly beyond the cutoff displacement value. If this is true, very little energy will be absorbed beyond this point.

Using the load ratio - normalized displacement relationship from Fig. 4.12, the following procedure is used to estimate the nonlinear response of the grid-stiffened structure.

1. The next failure event is predicted. Using the global-local procedure and the local failure models described in this chapter, the load and displacement at the next failure occurrence is predicted. This value of the load is considered the linear load.

2. The displacement value at the next predicted failure event is normalized using Eqn. 4.24.

3. The nonlinear/linear load ratio for this normalized displacement is found from the relationship shown in Fig. 4.12.

4. The nonlinear load is calculated by multiplying the linear load by the load ratio corresponding to that displacement.

To illustrate this procedure, it was applied to a sample aluminum isogrid-reinforced fuselages and a sample composite isogrid-reinforced fuselage. The load-displacement results for these cases are shown in Figs. 4.13 and 4.14. It can be seen from these figures that the load levels are significantly lower in the nonlinear approximation than for the lin-

ear case, and further that the energy absorption (or area under the load-displacement curve) is much less. It is also apparent that incorporating the nonlinear approximation leads to a higher percentage of the energy absorption occurring early in the deformation history.

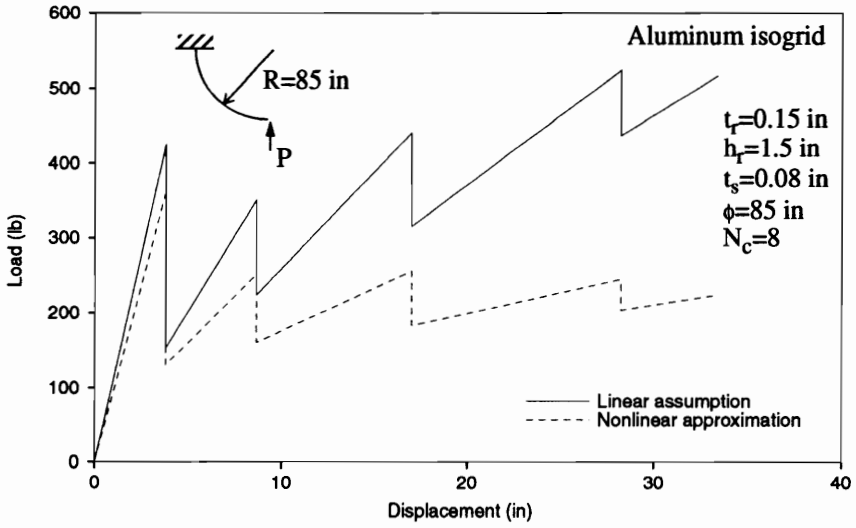

Figure 4.13 Comparison of linear and approximate nonlinear progressive failure curves for aluminum isogrid

Although the approximate nonlinear method which was presented here provides a good initial estimate for nonlinear effects in the crash sequence, its inherent assumptions must clearly break down at some point. For this reason, it is highly recommended that any designs selected through the preliminary design approach developed in this project be analyzed with a full geometrically nonlinear analysis to verify the energy absorption capability.

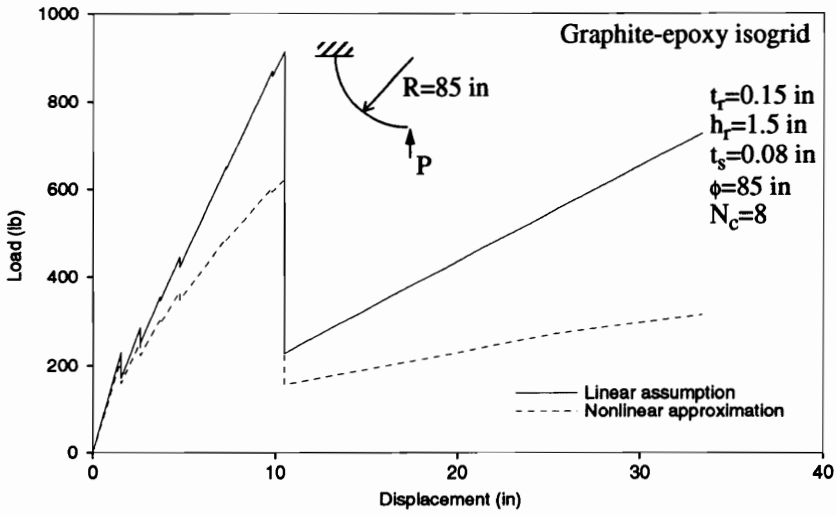

Figure 4.14 Comparison of linear and approximate nonlinear progressive failure curves for composite isogrid

5.0 Preliminary Design Tool for Grid-Stiffened Fuselage Structures

As stated in Chapter 1, the goal of this study was the development of a preliminary design tool for grid-stiffened composite fuselage structures which incorporates crashworthiness into the design process. As described in Chapters 3 and 4, a global-local method was developed and applied to crashworthiness analysis of these fuselages. With this method in hand, the only remaining task was to incorporate the crashworthiness analysis into an overall design tool which includes any other constraints governing the fuselage behavior. In this chapter, the development of this tool will be discussed, including selection of design variables and implementation of the optimization procedure. It is important to point out that the objective of this task was not to perform a trade study on fuselage designs, but to develop the design tool and demonstrate its applicability to grid-stiffened fuselage structures.

5.1 Overview of Preliminary Design Process

Preliminary design is, as its name implies, the earliest stage of the design process. Relatively simple analytical tools are employed to "rough out" from known requirements for a system a design, or family of designs, that are to be pursued farther along into the design sequence. The objective is not to select the definitive final design, but to begin to narrow the design space and limit the scope of configurations which must be analyzed using more detailed methods.

With this definition of preliminary design in mind, the global-local analysis method for fuselage crashworthiness estimation developed in this project was incorporated into a

preliminary design tool for fuselage design. Clearly, the global-local procedure is an approximate method, as there were a number of simplifying assumptions: the nonlinear approximation, the assumption of brittle failure modes, the application of simple models for local failure modes, and the use of plate elements in the local model rather than three-dimensional elements. Therefore, any results obtained using this approach must not be taken as conclusive. However, the global-local approach could prove extremely useful in the preliminary design process in determining how to design a fuselage which is as crash-worthy as is possible within the other constraints put on the design.

Recall the visual description of the global-local procedure that was shown in Fig. 3.1. This procedure was then embedded into a design optimization process that is shown schematically in Fig. 5.1. This process involves the crashworthiness estimation, weight evaluation, and other design requirements. It was desired to produce a preliminary design tool

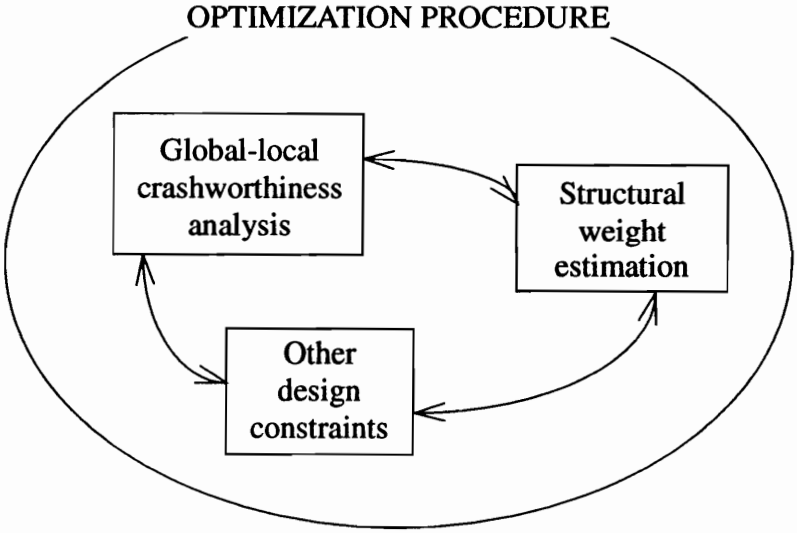

Figure 5.1 Schematic of preliminary design tool

which incorporated this process, allowing a designer to optimize either weight or crash-worthiness, using either of these as a constraint in addition to the other design constraints.

The details of this tool are discussed in Sec. 5.4 where the optimization procedure is presented and discussed.

5.2 Selection of Design Variables

Design variables are the parameters that, when specified, fully define a given design configuration. These can involve material specifications, geometrical parameters, manufacturing methods, etc. Much of the challenge of design is the selection of appropriate design variables. Design variables which, when varied, have little effect on whether or not the design meets the necessary constraints or optimization criteria can unnecessarily complicate the design process. However, neglecting design parameters that can significantly affect these constraints and optimization criteria can be significantly costly, both in time and the quality of the final design.

For the development of the preliminary design tool in the current study, several assumptions were made which limited the choice of design variables. These assumptions were:

-*Material is specified.* The material to be used for the fuselage will be specified by the designer before using the preliminary design tool. This does not mean that different materials may not be considered, just that the optimization process does not involve considering multiple materials simultaneously.

-*Blade-type stiffeners only are used.* Although it is possible to fabricate grid stiffeners which have a more complicated cross-sectional shape (e.g. t-section), for demonstration purposes it was decided to limit the design to simple rectangular cross-sections.

-*Geometry is constant.* The geometry of a unit cell does not change as one moves around the circumference of the fuselage. This is typical of most grid-stiffened

panels and cylinders to date, but does not necessarily have to be the case. The global-local procedure described in this study could easily be used to analyze geometry that changes in the circumferential direction. However, this would require more refined models for the other design requirements (see Sec. 5.3) than were utilized in the current study.

After making these assumptions, five design variables, all geometric, were chosen:

1. Rib thickness, t_r
2. Rib height, h_r
3. Skin thickness, t_s
4. Grid angle, ϕ
5. Grid spacing (actually, number of unit cells on quarter circumference, N_c)

These parameters are shown schematically in Fig. 5.2. These design variables were all expected to have significant impact on all three aspects of the design requirements: crashworthiness, weight, and the other constraints. To illustrate the effects of these design variables on crashworthiness, the key element of this project, several example configurations were analyzed. All of these involved aluminum isogrid-type reinforcement (although it is only a true isogrid when the grid angle, ϕ=60°)

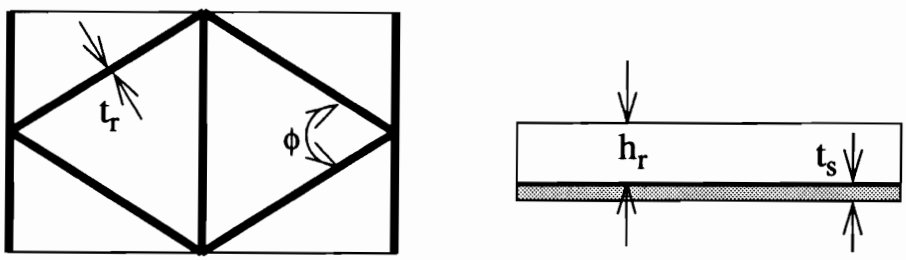

Figure 5.2 Schematic of geometric design variables

In Fig. 5.3, the effect of varying rib thickness on crash response is illustrated. (Note

that the loads and energies have been normalized per unit length of the fuselage.) From this plot, it appears that there is nearly a linear relationship between rib thickness and energy absorption.

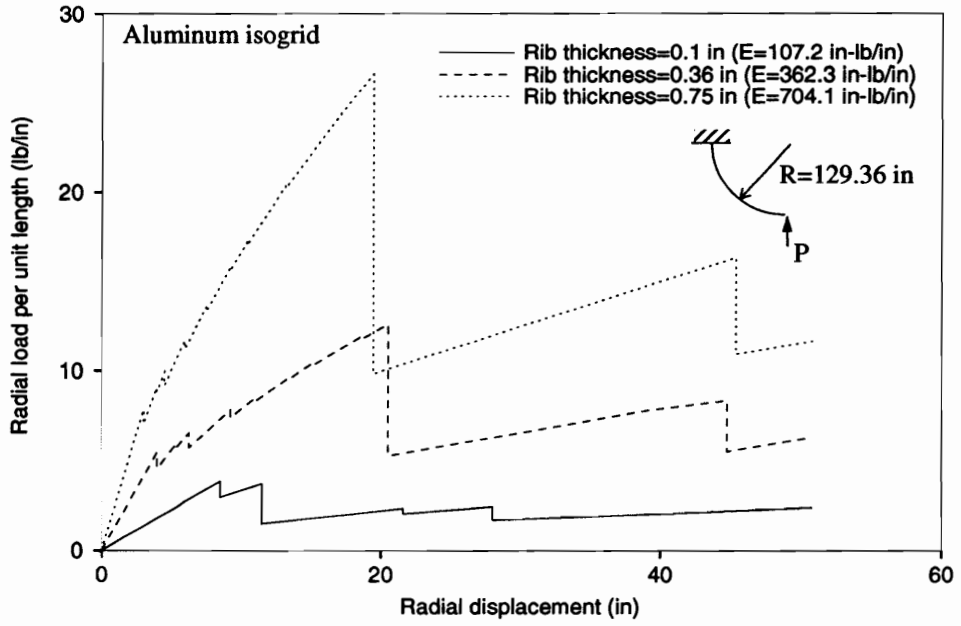

Figure 5.3 Effect of rib thickness on progressive failure response for aluminum isogrid-type fuselage (h_r=0.875 in, t_s=0.04 in, ϕ=60°, N_c=16)

In Fig. 5.4, the effect of varying rib height is illustrated. Clearly, increasing rib height yields a stiffer, more energy-absorbing structure. In fact, there is approximately a cubic relationship between energy and rib height for this example (which is not unexpected, since the bending moment of inertia of a stiffener is a cubic function of the rib height).

In Fig. 5.5, the effect of varying skin thickness is illustrated. Increasing the skin thickness does appear to increase energy absorbing capability, but the relationship is less than linear.

In Fig. 5.6, the effect of varying grid angle is illustrated. From this example, it is obvi-

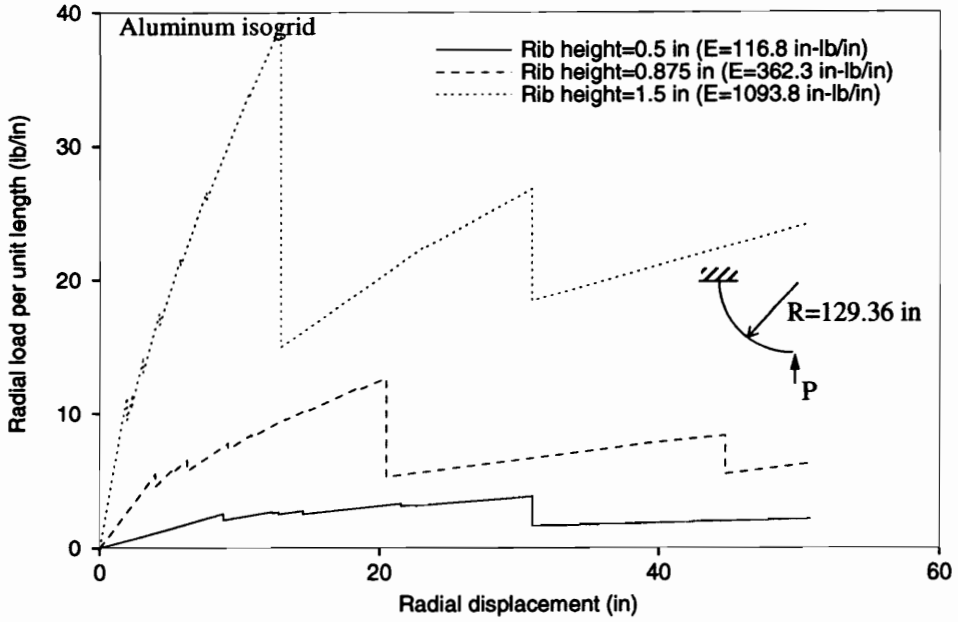

Figure 5.4 Effect of rib height on progressive failure response for aluminum isogrid-type fuselage (t_r=0.36 in, t_s=0.04 in, ϕ=60°, N_c=16)

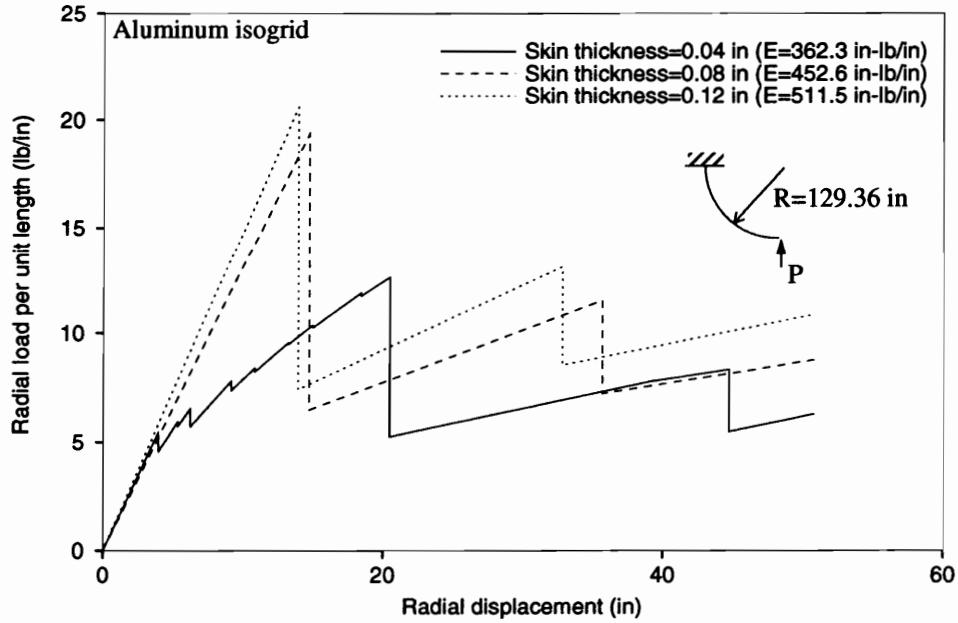

Figure 5.5 Effect of skin thickness on progressive failure response for aluminum isogrid-type fuselage (t_r=0.36 in, h_r=0.875 in, ϕ=60°, N_c=16)

ous that large grid angles (where the stiffeners are aligned mostly in the axial direction of the fuselage) will result in lower energy absorption.

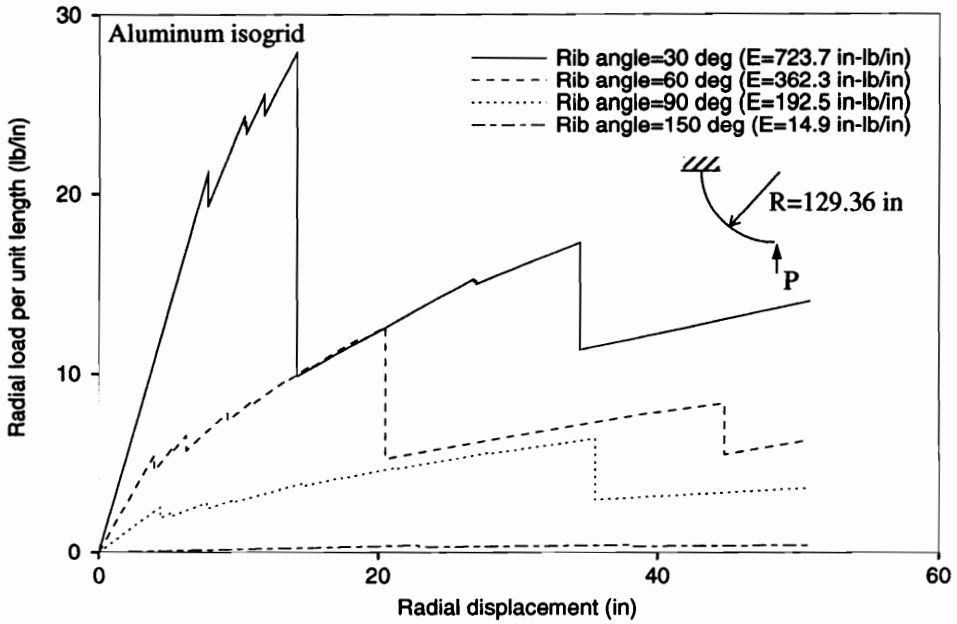

Figure 5.6 Effect of rib angle on progressive failure response for aluminum isogrid-type fuselage (t_r=0.36 in, h_r=0.875 in, t_s=0.04 in, N_c=16)

In Fig. 5.7, the effect of varying the grid spacing (or number of unit cells per quarter circumference) is illustrated. For this example, it appears that decreasing the grid spacing (increasing the number of cells) raises the energy absorption.

It should be pointed out here that the observations of these sample results are limited to the particular example considered. These trends may vary considerably when different baseline configurations or different materials are considered. They were placed here mainly to illustrate that varying the five selected design variables can significantly affect the impact response of the fuselage sub-floor.

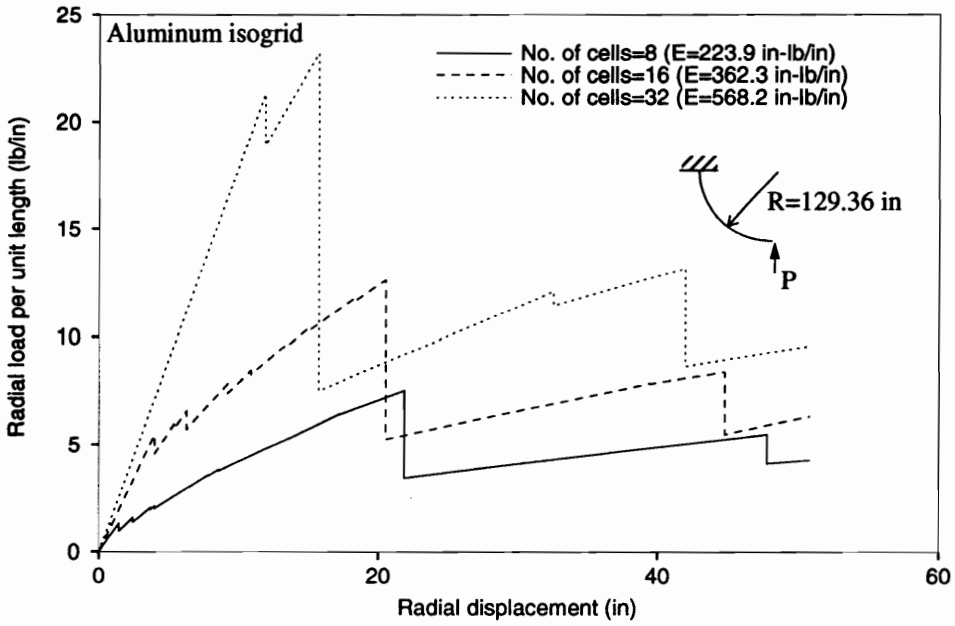

Figure 5.7 Effect of number of cells on progressive failure response for aluminum isogrid-type fuselage (t_r=0.36 in, h_r=0.875 in, t_s=0.04 in, ϕ=60°)

5.3 Other Design Requirements for Fuselages

The method described in Chapter 4 provides a useful tool to allow aircraft designers to incorporate crashworthiness effects into their designs at an early stage. However, it is important to note that crashworthiness, or energy absorption, is not the sole function of the fuselage structure. In fact, crashworthiness is not even the primary function. Optimizing crashworthiness (or developing a maximum crashworthiness capability) cannot be performed independently of the other structural requirements of the fuselage structure. Some of the other requirements of the fuselage in the aircraft design process are:

1. *Support aerodynamic and other bending loads.* The fuselage must not fail or buckle under the flight loads which would impart a bending moment to the structure.

2. *Support torsional loads.* Certain aircraft maneuvers can result in a state of tor-

sion in the fuselage. The structure must not fail or buckle under this type of loading as well.

3. *Operate as a pressure vessel.* Particularly on large transport aircraft, cabins must be pressurized during high-altitude flight. The fuselage structure is the primary support mechanism for this pressure.

There are many other requirements on fuselage structures, but these are some of the more critical (i.e.primary) types. These constraints must be added to the optimization process for the designer to come up with a usable preliminary design. Since the primary objective of this effort was to develop a tool for preliminary design incorporating a crashworthiness criterion, simple models were chosen to incorporate these primary constraints. A number of models for these types of problems were discussed in Chapter 2. Suitable models, which reasonably incorporated the differences between the designs considered in the optimization scheme were selected and built into the optimization code. These models were included in a modular fashion, so that it would be easy for a subsequent investigator to replace them with more sophisticated models if desired.

Predictive models were chosen for three different load requirements which would be important in a fuselage design. These load types were:

1. Bending loads
2. Torsional loads
3. Pressure loads

In the remainder of this section, the models chosen for each of these failure modes are presented and discussed.

5.3.1 Bending Loads

In a typical aircraft, most of the lift (which offsets the aircraft's weight) is generated by aerodynamic forces distributed along the wings. The fuselage generally carries only a small portion of this distributed load. However, the fuselage is subjected to very high concentrated load at the wing attachment and other attachments, such as the horizontal tail, vertical stabilizer, and landing gear. Further, a substantial percentage of the weight in an aircraft is carried in the fuselage. This is particularly true for a large transport aircraft, which may carry up to several hundred passengers. Under typical flight conditions, the wings exert an upward lifting force on the fuselage, while the weight of the fuselage and its components act in a downward direction. The result of this combination of loads is a large bending moment on the fuselage structure. If the aircraft is accelerating upward, its load factor (i.e. ratio of lift to weight) can cause this bending load to be even larger. Thus, it is crucial for the fuselage to be designed to withstand very large bending moments.

To incorporate this design requirement into the current optimization scheme, several potential failure modes had to be considered. These were:

1. *Global bending failure.* The fuselage must be capable of supporting the bending loads without failure of the skin or ribs.

2. *Global bending buckling.* The fuselage must be capable of supporting the bending loads without a loss of global stability.

3. *Local rib crippling under bending.* The fuselage must be capable of supporting the bending loads without local crippling failure of the grid-type stiffeners.

Local buckling of the aircraft skin between the stiffeners could also be incorporated in the design model. However, since most of the flexural rigidity of an aircraft structure is provided by the stiffeners, local skin buckling was not felt to be important enough to consider in this preliminary effort. In fact, skin sections often undergo buckling to some

degree during regular aircraft operations. (It must be noted here, though, that skin buckling events can be significant during the deformation and failure that accompanies a crash event. This leads to a contribution to the total energy absorbed during impact that cannot be neglected and was included in the crashworthiness estimation procedure described earlier.)

The failure models for each of the three bending failure modes listed above are described in this section.

5.3.1.1 Global Bending Failure

Under the effects of a large bending moment, the fuselage must be designed in such a way that material failure of either the skin or the ribs should not occur. The simplest method to predict this type of failure is to treat the fuselage as a simple beam and use a traditional Euler-type bending solution. For the purposes of this study, the fuselage skin/stiffener arrangement was idealized as a simple circular cylinder. However, to be relevant to the current design tool, the effect of varying grid arrangements and dimensions had to be included. This was accomplished by calculating an effective thickness and effective modulus of the skin and stiffener together[105].

The effective stiffness of the skin/stiffener hybrid was determined using a grid unit cell approximation coupled with constitutive equations, analogous to classical lamination theory, based on those presented for a general grid configuration by Reddy *et al*[5]. For the general unit cell shown in Fig. 5.8, the inplane stiffness matrix [A] from lamination theory

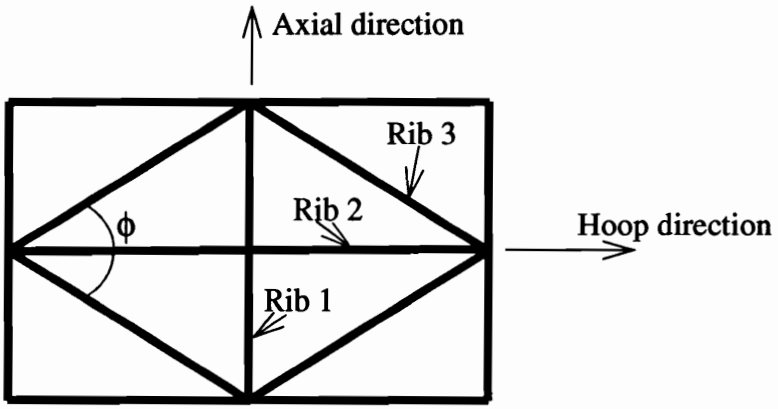

Figure 5.8 General grid unit cell definition used for estimating effective properties [5]

can be approximated by:

$$\begin{bmatrix} N_x \\ N_y \\ N_{xy} \end{bmatrix} = \begin{bmatrix} A_{11} & A_{12} & 0 \\ A_{12} & A_{22} & 0 \\ 0 & 0 & A_{66} \end{bmatrix} \begin{bmatrix} \varepsilon_x \\ \varepsilon_y \\ \gamma_{xy} \end{bmatrix} \tag{5.1}$$

where:

$$A_{11} = E_s t_s + \frac{2E_1 A_1}{a} + \frac{2E_3 A_3 \left(\sin\frac{\phi}{2}\right)^3}{a}$$

$$A_{12} = E_s \nu_s t_s + \frac{2E_3 A_3 \cos\frac{\phi}{2} \left(\sin\frac{\phi}{2}\right)^2}{a}$$

$$A_{22} = E_s t_s + \frac{2E_2 A_2}{b} + \frac{2E_3 A_3 \left(\cos\frac{\phi}{2}\right)^3}{b}$$

$$A_{66} = G_s t_s + \frac{2E_3 A_3 \left(\cos\frac{\phi}{2}\right)^2 \sin\frac{\phi}{2}}{b} + \frac{2E_3 A_3 \left(\sin\frac{\phi}{2}\right)^2 \cos\frac{\phi}{2}}{a}$$

From these expressions, the effective inplane stiffnesses of the stiffened skin can be

estimated for various configurations (e.g. isogrid, orthogrid) by adjusting the appropriate geometric parameters. For this analysis, coupling between bending and stretching (the [B] matrix in laminate theory) was neglected. Here, the axial direction of the fuselage was assumed to be the 1-direction. The effective stiffness of the fuselage can then be estimated by:

$$E_{eff} = \frac{A_{11}}{t_{eff}} \tag{5.2}$$

where t_{eff} is the effective thickness of the skin/stiffener hybrid. A simple rule-of-mixtures type approach was used to determine this thickness as:

$$t_{eff} = t_s + \frac{2t_r h_r}{b} \tag{5.3}$$

For the circular cylinder approximation, the maximum strain in the fuselage section occurs at the largest distance from the cylinder axis. Thus, the maximum magnitude of the strain is given by:

$$\varepsilon_{max} = \frac{MR}{E_{eff} I} \tag{5.4}$$

where M is the bending moment, R is the outer radius of the fuselage and I is the area moment of inertia of the approximate cross section and is given by $\pi[R^4-(R-t_{eff})^4]/4$.

Once the maximum value of the strain is determined, the maximum stress in the skin and stiffeners can be estimated by:

$$(\sigma_s)_{max} = E_s \varepsilon_{max} \qquad (\sigma_r)_{max} = E_r \varepsilon_{max} \tag{5.5}$$

If the tensile strength of the skin and ribs are, respectively, σ^s_{ult} and σ^r_{ult}, the bending

moment on the fuselage that will cause failure of each component is given by:

$$(M_{max})_{skin} = \frac{\sigma^{s}_{ult} I}{R} \qquad (M_{max})_{rib} = \frac{\sigma^{r}_{ult} I}{R} \tag{5.6}$$

Using this approach, the maximum bending capacity for material failure of each component is computed and compared to the given load requirements.

5.2.1.2 Global Bending Buckling

In the preceding section, the simple model used to predict material failure of a fuselage under bending was presented. However, even if a fuselage can be designed to avoid material failure under bending, it may still fail through a loss of global stability, or buckling. This mode is particularly important for a thin shell-type structure such as a fuselage. The resistance to buckling is provided primarily by the flexural stiffness of the stiffeners.

Many researchers have investigated the buckling of grid-stiffened plates and shells. A number of these approaches were presented in Chapter 2. For the purposes of this study and the preliminary design tool developed herein, a very simple approach was taken. The stiffened fuselage was assumed to be a homogeneous, orthotropic cylinder (as was the assumption for the bending failure model). This assumption again neglects the bending-extension coupling. However, this allows for a fairly simple computation of buckling strength in a trade study, while still incorporating the effects of varying stiffener configurations.

For an orthotropic circular cylinder, the Donnell-Mushtari-Vlasov shell equations of

motion including the effects of axial compressive load, N_{11}, are [114]:

$$D_{11}\frac{\partial^4 u_3}{\partial x^4}+\frac{2\,(D_{12}+2D_{66})}{R^2}\frac{\partial^4 u_3}{\partial x^2\partial\theta^2}+\frac{D_{22}}{R^4}\frac{\partial^4 u_3}{\partial\theta^4}+\frac{1}{R}\frac{\partial^2\phi}{\partial x^2}+N_{11}\frac{\partial^2 u_3}{\partial x^3}=0$$
$$\left(\frac{A_{12}^2-A_{11}A_{22}}{R}\right)\frac{\partial^2 u_3}{\partial x^2}+A_{11}\frac{\partial^4\phi}{\partial x^4}+\frac{A_{11}A_{22}-A_{12}^2-2A_{12}A_{66}}{A_{66}R^2}\frac{\partial^4\phi}{\partial x^2\partial\theta^2}+\frac{A_{22}}{R^4}\frac{\partial^4\phi}{\partial\theta^4}=0 \tag{5.7}$$

where u_3 is the radial deflection of the cylinder and D_{ij} are its flexural stiffnesses. These flexural stiffnesses can be estimated using the same procedure used above to estimate A_{ij}. The resulting expressions for these stiffnesses are:

$$\begin{bmatrix}M_x\\M_y\\M_{xy}\end{bmatrix}=\begin{bmatrix}D_{11}&D_{12}&0\\D_{12}&D_{22}&0\\0&0&D_{66}\end{bmatrix}\begin{bmatrix}\kappa_x\\\kappa_y\\\kappa_{xy}\end{bmatrix} \tag{5.8}$$

where:

$$D_{11}=\frac{E_s t_s^3}{12\,(1-\nu_s^2)}+\frac{2E_1I_1}{a}+\frac{2E_3I_3\,(\sin\frac{\phi}{2})^3}{a}$$

$$D_{12}=\frac{E_s\nu_s t_s^3}{12\,(1-\nu_s^2)}+\frac{2E_3I_3\cos\frac{\phi}{2}\,(\sin\frac{\phi}{2})^2}{a}$$

$$D_{22}=\frac{E_s t_s^3}{12\,(1-\nu_s^2)}+\frac{2E_2I_2}{b}+\frac{2E_3I_3\,(\cos\frac{\phi}{2})^3}{b}$$

$$D_{66}=\frac{G_s t_s^3}{12}+\frac{2E_3I_3\,(\cos\frac{\phi}{2})^2\sin\frac{\phi}{2}}{b}+\frac{2E_3I_3\,(\sin\frac{\phi}{2})^2\cos\frac{\phi}{2}}{a}$$

The solution of this equation is made more complicated if N_{11} varies with θ, as it does for bending. To keep this problem simple yet still reasonably accurate, the decision was made to consider the buckling of the cylinder under a uniform axial compression rather than pure bending. Buckling test data reported by Bruhn[105] show that, for the range of cylinder geometries typical of fuselages, buckling stress due to bending is consistently about 10-20% higher than buckling stress for pure compression. So the compressive buckling problem was solved, and the buckling stresses were increased by 20% to approximate this difference.

It was assumed for this simple analysis that the ends of the cylinder are simply-supported. This allows for an approximate Raleigh-type solution, where displacements of the form

$$\begin{aligned} u_3(x,\theta) &= U_{mn}\sin\frac{m\pi x}{L}\cos n(\theta-\phi) \\ \phi(x,\theta) &= \Phi_{mn}\sin\frac{m\pi x}{L}\cos n(\theta-\phi) \end{aligned} \tag{5.9}$$

are assumed, where m and n denote the number of buckling waves in the axial and hoop directions, respectively, L is the length of the cylinder, U_{mn} is the deflection amplitude, and ϕ is a phase angle. By substituting this expression into Eqns. 5.7 and 5.8 above, we obtain a system of two equations:

$$\begin{aligned} D_{11}\left(\frac{m\pi}{L}\right)^4 + 2(D_{12}+2D_{66})\left(\frac{n}{R}\frac{m\pi}{L}\right)^2 + D_{22}\left(\frac{n}{R}\right)^4 - N_{11}\left(\frac{m\pi}{L}\right)^2\Bigg]U_{mn} - \left(\frac{m\pi}{L}\right)^2\frac{\Phi_{mn}}{R} = 0 \\ \frac{A_{11}A_{22}-A_{12}^2}{R}\left(\frac{m\pi}{L}\right)^2 U_{mn} + \left[A_{11}\frac{m\pi}{L}^4 + C\frac{n}{R}\frac{m\pi}{L}^2 + A_{22}\frac{n}{R}^R\right]\Phi_{mn} = 0 \end{aligned} \tag{5.10}$$

where:

$$C = \frac{A_{11}A_{22} - A_{12}^2 - 2A_{12}A_{66}}{A_{66}}$$

These equations can be expressed in a simple form as:

$$\begin{aligned} \left(K_1 - \left(\frac{m\pi}{l}\right)^2 N_{11}\right) U_{mn} + K_2 \Phi_{mn} = 0 \\ K_3 U_{mn} + K_4 \Phi_{mn} = 0 \end{aligned} \tag{5.11}$$

where:

$$K_1 = D_{11}\left(\frac{m\pi}{L}\right)^4 + 2\left(D_{12} + 2D_{66}\right)\left(\frac{n}{R}\frac{m\pi}{L}\right)^2 + D_{22}\left(\frac{n}{R}\right)^4 - N_{11}\left(\frac{m\pi}{L}\right)^2$$

$$K_2 = -\frac{1}{R}\left(\frac{m\pi}{L}\right)^2$$

$$K_3 = \frac{A_{11}A_{22} - A_{12}^2}{R}\left(\frac{m\pi}{L}\right)^2$$

$$K_4 = A_{11}\frac{m\pi}{L}^4 + C\frac{n}{R}\frac{m\pi}{L}^2 + A_{22}\frac{n}{R}^R$$

For a given combination of buckling waves *m,n* the only non-trivial solution to these equations occurs when the determinant of the matrix is zero. This results in an expression for the buckling load:

$$(N_{11})_{cr} = \frac{K_1 K_4 - K_2 K_3}{\left(\frac{m\pi}{L}\right)^2 K_4} \tag{5.12}$$

This expression is evaluated for various combinations of m and n, with the actual buckling load equal to the lowest value for any combination. The bending moment which causes

buckling is then estimated by:

$$(M_{max})_{buck} = \frac{1.2\,(N_{11})_{cr} I}{R} \tag{5.13}$$

This value is the compared to the required load capability to evaluate the fitness of a given design.

5.3.1.3 Local Rib Crippling

The preceding two sections have described simple models for global bending failure and buckling. For some configurations, though, local crippling of the ribs may precede any material failure or global loss of stability. Since the ribs are the primary source of fuselage flexural stiffness, this result would be unacceptable. Thus, local rib crippling due to regular flight loads (as opposed to just impact loads considered in the crashworthiness model) was also considered as a design requirement. A suitable rib crippling model was already developed and presented in Sec. 4.5.1. That model was implemented for this failure mode as well.

5.3.2 Torsional Loads

Although the bending loads discussed in the previous section are expected to be the most critical for a typical fuselage structure, significant torsional loading can occur and must be accounted for in the design. These loads typically occur from aircraft maneuvers, where the lift on one wing is not necessarily the same as the lift on the other wing. The inertia of the massive fuselage then results in a torsional moment within the fuselage cylinder. Also, inertial torsional loads can occur during uneven landings, as well as wind gusts and many other causes. Thus, the fuselage must be designed to withstand appreciable torsional loads without material failure or buckling. The simple models selected to pre-

dict these capabilities are discussed in the following sections.

5.3.2.1 Torsional Failure

Just as in the case of bending, the fuselage must withstand the required torsional loading without material failure of either the skin or the ribs. The model selected for torsion was directly analogous to the one described for bending. The fuselage is approximated as a thin-walled circular cylinder, where the effective shear stiffness is estimated by:

$$G_{eff} = \frac{A_{66}}{t_{eff}} \tag{5.14}$$

where A_{66} is given by Eqn. 5.1. Then, the maximum shear strain in the cylinder is given by:

$$\gamma_{max} = \frac{TR}{G_{eff}J} \tag{5.15}$$

where J is the polar moment of inertia of the cylinder and is given by $\pi[R^4-(R-t_{eff})^4]/2$. The maximum shear stress in the skin can then be found from:

$$(\tau_{max})_s = G_s\gamma_{max} \tag{5.16}$$

The ribs, however, support torsional load by stretching. Thus, torsional strain in the fuselage results in normal stress in the ribs. From a strain transformation, the axial stress in the ribs due to a torsional load on the fuselage can be estimated by:

$$\sigma_r = E_r\gamma_{max}\frac{1}{2}\sin\phi \tag{5.17}$$

From these expressions, the maximum torsional moment capability of the stiffened fuse-

lage can be predicted by:

$$(T_{max})_{skin} = \frac{\tau_{s_{ult}} G_{eff} J}{G_s R} \qquad (T_{max})_{rib} = \frac{2\sigma_{r_{ult}} G_{eff} J}{E_r R \sin\phi} \tag{5.18}$$

5.3.2.2 Torsional Buckling

The model selected for predicting fuselage buckling under torsional loads was essentially the same as that presented above for bending (actually axially compressive) buckling. The Rayleigh-type assumed displacement function approach was used, along with the aforementioned assumption of simply supported ends. This allowed the use of the prescribed displacement field, as presented by Timoshenko and Gere[108] as:

$$\begin{aligned} u_3(x,\theta) &= U_{mn} \sin\left(\frac{m\pi x}{L} - n\theta\right) \\ \phi(x,\theta) &= \Phi_{mn} \sin\left(\frac{m\pi x}{L} - n\theta\right) \end{aligned} \tag{5.19}$$

Substituting these displacement expressions into the Donnell-Mushtari-Vlasov equations of motion (Eqn's. 5.7 and 5.8) result in the eigenvalue problem:

$$\begin{aligned} \left(K_1 - 2n\left(\frac{m\pi}{l}\right) N_{11}\right) U_{mn} + K_2 \Phi_{mn} = 0 \\ K_3 U_{mn} + K_4 \Phi_{mn} = 0 \end{aligned} \tag{5.20}$$

where K_1, K_2, K_3 and K_4 are identical to the compressive buckling case described above. The solution to these equations provides the torsional (or shear) buckling value:

$$(N_{12})_{cr} = \frac{K_1 K_4 - K_2 K_3}{2\frac{n}{R}\left(\frac{m\pi}{L}\right) K_4} \tag{5.21}$$

The applied torque which would cause buckling can then be estimated from:

$$(T_{max})_{buck} = \frac{(N_{12})_{cr} J}{R} \tag{5.22}$$

This value is then compared to the required buckling load capacity of the structure.

5.3.3 Pressure Loads

In addition to bending and torsional loads, fuselages typically are required to act as pressure vessels. Aircraft, particularly large transports, require cabin pressurization while flying at high altitudes. Bending loads require primarily axial stiffness or strength and torsional loads require primarily shear stiffness or strength. Pressure loads provide the primary impetus for circumferential strength. The simple model selected for this loading is again analogous to those used for bending and torsional strength. The fuselage is assumed to be a homogeneous circular cylinder undergoing a pressure load. The potential effects of the ends of the fuselage, which would create an axial stress, were neglected. Attention was focused, instead, on the hoop stresses. The effective stiffness of the stiffened skin was taken from the approach described previously as:

$$E_{efe} = \frac{A_{22}}{t_{eff}} \tag{5.23}$$

Using this results, the hoop strain caused by a gage pressure, p, would be

$$\varepsilon_{hoop} = \frac{pR}{E_{eff} t_{eff}} \tag{5.24}$$

Then, the stresses in the skin and ribs would be:

$$(\sigma_s)_{hoop} = E_s \varepsilon_{hoop} \qquad (\sigma_r)_{hoop} = E_r \varepsilon_{hoopx} \tag{5.25}$$

From this result, the maximum pressure capacity of the skin and ribs can be expressed as:

$$(p_{max})_{skin} = \frac{\sigma_{s_{ult}} E_{eff} t_{eff}}{E_s R} \qquad (p_{max})_{rib} = \frac{\sigma_{r_{ult}} E_{eff} t_{eff}}{E_r R} \tag{5.26}$$

The lower of these two values is the pressure-carrying capability of the fuselage and can then be compared to the pressure load requirements.

5.4 Development of Genetic Algorithm for Optimization

With a method in hand for modeling the crushing of a grid-stiffened fuselage structure and having selected the design variables, it remained only to select and apply an optimization process to develop the desired preliminary design tool. The design problem under consideration, due primarily to its use of composite materials and limits on the variation of the grid configurations due to manufacturing constraints, suggests a natural application of a genetic algorithm. In fact, this was the method selected by Woodson[1] in his design code for beam-type fuselage frames. The success he demonstrated helped lead to the selection of this method for the current project as well. Woodson also presented an excellent general description of genetic algorithms. Rather than repeat that description here, an overview will be presented and the application of the genetic algorithm to the current problem will be discussed.

Genetic algorithms, originally suggested by Holland[115], simulate the natural selection process in biology. Darwin's survival of the fittest principle suggests that creatures who have traits that make them more likely to survive and breed, pass those traits on to future generations. Thus, the beneficial traits will persist through generations, while traits which are not beneficial to survival will result in offspring less likely to survive and breed.

Thus, these detrimental traits will not persist in the species. Genetic algorithms are merely a mathematical representation of this biological process, where design traits which result in poor designs are less likely to survive the design process, while traits which result in good designs are more likely to survive.

In biology, genetic characteristics are passed from generation to generation through chromosomal strings, or DNA. In genetic algorithms, design information is passed down using analogous mathematical strings. The means for transmitting this information from reproducing biological parents to their offspring can involve such methods as crossover and mutation. These methods are mimicked in the genetic algorithm as well.

Genetic algorithms have several inherent advantages over traditional optimization procedures. Since a population of designs is maintained rather than a single design point, there is less risk of finding a local optimum rather than the global optimum. Also, genetical algorithms are particularly well-suited for cases where simple analytical functions do not exist for the design evaluations. In these cases, derivative information that is required for many optimization methods can be very difficult to determine. For this reason also, genetic algorithms are particularly useful for nonlinear or discontinuous design space.

There is a drawback to the genetic algorithm process as well. Since the method involves a whole population of designs that evolves over a number of generations, it can require a very large number of analyses. For this reason, it is necessary to have analytical methods that are computationally efficient. Thus, it is vital to have tools such as the global-local crashworthiness analysis developed in this study.

In genetic algorithms, a population of designs is maintained at each generation. Each design within this population is considered an individual. Each individual (or design) is

stored as a design string, paralleling the DNA string in biological creatures. These individual designs are evaluated using a fitness function, which describes their relative goodness in terms of the desired characteristics.

When the fitness of each member of a population is known, probabilistic methods are utilized to guide the better members to reproduce and create the population of the next generation. This process continues until a convergence criterion is met. This probabilistic nature ensures that the process is not random, but is actually steered towards improving designs.

Genetic algorithms do not actually use the design variables themselves, but rather use a coding of these variables. The most common coding is the use of binary integers (0 and 1) set into a string which represents a larger range of integers. This coding was used in this project, and the selected DNA string for a given design is shown in Fig. 5.9

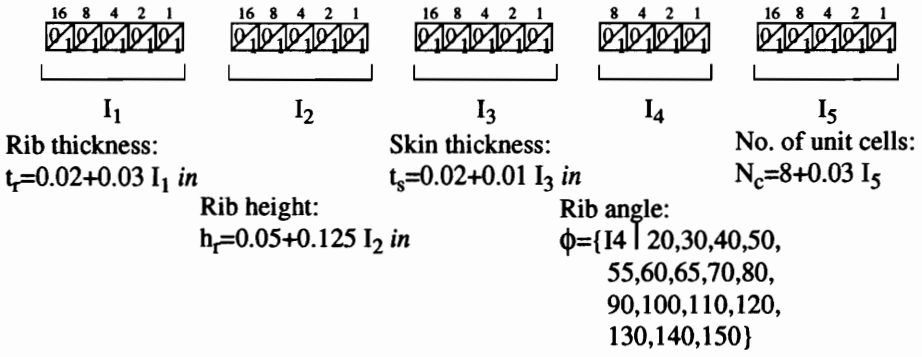

Figure 5.9 Definition of design string for genetic algorithm

Fig. 5.9 illustrates how this binary coding can be used to represent both a range of integer values (in the case of number of cells) and to simulate a continuous range (the rib or

skin dimensions). An example application of this DNA description is shown in Fig. 5.10.

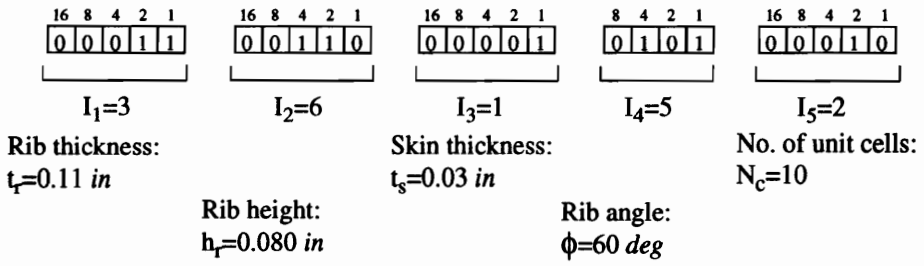

Figure 5.10 Example design string for genetic algorithm

With the design string coding selected, the genetic algorithm was then coded. The algorithm goes through the following steps:

1. Generation of initial population
2. Fitness evaluation
3. Ranking of population based on fitness
4. Selection of parents
5. Reproduction
6. Mutation

Steps 2 through 5 are then repeated until convergence is obtained, typically after some number of generations has passed with no improvement in design. Each of these steps will be discussed below.

1. Generation of Initial Population. For each member of the initial population (the size of which is specified by the user), the binary digits, or alleles, of the design string are selected randomly. Specifically, a random number between 0 and 1 is chosen, and the

allele is defined by:

$$allele = \begin{cases} 0 & \text{if} \quad rnd < 0.5 \\ 1 & \text{if} \quad rnd \geq 0.5 \end{cases} \tag{5.27}$$

where *rnd* is a random number between 0 and 1.

Thus, a random population set is created. If any "hard" constraints are present (hard constraints are those for which no member of a population is allowed if it violates this constraint), any member which violates any of these hard constraints is eliminated and a new member is selected. This process continues until a full population of members is created which meet all hard constraints.

2. *Fitness Evaluation.* Each member of the population is then analyzed. For the current design tool, the following analyses are performed:

- weight calculation
- crashworthiness estimation
- peak load during crash
- calculation of bending moment capacity
- calculation of torsional moment capacity
- calculation of pressure load capacity

The baseline fitness of each design is calculated using the expression:

$$fitness = f_c \frac{E}{E_{base}} + f_w \frac{w_{base} - w}{w_{base}} \tag{5.28}$$

where: f_c and f_w are user-defined weighting factors for energy absorption and weight, respectively, E is the energy absorbed by the design, w is the weight of the design, and

E_{base} and w_{base} are user-defined baseline values for energy absorption and weight. By adjusting these four parameters, the designer has a substantial amount of flexibility in rating designs. Designs can be optimized for energy absorption, weight, or any combination of these.

In addition to the "hard" constraints discussed above, a number of "soft" constraints may also be specified. These are typically referred to as penalty constraints. For penalty constraints, designed are allowed to exist which violate certain constraints, but their fitness is penalized. Thus, their fitness function is modified by:

$$fitness = fitness_{base} - \sum_i p_i \frac{X_i - X_{req}}{X_{req}} \tag{5.29}$$

where $fitness_{base}$ is the fitness computed from Eqn. 5.28 above, X_{req} is the required value of a constraint (e.g. bending moment capacity), X_i is the actual value, and p_i is a user-defined penalty parameter. Using penalty constraints allows the retention of designs which fail to meet certain constraints, but may actually be very close to good designs which do meet these constraints.

3. Ranking of Population Based on Fitness. Based on the computed fitnesses of the current generation, the members are ranked 1 through Ngen, where Ngen is the size of the population. These rankings will then be utilized in the selection process described next.

4. Selection of Parents. In order to create the following generation, members of the existing generation are selected to be reproducing parents. Rather than just randomly select two parents, a probabilistic approach is used based on the fitness ranking of the current generation. This approach ensures that the more fit members of the population are

more likely to be selected for reproduction. The roulette wheel method was selected for this purpose. Each member of the current population has a space on the roulette wheel, but the size of that space depends on that member's fitness ranking. The total area on the roulette wheel is the sum of *1* through N_{gen}, and the size of each member's space is their ranking subtracted from N_{gen}+1. This is illustrated schematically for a four-member population in Fig. 5.11. The probability that the top-ranked member will be selected is:

$$prob = \frac{N_{gen} + 1 - rank}{\sum_{1}^{N_{gen}} i} = \frac{4 + 1 - 1}{1 + 2 + 3 + 4} = 0.40 \tag{5.30}$$

Design #	Rank
1	3
2	1
3	2
4	4

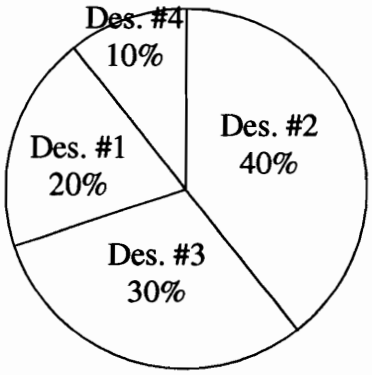

Figure 5.11 Illustration of roulette wheel approach for selection

To maintain a fluid searching of the design space, it is also required that the two parents be unique. That is, the same member of the population may not be selected to be both parents of a given offspring.

5. Reproduction. Once two parents are selected, the reproduction process is used to create a child member of the next generation. This is accomplished by using the crossover

technique. This is analogous to the means by which child DNA strings are created in nature. The methods chosen for the current tool are one-point crossover, uniform crossover, and cloning.

In the one-point crossover method, a location within the design string is selected at random. The child is created by copying one parent's string on one side of this crossover point, and the other parent's on the other side. This is illustrated schematically in Fig. 5.12. Which parent provides the string for which side of the crossover is also determined randomly.

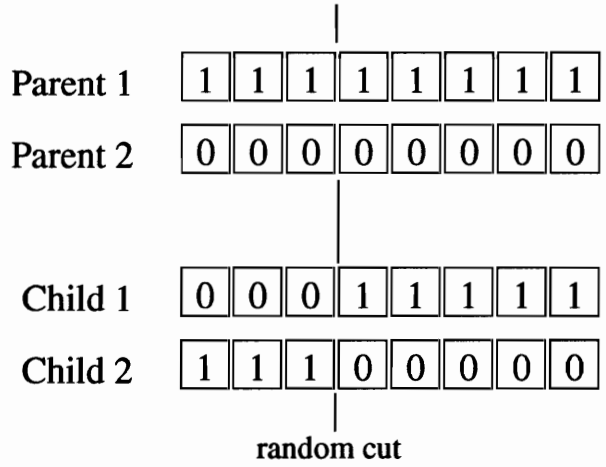

Figure 5.12 Schematic of one-point crossover [1]

In the uniform crossover method, each allele in the design string is considered independently. For each allele, the parent whose allele is copied is chosen randomly. The uniform crossover method is illustrated schematically in Fig. 5.13. Thus, it is possible to end up with a child design that is radically different than either parent. This helps to maintain a wide search of the design space.

The cloning method is not truly a crossover method, but it is commonly used in genetical algorithms. In this method, one parent is selected randomly, and the child is just a duplicate of that one parent. Cloning is illustrated schematically in Fig. 5.14.

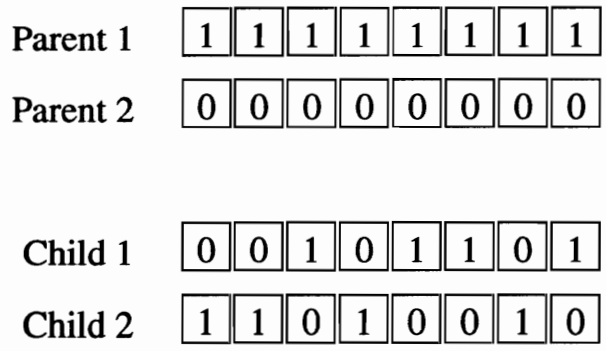

Figure 5.13 Schematic of uniform crossover

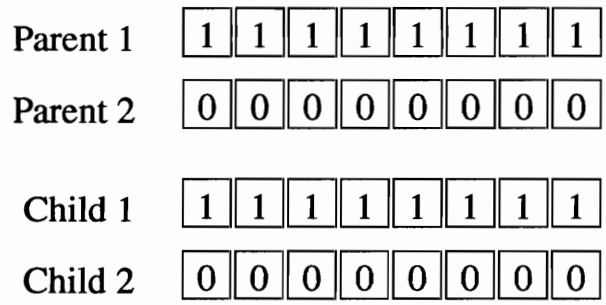

Figure 5.14 Schematic of cloning [1]

Which of these methods is used for a particular reproduction is decided randomly. However, the designer may specify percentages for each. For the current study, one-point crossover was used 50% of the time, uniform crossover was used 35% of the time, and cloning was used 15% of the time. Varying these values will not change the optimum result, but may affect the convergence rate of the genetic algorithm method.

6. Mutation. In biological systems, many changes in species result from genetic mutation. In nature, this means that a particular gene is modified, either by accident or through some other cause. This is a particularly important part of genetic algorithms, as it aids is preventing designs from converging on a local optimum. The mutation method imple-

mented in the current design tool uses a user-defined mutation factor which is operated on each gene of each child design. A random number between 0 and 1 is selected for each gene. If this number is less than or equal to the mutation factor, that gene is flipped (if it is 0 it becomes 1, and vice versa). Mutation is illustrated schematically in Fig. 5.15. Empirical results with genetic algorithms suggest that the mutation factor should be high enough that one gene per design string is mutated most of the time. So for the current study, a mutation factor of 0.04 was selected (1 divided by the number of genes in the string, 24). Mutation also does not affect the optimum design, but can affect the convergence rate.

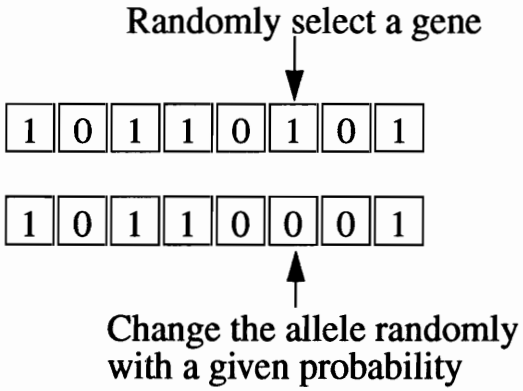

Figure 5.15 Schematic of mutation [1]

The seletion-reproduction-mutation process continues until the next generation is fully populated. If hard constraints are specified, any children which do not meet these constraints are discarded and the selection-reproduction-mutation process is repeated until a suitable child design is created.

Elitist Strategy. In order to ensure that convergence is obtained monotonically, the elitist strategy was implemented in the current project. This is a common practice in genetic algorithms, in which the best design of the current generation is copied directly into the following generation. If this were not done, it would be possible for the best design of the

new generation to have a lower fitness value than the best design of the previous generation. While this does not preclude eventual convergence to the optimum design, it generally aids in the convergence process.

6.0 Illustrative Design Example

In Chapter 5, development of the preliminary design tool was presented. In order to demonstrate the use of this tool, an illustrative example was considered. The results of the design study on this example are presented in this chapter. The purpose of the current study was not to perform a trade study on fuselage designs. This example is merely a demonstration of the use and promise of the design tool. With that in mind, in the following sections the example problem is stated, and a preliminary design process is illustrated for both an isotropic material (aluminum) and a composite material (graphite-epoxy).

6.1 Problem Statement

To best demonstrate the use of the preliminary design tool, a sample problem was selected for applying the tool to the design of a crashworthy, grid-stiffened fuselage. The problem chosen corresponded to the Boeing 757-200 large passenger transport aircraft, which is shown in Fig. 6.1. The pertinent specifications for the 757-200, courtesy of the Boeing Company[116] are shown in Table 6.1.

The goal of this example problem was to design a fuselage as light as possible yet with as much energy absorption capability as possible. The procedure and results of that process are summarized in Secs. 5.2 and 5.3. However, this optimization must be performed in the presence of the other design constraints on the fuselage, such as those discussed in Sec. 5.3. Thus, design load requirements were needed for the following quantities:

- Bending moment
- Torsional moment
- Internal pressure

Figure 6.1 The Boeing 757-200 transport aircraft [116]

Table 6.1 Specifications for Boeing 757-200 transport aircraft [116]

Wingspan	124 ft 10 in
Overall length	155 ft 3 in
Cabin width	11 ft 7 in
Fuel capacity	11,276 gallons
Engines	2 Rolls Royce RB211-535 or 2 Pratt-Whitney PW2040
Max takeoff weight	220,000 lb

• Peak load during impact

Normally, a designer would know the load requirements for the structure. However, since this information was unavailable from Boeing, estimates were made for use in this example. The rationale and results for these estimates are described below.

Bending Moment Requirement. To estimate the required bending moment capacity of the fuselage, the aircraft was idealized as a simple beam. The weight of the fuel, wings, and engines was assumed to act as a concentrated load at the center of the remaining fuselage section. The remaining structural weight was assumed to be evenly distributed along the remainder of the aircraft. This is illustrated schematically in Fig. 6.2, which also shows the resulting moment diagram of the aircraft (simple beam).

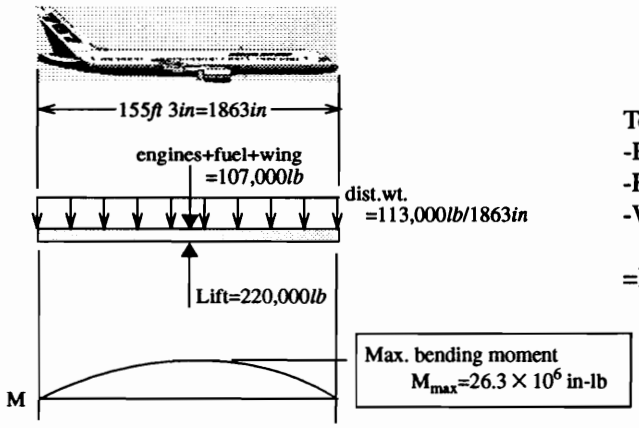

Weight Estimates	
Total weight	220,000 lb
-Engine weight	≈10,000 lb
-Fuel weight	≈75,000 lb
-Wing weight	≈22,000 lb
=Distributed weight	≈113,000 lb

Figure 6.2 Calculation of required bending moment capability

Torsional Moment Requirement. To estimate the maximum torsional moment requirement, it was assumed that the aerodynamic resultant of the lift on the wings is located one-third of the way from the aircraft centerline to the wing tip. Under level flight conditions, the lift on each wing is the same and there is no torsional moment on the fuselage. When the aircraft banks (rolls to one side) during a maneuver, the lift on the two wings is no

longer equal, and the torsional inertia of the fuselage results in a torsional moment. To represent this, it was assumed that 75 percent of the lift was being carried by one wing during a maneuver, while the remaining 25 percent was being carried by the other. Rather than calculating the rotational inertia effects, it was assumed that the nose of the aircraft was fixed. Thus, the torsional moment was calculated from the moment resultant of the two lift forces. This is illustrated in Fig. 6.3.

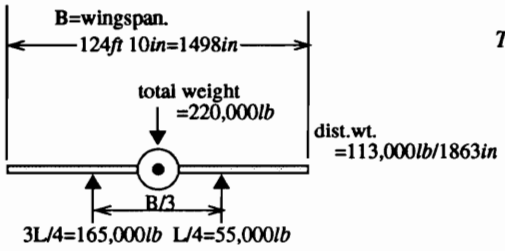

$$T_{max} = (\frac{3}{4}L)(\frac{B}{6}) - (\frac{1}{4}L)(\frac{B}{6}) = 27.5 \times 10^6 in \cdot lb$$

Max. torsional moment
T_{max}=27.5 × 10^6 in-lb

Figure 6.3 Calculation of required torsional moment capability

Internal Pressure Requirement. Aircraft cabins require internal pressure when the aircraft is flying at the high altitudes typical of most modern transports. Typically, this pressure is approximately equivalent to atmospheric pressure on the ground, or roughly 15 pounds per square inch. Allowing for a slight overpressure, the internal pressure requirement was assumed to be 20 pounds per square inch (*psi*).

Peak Load Requirement. The peak load requirement derives from the fact that decelerations during impact must be maintained below the fatal level for the human passengers. The danger level for humans is a deceleration of about 10*g*, or 10 times the acceleration of gravity. Applying this factor to the fuselage would be somewhat misleading. A substantial amount of the impact force would be absorbed by the landing gear or the fuselage bulk-

heads. It was estimated for the current example that the fuselage itself should be designed such that it would generate a force that would cause no greater than $2.5g$ deceleration. Thus, the maximum allowable peak load (per unit length of fuselage) was obtained from:

$$\frac{F}{L} = \frac{ma}{L} = \frac{m(2.5g)}{L} = \frac{(220,000lb)\,2.5}{1863in} = 295lb/in \tag{6.1}$$

6.2 Design of Aluminum Isogrid-Type Fuselage

The analysis methods incorporated into the preliminary design tool are capable of analyzing advanced composite materials. However, it is always advisable to test composite models using isotropic material properties first. For this reason, a design study was performed with the assumption that the fuselage skin and stiffeners were manufactured from standard aluminum. The properties used for aluminum are summarized in Table 6.2 below.

Table 6.2 Mechanical properties of aluminum used in design study

Elastic modulus, E	10 Msi
Shear modulus, G	3.85 Msi
Poisson's ratio, ν	0.3
Tensile strength, σ_{ult}	50 ksi
Shear strength, τ_{ult}	25 ksi

It is important to point out that, although the aluminum properties were used in the design tool, the results should be viewed with some skepticism. One assumption inherent in the progressive failure model was that failure events were brittle and resulted in total loss of load-carrying capability of the failed region. In aluminum, as in other ductile met-

als, many of these failure events would occur in conjunction with significant plastic yielding which would result in additional residual stiffness and increased energy absorption. Comparing the results from this aluminum design study with the results for the composite fuselage in the following section would not be advisable.

Two important aspects of the design study are worth mentioning here. They are:

-Only isogrid-type stiffener configuration was investigated. Although the design tool was designed with the capability to consider orthogrid, spiral grid, and general grid, only the isogrid-type stiffener configuration was considered in the example problem. However, since the rib angle is one of the design variables, this does not limit the problem to true isogrids, which involve equilateral triangular stiffener sections.

-The moment requirements were implemented as hard constraints. It was found to be very difficult to adjust the penalty constraint parameters in a manner that yielded meaningful crashworthy designs. This fact seemed to only slightly increase the convergence time.

The design process was accomplished in two steps. These were:

1. Minimum weight design of fuselage without crashworthiness consideration.
2. Maximum crashworthiness design with weight constraint.

These steps, and their results, are discussed in the sections below.

6.2.1 Minimum Weight Design of Fuselage Without Crashworthiness Consideration

The first step in the design study was to optimize the fuselage for minimum weight without considering crashworthiness. This represents the traditional preliminary design process. This was accomplished by setting the crashworthiness fitness coefficient to zero and eliminating the peak load requirement. The design code was written so that when the

crashworthiness effects were not considered, it does not perform the progressive failure analysis on each design. This greatly enhanced the execution speed of the program. It was possible to analyze 500 generations of a 25-member population using the genetic algorithm in less than 1 minute of run time on a desktop Pentium Pro 200 computer. This analysis was performed 10 times, each time resulting in the same optimum (minimum weight) design. The resulting design is shown in Table 6.3, along with its resulting load-carrying capabilities. The energy absorption and peak load for this design are also shown for comparative purposes with the results described in the following section.

Table 6.3 Parameters of aluminum isogrid-type minimum weight design

Rib thickness, t_r	in	0.08
Rib height, h_r	in	1.05
Skin thickness, t_s	in	0.02
Rib angle, ϕ	deg	70
Number of cells, N_c	----	8
Weight parameter (volume per unit length)	in^2	5.76
Energy absorbed (per unit length)	in-lb/in	139.3
Bending moment capacity	in-lb	27.2×10^6
Torsional moment capacity	in-lb	31.4×10^6
Pressure load capacity	psi	20.6
Peak impact load (per unit length)	lb/in	8.4

6.2.2 Maximum Crashworthiness Design with Weight Constraint

The result of the minimum weight design ignoring crashworthiness clearly demonstrates the lowest possible weight design which meets all the design requirements. Any design which increases crashworthiness must invariably be a heavier design. Thus, the approach for the second part of the design process was to implement weight as a constraint

(rather than as a fitness parameter) and ask the design tool to select the maximum energy absorbing design within this constraint. The weight constraint was arbitrarily selected to be about one-third greater than the minimum-design value, or:

$$wpl_{max} = 7.5 \tag{6.2}$$

where *wpl* is the weight parameter per unit length of fuselage.

With the crashworthiness effects included, the progressive failure analysis consumed much of the computational time of the design tool. Thus, the number of cases that could be run, as well as the size of population and number of generation, had to be significantly reduced. It was found that 100 generations of a 15-member population could be executed in about 8 hours on the same desktop Pentium Pro 200 computer. Six optimization runs were executed for this design. The designs obtained from these runs are summarized in Table 6.4. The optimum design was achieved in 4 of the 6 runs. Although there is no assurance that this design is in fact the true global optimum, a parameter study of the design space in the vicinity of this design showed that it was at least a local optimum.

To get additional insight into the optimum nature of the selected designs, a parameter study was performed by first noting that the minimum-weight design shown in Table 6.3 and the most crashworthy design from Table 6.4 both have the same rib dimensions and skin thickness. The only variables that changed were the grid angle and number of cells. To investigate the design space, holding the rib and skin dimensions constant, the progressive failure model was exercised over the full range of allowable rib angles (20-150 degrees) and number of cells (8-32). The resulting contours of energy absorption and weight parameter are shown in Fig. 6.4. Note in this figure that the region in the upper left has been eliminated and represents designs which do not meet the moment requirements.

Table 6.4 Optimum crashworthiness designs obtained for aluminum isogrid-type fuselage

		Design 1 (4 runs)	Design 2 (2 runs)
Rib thickness, t_r	in	0.08	0.08
Rib height, h_r	in	1.05	1.05
Skin thickness, t_s	in	0.02	0.02
Rib angle, ϕ	deg	50	55
Number of cells, N_c	----	9	10
Weight parameter (volume per unit length)	in^2	7.16	7.39
Energy absorbed (per unit length)	in-lb/in	236.6	227.0
Bending moment capacity	in-lb	31.1×10^6	31.5×10^6
Torsional moment capacity	in-lb	31.6×10^6	34.6×10^6
Pressure load capacity	psi	23.4	23.7
Peak impact load (per unit length)	lb/in	14.9	14.1

It is clear from this plot that, at least with these rib and skin dimensions, the minimum weight design occurs when ϕ=70° and N_c=8 as was found using the genetic algorithm. If the weight parameter is allowed to increase to 7.5, it is apparent from this plot that the rib angle should go down.

The region around that area is magnified and shown in Fig. 6.5. The two designs selected by the genetic algorithm are denoted on this plot. It is obvious from this plot that the better of those designs (ϕ=50°, N_c=9) is the optimum design possible given these rib and skin dimensions and limiting designs to integer values of N_c (which is necessary to use the global-local model). Although it is possible that a design with different rib and skin dimensions could be found that is superior to the design found by the genetic algorithm, this design is clearly an optimum within the current rib and skin dimensions. This increases the confidence that the selected design may indeed be a global optimum.

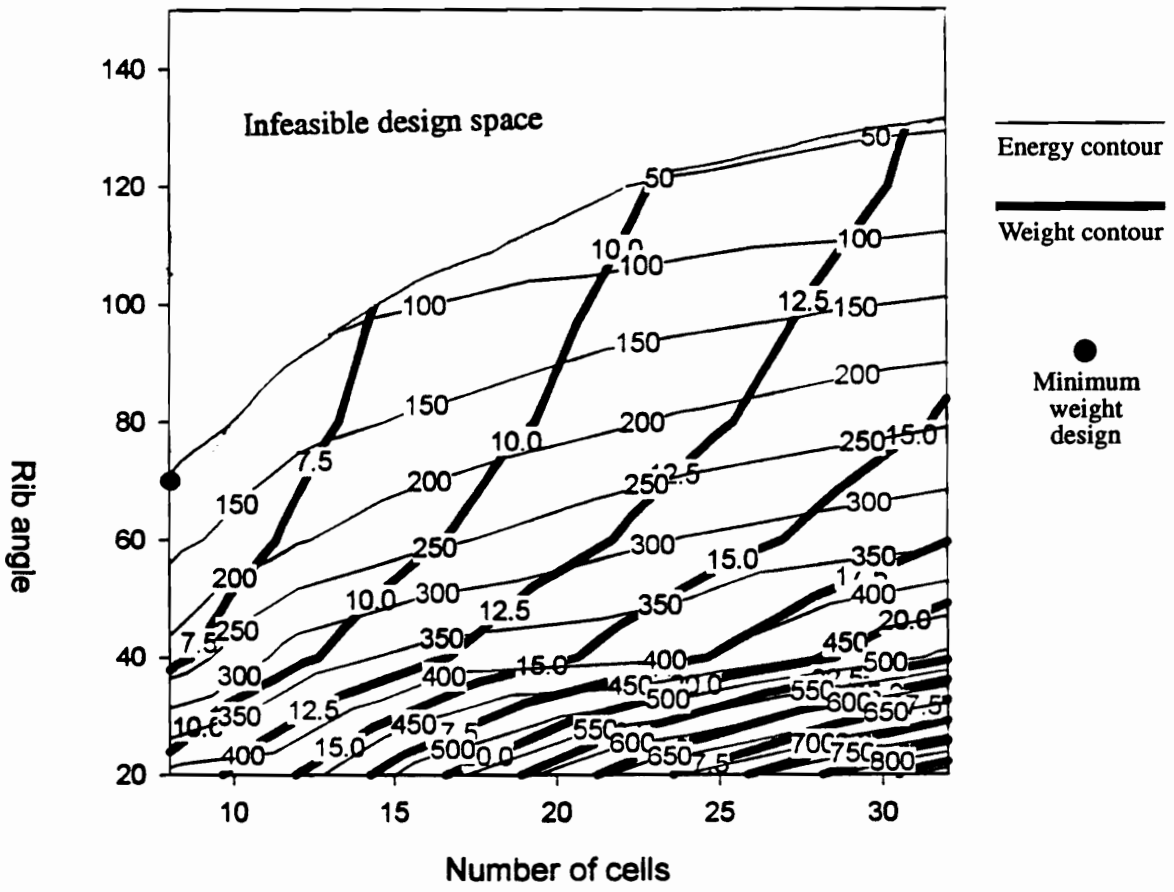

Figure 6.4 Energy and weight parameter contours over full range of grid spacing and grid angles for aluminum isogrid-type fuselage

6.2.3 Comparison of Minimum Weight and Maximum Crashworthiness Designs

The optimum designs obtained using the minimum weight and maximum crashworthiness approaches described above are summarized and compared in Table 6.5. The significance of these results is that the preliminary design tool was successful in locating a design which increased energy absorption capability by 70 percent over the minimum weight design at a weight penalty of only 24 percent.

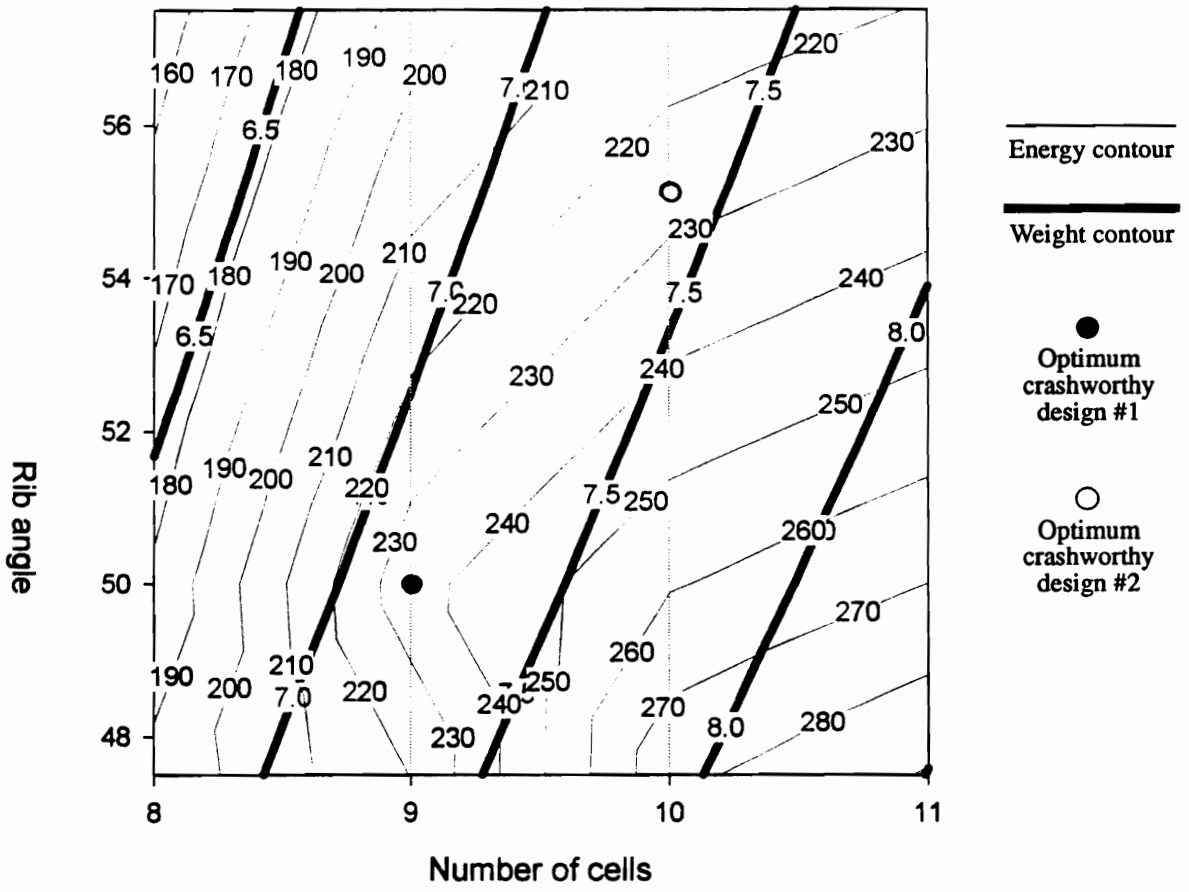

Figure 6.5 Energy and weight parameter contours near optimum region of grid spacing and grid angles for aluminum isogrid-type fuselage

The predicted progressive failure responses for the minimum weight and optimum fuselage designs are shown in Fig. 6.6.

Table 6.5 Comparison of minimum weight and optimum crashworthiness designs for aluminum isogrid-type fuselage

		Mininum weight design	Optimum crashworthiness design
Rib thickness, t_r	in	0.08	0.08
Rib height, h_r	in	1.05	1.05
Skin thickness, t_s	in	0.02	0.02
Rib angle, ϕ	deg	70	50
Number of cells, N_c	----	8	9
Weight parameter (volume per unit length)	in^2	**5.76**	**7.16**
Energy absorbed (per unit length)	in-lb/in	**139.3**	**236.6**
Bending moment capacity	in-lb	27.2×10^6	31.1×10^6
Torsional moment capacity	in-lb	31.4×10^6	31.6×10^6
Pressure load capacity	psi	20.6	23.4
Peak impact load (per unit length)	lb/in	8.4	14.9

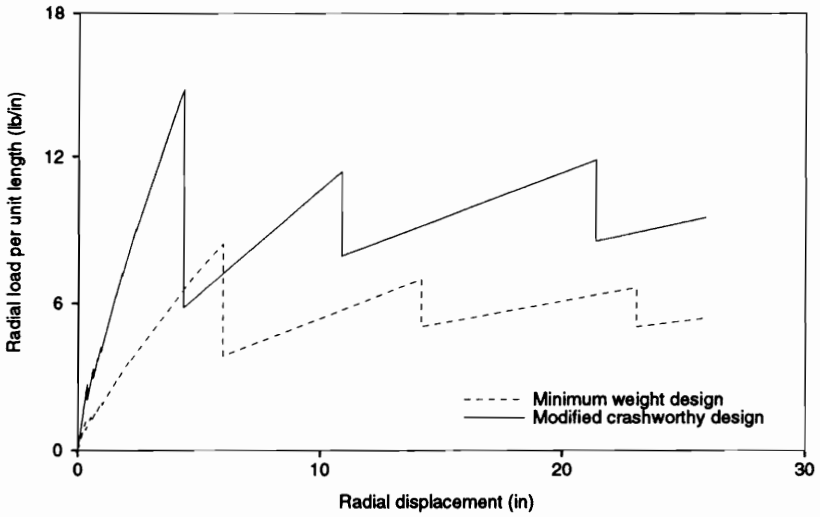

Figure 6.6 Comparison of progressive failure responses of minimum weight and optimum crashworthiness design for aluminum isogrid-type fuselage

6.3 Design of Graphite-Epoxy Isogrid-Type Fuselage

Having demonstrated the use of the preliminary design tool for isotropic aluminum, the next step was to apply it to the brittle, fiber-reinforced materials for which it was intended. For this purpose, a design study was performed with the assumption that the fuselage skin and stiffeners were manufactured from graphite-epoxy. The properties used for graphite-epoxy are typical and are summarized in Table 6.6 below. The fuselage skin was assumed to be made of a quasi-isotropic layup, while the ribs were assumed to be orthotropic, with the fibers aligned with the rib directions.

Table 6.6 Mechanical properties of graphite-epoxy used in design study

Longitudinal elastic modulus, E_1	18.5 Msi
Transverse elastic modulus, E_2	1.64 Msi
Shear modulus, G_{12}	0.87 Msi
Poisson's ratio, ν_{12}	0.3
Longitudinal tensile strength, $(\sigma_1)_{ult}$	165 ksi
Transverse tensile strength, $(\sigma_2)_{ult}$	9 ksi
Quasi-isotropic tensile strength, $(\sigma_{iso})_{ult}$	82 ksi

As was the case in the aluminum design case, only isogrid-type stiffener configurations were investigated, and the moment requirements were implemented as hard constraints. The design process was accomplished using the same steps as were taken in the aluminum design case.

6.3.1 Minimum Weight Design of Fuselage Without Crashworthiness Consideration

The first step in the design study was to optimize the fuselage for minimum weight without considering crashworthiness. This was accomplished by setting the crashworthi-

ness fitness coefficient to zero, and eliminating the peak load requirement. As in the aluminum case, this analysis was performed 10 times, each time resulting in the same optimum (minimum weight) design. The resulting design is shown in Table 6.7, along with its resulting load-carrying capabilities. The energy absorption and peak load for this design are also shown for comparative purposes with the results described in the following section.

Table 6.7 Parameters of graphite-epoxy isogrid-type minimum weight design

Rib thickness, t_r	in	0.11
Rib height, h_r	in	0.675
Skin thickness, t_s	in	0.02
Rib angle, ϕ	deg	65
Number of cells, N_c	----	8
Weight parameter (volume per unit length)	in^2	5.47
Energy absorbed (per unit length)	in-lb/in	143.6
Bending moment capacity	in-lb	27.3×10^6
Torsional moment capacity	in-lb	105.1×10^6
Pressure load capacity	psi	37.6
Peak impact load (per unit length)	lb/in	11.6

6.3.2 Maximum Crashworthiness Design with Weight Constraint

The result of the minimum weight design ignoring crashworthiness demonstrates the lowest possible weight design which meets all the design requirements. Any design which increases crashworthiness must invariably be a heavier design. Thus, the approach for the second part of the design process was to implement weight as a constraint (rather than as a fitness parameter) and ask the design tool to select the maximum energy absorbing design within this constraint. The weight constraint was arbitrarily selected to be about one-third

greater than the minimum-design value, or:

$$wpl_{max} = 7.5 \tag{6.3}$$

Six optimization runs were executed for this design. The designs obtained from these runs are summarized in Table 6.8. The optimum design was achieved in 4 of the 6 runs. Although again, there is no assurance that this design is in fact the true global optimum, a parameter study of the design space in the vicinity of this design showed that it was at least a local optimum.

Table 6.8 Optimum crashworthiness designs obtained for graphite-epoxy isogrid-type fuselage

		Design 1 (4 runs)	Design 2 (2 runs)
Rib thickness, t_r	in	0.11	0.11
Rib height, h_r	in	0.80	0.675
Skin thickness, t_s	in	0.02	0.02
Rib angle, ϕ	deg	45	35
Number of cells, N_c	----	8	8
Weight parameter (volume per unit length)	in^2	7.16	7.21
Energy absorbed (per unit length)	in-lb/in	333.1	315.9
Bending moment capacity	in-lb	29.3×10^6	27.1×10^6
Torsional moment capacity	in-lb	31.2×10^6	36.1×10^6
Pressure load capacity	psi	47.2	45.3
Peak impact load (per unit length)	lb/in	29.3	27.1

To gain additional insight into the optimum nature of the selected designs, a parameter study was performed. First, it was noted that the minimum-weight design shown in Table 6.7 and the crashworthy designs from Table 6.8 all have the same rib and skin thicknesses. The only variables that changed were the grid angle and rib height.

To investigate the design space, holding the thicknesses constant, the progressive failure model was exercised over the full range of allowable rib angles (20-150 degrees) and number of cells (8-32). The resulting contours of energy absorption and weight parameter are shown for a rib height of 0.675 inches in Fig. 6.7 and for a rib height of 0.80 inches in Fig. 6.8. The minimum weight design from Table 5.7 is denoted and is clearly the optimum design for these rib and skin dimensions. If the weight parameter is permitted to increase to 7.5, it is apparent from this plot that the rib angle should decrease.

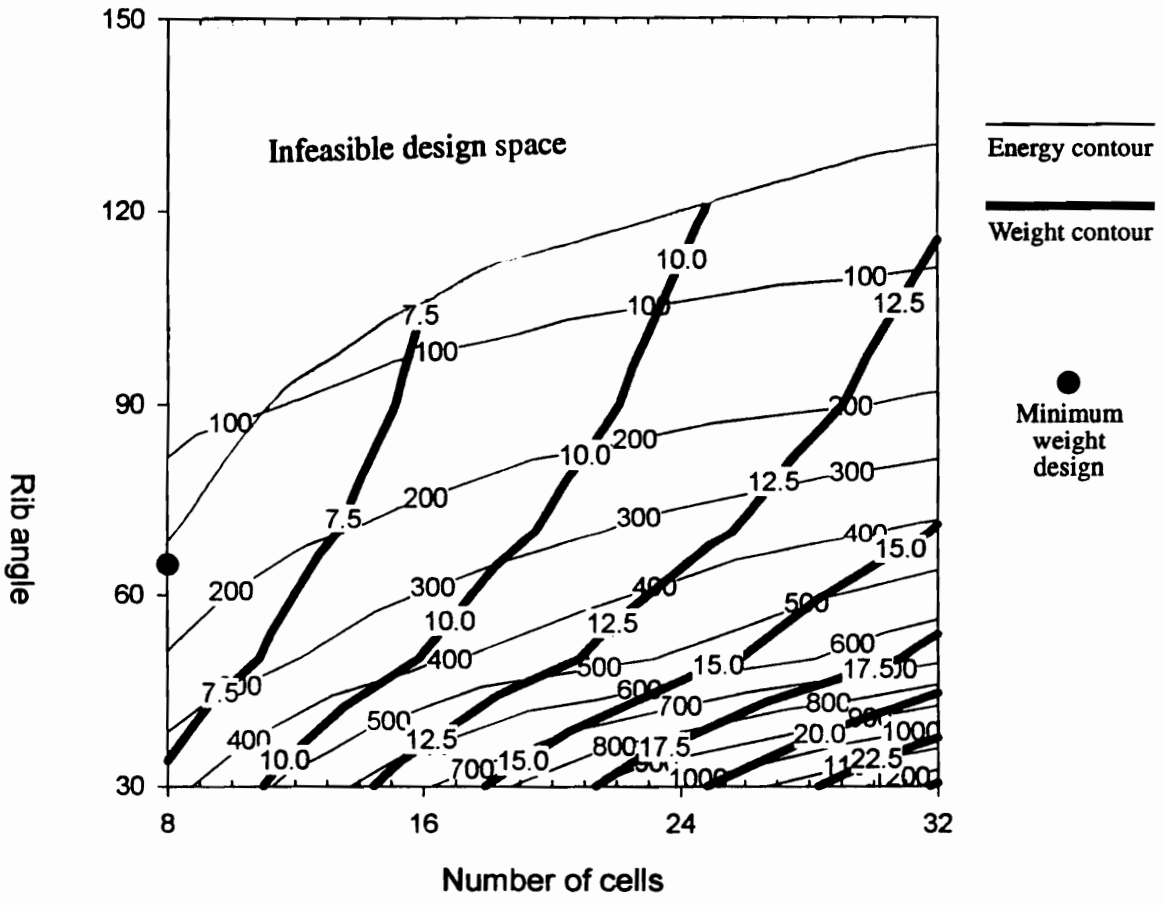

Figure 6.7 Energy and weight parameter contours over full range of grid spacing and grid angles for graphite-epoxy isogrid-type fuselage (rib height=0.675 in)

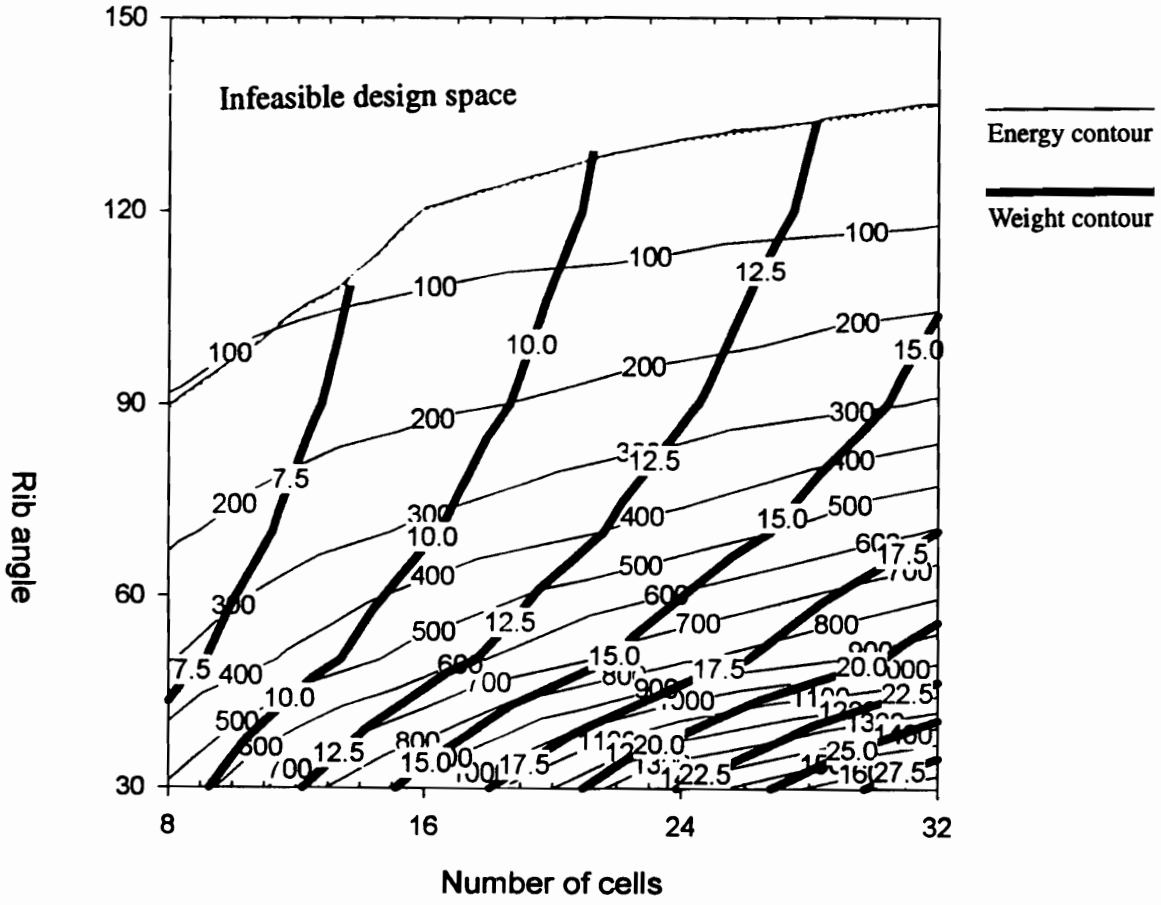

Figure 6.8 Energy and weight parameter contours over full range of grid spacing and grid angles for graphite-epoxy isogrid-type fuselage (rib height=0.80 in)

To help visualize this region better, that area is magnified in the vicinity of the optimum design. The resulting contours of energy absorption and weight parameter are shown for a rib height of 0.675 inches in Fig. 6.9 and for a rib height of 0.80 inches in Fig. 6.10. The optimum crashworthiness designs selected by the genetic algorithm are also shown. It is apparent from this plot that the design (ϕ=45°, N_c=8, h_r=0.80 *in*) is the optimum design possible given these rib and skin thicknesses. Although it is possible that a design with different rib or skin thicknesses and number of cells could be found that is superior to the

design found by the genetic algorithm, this design is clearly an optimum within the current parameters. This increases the confidence that the selected design may indeed be a global optimum.

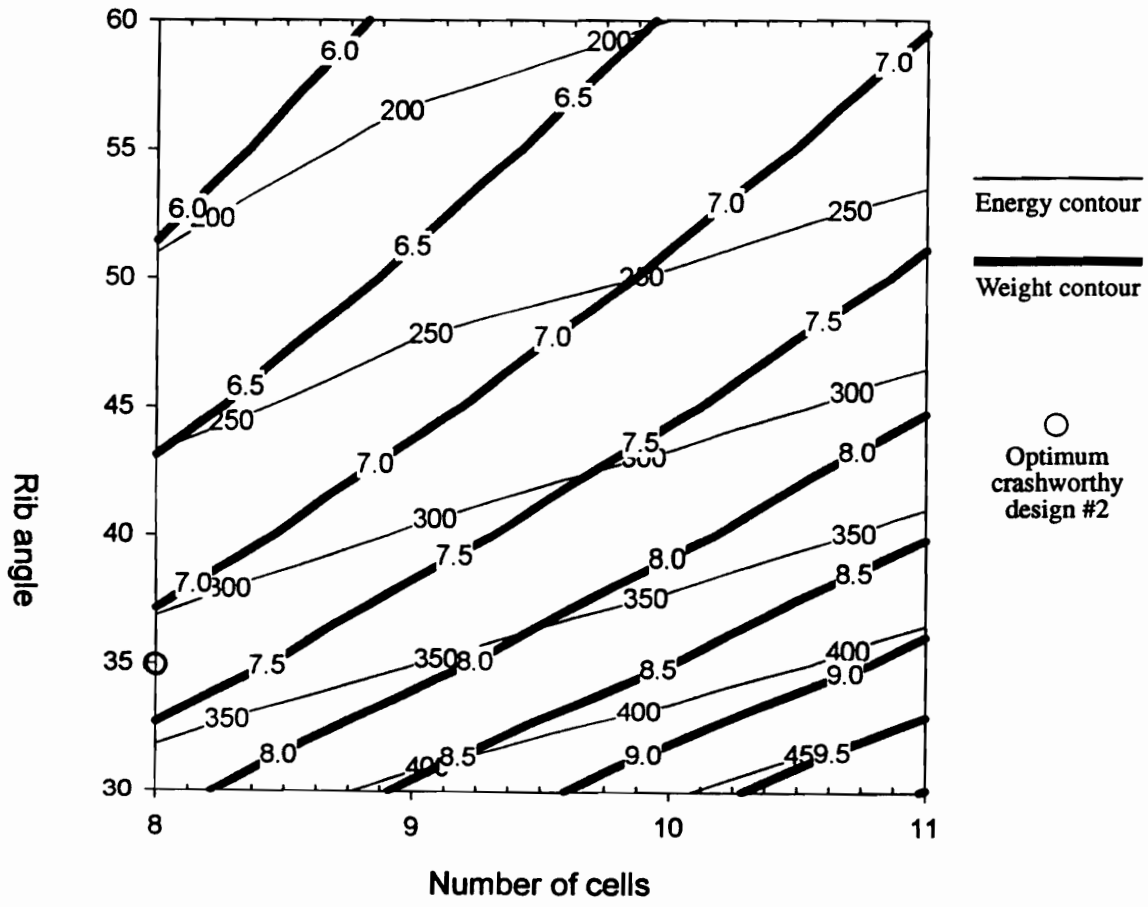

Figure 6.9 Energy and weight parameter contours near optimum region of grid spacing and grid angles for graphite-epoxy isogrid-type fuselage (rib height=0.675 in)

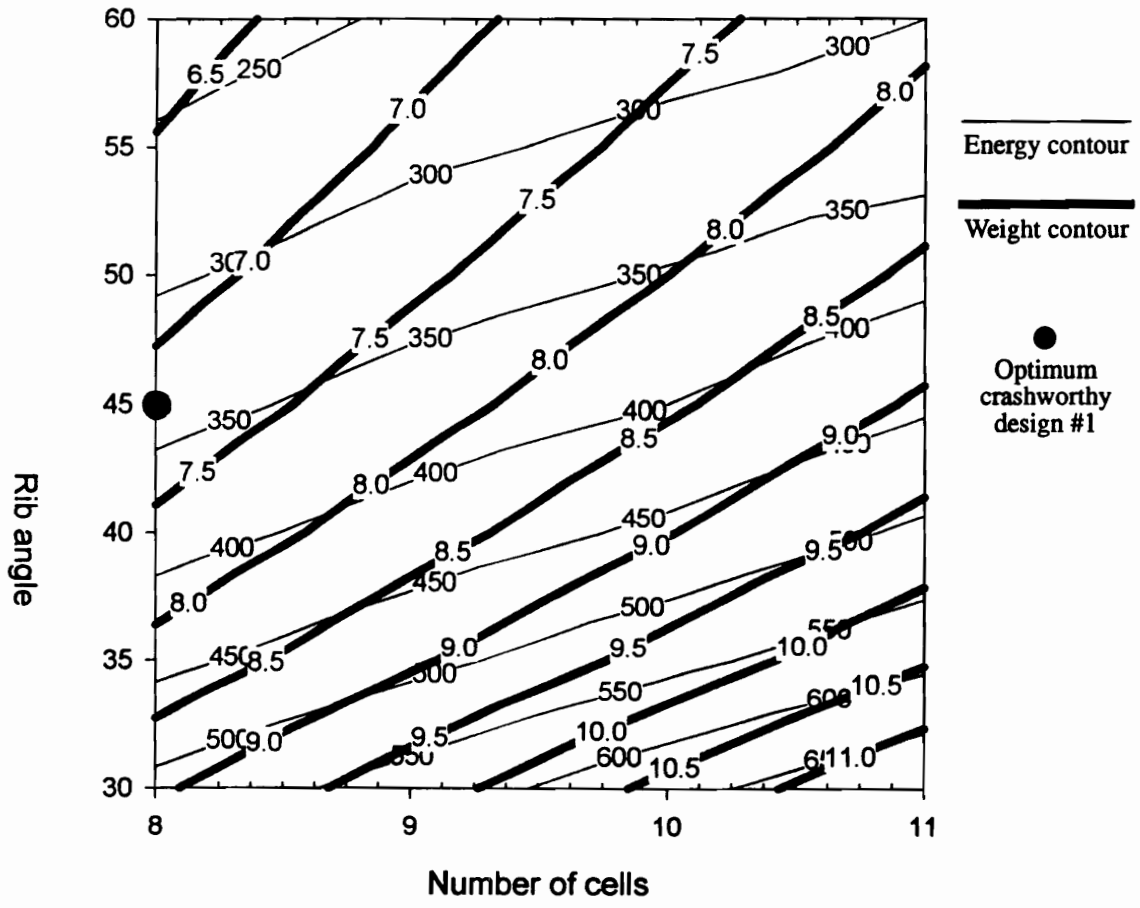

Figure 6.10 Energy and weight parameter contours near optimum region of grid spacing and grid angles for graphite-epoxy isogrid-type fuselage (rib height=0.80 in)

6.3.3 Comparison of Minimum Weight and Maximum Crashworthiness Designs

The optimum designs obtained using the minimum weight and maximum crashworthiness approaches described above are summarized and compared in Table 6.9. The significance of these results is that the preliminary design tool was successful in locating a design which increased energy absorption capability by 318 percent (more than a factor of 4) over the minimum weight design at a weight penalty of only 35 percent.

Table 6.9 Comparison of minimum weight and optimum crashworthiness designs for graphite-epoxy isogrid-type fuselage

		Mininum weight design	Optimum crashworthiness design
Rib thickness, t_r	in	0.11	0.11
Rib height, h_r	in	0.675	0.80
Skin thickness, t_s	in	0.02	0.02
Rib angle, ϕ	deg	65	45
Number of cells, N_c	----	8	8
Weight parameter (volume per unit length)	in^2	**5.47**	**7.16**
Energy absorbed (per unit length)	in-lb/in	**143.6**	**333.1**
Bending moment capacity	in-lb	27.3×10^6	29.3×10^6
Torsional moment capacity	in-lb	105.1×10^6	106.0×10^6
Pressure load capacity	psi	37.6	47.2
Peak impact load (per unit length)	lb/in	11.6	29.3

The predicted progressive failure responses for the minimum weight and optimum crashworthiness designs are shown in Fig. 6.11

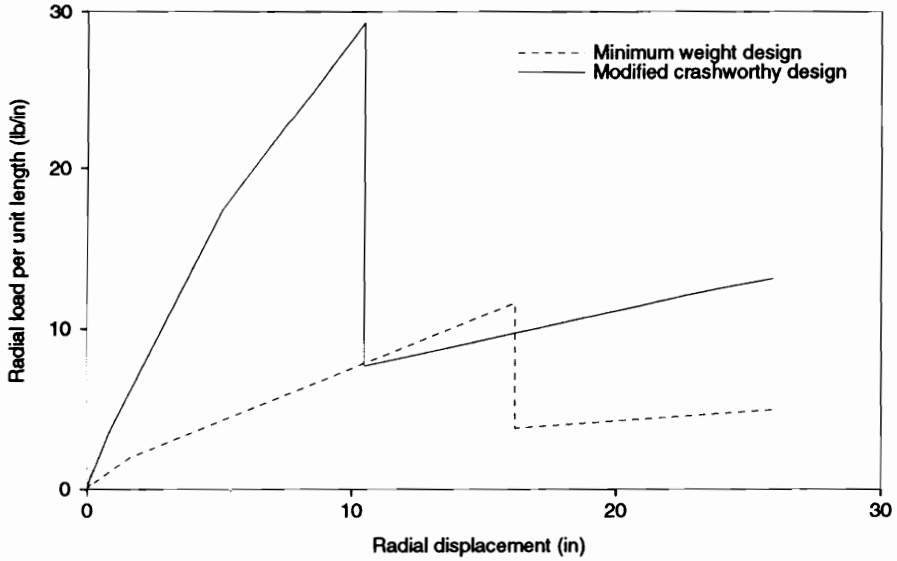

Figure 6.11 Comparison of progressive failure responses of minimum weight and optimum crashworthiness design for graphite-epoxy isogrid-type fuselage

7.0 Conclusions and Recommendations

In this study, a perceived need for a preliminary design tool for incorporating crashworthiness into the preliminary design of grid-stiffened composite fuselage structures was identified. This preliminary design tool was then developed, utilizing a global-local method to simplify the simulation of crash response and estimation of crashworthiness, along with a genetic algorithm to search for optimum designs. This tool was then demonstrated using an illustrative example, which showed the ability of the tool to improve crashworthiness during the preliminary design stage.

The major accomplishments of the present effort are summarized below:

- A global-local analysis approach was developed to reduce the computational requirements of analyzing a fuselage undergoing a crash event. The method served as the bridge between a local model based on layered plate finite elements and a global model based on simple beam-type elements. A reduction method was developed to derive a beam-type stiffness matrix from a complex local model, and a stress recovery procedure was developed to calculate local stresses from the global model results. The global-local procedure was validated for some simple examples, showing excellent agreement with a full finite element analysis.
- A progressive failure model was implemented with the global-local analysis to enable modeling of the impact event during which regions of the structure fail at various intervals. Simple local failure models were derived or taken from the literature and incorporated into the failure model.
- An approximate approach to incorporate effects of geometric nonlinearity was developed and incorporated. The large predicted deflections necessitated this effort.
- The global-local model with progressive failure capability was implemented to analyze

the crash response of a fuselage. The results of this analysis were used to estimate crashworthiness of a structure by using the integral of the force-displacement relationship as a measure of energy absorption.

- The crashworthiness estimation procedure was implemented within a genetic algorithm optimization procedure. Several simple models were developed or applied to calculate the ability of a fuselage design to withstand the non-crashworthiness related load requirements. This simple models were used along with the crashworthiness estimation and weight estimate to form the basis of the preliminary design tool.
- The preliminary design tool was used to solve an example fuselage problem that corresponded to that of the Boeing 757-200 transport aircraft. A design study was performed for an aluminum isogrid-type fuselage as well as a graphite-epoxy isogrid-type fuselage. For both materials, the tool was successful in selecting designs which substantially improved crashworthiness without a significant weight penalty on the structure.

As is the case for any research effort, there are a number of areas in which the current project could be improved or extended. The emphasis in this work was on the development and demonstration of the preliminary design tool. It was felt that once this tool was developed, if it were sufficiently modular in nature, it could be enhanced easily in a variety of ways. Some recommendations for future researchers are:

- More accurately incorporate geometric nonlinearity. While the present approximate approach improves the estimate of energy absorption, it is based on assumptions regarding the failure sequence that must eventually break down. Some means for more accurate handling of large deflections without a significant increase in computation demands would be helpful.

- Numerical methods for reducing computational times should be pursued. Although the crashworthiness estimation procedure is fairly efficient, a large number of analyses are required for optimization. It is possible that a more efficient static condensation or recovery algorithm could be derived that would lower the run time.
- A more accurate method for incorporating the effects of failed regions on the subsequent structural behavior would be useful. The current method assumes all stiffness is lost for a failed region. However, depending on the failure mode, a failed regions may still be capable of carrying increased load.
- More refined models could be implemented for the other design requirements of a fuselage. These models are implemented as subroutines, so this could be accomplished without substantially rewriting the design tool.
- Some experimental validation of the progressive failure model would increase the confidence of a designer utilizing this tool. Although the model was validated for initial linear behavior, there is no assurance of its accuracy after the failure sequence has begun. (Fortunately, high levels of accuracy are not necessarily required in the preliminary design phase).
- Thorough design studies can be performed utilizing this tool. The present effort was not intended to be an exhaustive study of the effects of various design variables on crashworthiness. However, with the tool now in hand, an investigator could learn much about the crashworthiness trends in a variety of design families.

References

1. Woodson, M.B., "Optimal Design of Composite Fuselage Frames for Crashworthiness," Ph.D. Disseratation, Virginia Polytechnic Institute and State University, Dec. 1994.

2. Carper, C.H. and Burrows, L.T., "Evolving Crashworthiness Design Criteria," *Energy Absorption of Aircraft Structures as an Aspect of Crashworthiness*, AGARD Conf. Proc. No. 443, Luxembourg, 1988, pp. 3-1 to 3-8.

3. Wittlin, G., "Aircraft Crash Dynamics: Modelling, Verification and Application," *Structural Crashworthiness*, Butterworths, London, 1983, pp. 259-282.

4. Carden, H.D., Boitnott, R.L. and Fasanella, E.L., "Behavior of Composite/Metal Aircraft Structural Elements and Components Under Crash-Type Loads--What Are They Telling Us?," presented at the 17th Congress of the International Council of Aeronautical Sciences, Stockholm, Sept. 1990.

5. Reddy, A.D., Valisetty, R.R., and Rehfield, L.W., "Continuous Filament Wound Composite Concepts for Aircraft Fuselage Structures," *Journal of Aircraft*, Vol. 22, No. 3, March 1985, pp. 249-255.

6. Meyer, R.R. and Bellingante, R.J., "Fabrication and Experimental Evaluation of Common Domes Having Waffle-Like Stiffening," Report Sm-47742, McDonnell Douglas Astronautics Co., Huntington Beach, CA, Nov. 1964.

7. Rehfield, L.W., Deo, R.B. and Renieri, G.D., "Continuous Filament Advanced Composite Isogrid: A Promising Structural Concept," *Fibrous Composites in Structural Design*, 1980, pp. 215-239.

8. Rehfield, L.W. and Reddy, A.D., "Damage Tolerance of Continuous Filament Composite Isogrid Structures: A Preliminary Assessment," *Composite Materials; Mechanics, Mechanical Properties and Fabrication*, Proceedings of Japan-U.S. Conference, Tokyo, 1981, pp. 471-477.

9. Hofmeister, L.D. and Felton, L.P., "Waffle Plates with Multiple Rib Sizes: I. Stability Analysis," *Journal of Spacecraft*, Vol. 7, No. 11, Nov. 1970, pp. 1322-1327.

10. Hofmeister, L.D. and Felton, L.P., "Waffle Plates with Multiple Rib Sizes: II. Design Examples," *Journal of Spacecraft*, Vol. 7, No. 11, Nov. 1970, pp. 1327-1331.

11. Pappas, M. and Amba-Rao, C.L., "Structural Synthesis of Thin, Cylindrical Shells with Spiral-Type Stiffeners," *AIAA Journal*, Vol. 8, No. 8, Aug. 1970, pp. 1529-1530.

12. Haftka, R.T. and Sobieski, J., "The Case for Helping Consumers of Research," *Structural Optimization*, Vol. 4, 1992, pp. 63-64.

13. Pifko, A.B., Winter, R. and Ogilvie, P.L., "DYCAST--A Finite Element Program for the Crash Analysis of Structures," *NASA CR 4040*, 1987.

14. Hallquist, J.O. and Benson, D.J., "DYNA3D, A Computer Code for Crashworthiness Engineering," *Report UCRL-95152*, University of California, Lawrence Livermore National Laboratory, Livermore, CA, Sept. 1986.

15. Jarzab, W., "Mathematical Modeling and Applications in Crash Analysis," *Proceedings of the International Conference of Supercomputer Applications in the Automotive Industry*, Zurich, 1986.

16. Gamon, M., "General Aviation Airplane Structural Crashworthiness User's Manual: Volume I, Program KRASH Theory," Final Report FAA-RD-77-189, Feb. 1978.

17. Murray, N.W., "The Static Approach to Collapse and Energy Dissipation in Some Thin-Walled Steel Structures," *Structural Crashworthiness*, Butterworths, London, 1983, pp. 44-65.

18. Winter, R., Pifko, A.B. and Cronkhite, J.D., "Crash Simulation of Composite and Aluminum Helicopter Fuselages Using a Finite Element Program," *Journal of Aircraft*, Vol. 17, No. 8, Aug. 1980, pp. 591-597.

19. Jackson, K.E., Kellas, S., Kindervater, C. and Lutzenburger, M., "Experimental and Simulated Crash Respones of Composite Airframe Structures," *Proceedings of the AHS 50th Annual Forum*, Washington, D.C., 1994, pp. 509-519.

20. Hayduk, R.J., Winter, R., Pifko, A.B. and Fasanella, E.L., "Application of the Non-Linear Finite Element Computer Program 'DYCAST' to Aircraft Crash Analysis," *Structural Crashworthiness*, Butterworths, London, 1983, pp. 283-307.

21. Haug, E., Arnaudeau, F., Dubois, J., de Rouvray, A. and Chedmail, J.F., "Static and Dynamic Finite Element Analysis of Structural Crashworthiness in the Automotive and Aerospace Industries," *Structural Crashworthiness*, Butterworths, London, 1983, pp. 175-217.

22. Tennyson, R.C. and Hansen, J.S., "Study of the Crash Behaviour of Aircraft Fuselage Structures," *Structural Crashworthiness*, Butterworths, London, 1983, pp. 218-258.

23. Logan, R.W., Burger, M.J., McMichael, L.D. and Parkinson, R.D., "Cashworthiness Analysis Using Advanced Material Models in DYNA3D," *Crashworthiness and Occupant Protection in Transportation Systems*, ASME AMD, Vol. 169, 1993, pp. 127-136.

24. Thomson, R.G. and Goetz, R.C., "NASA/FAA General Aviation Crash Dynamics Program--A Status Report," *Journal of Aircraft*, Vol. 17, No. 8, Aug. 1980, pp. 584-590.

25. Hansen, J.S. and Tennyson, R.C., "Study of the Dynamic Behaviour of Stiffened Composite Fuselage Shell Structures," *Energy Absorption of Aircraft Structures as an Aspect of Crashworthiness*, AGARD Conference Proceedings No. 443, Luxembourg, 1988, pp. 15-1 - 15-12.

26. Wittlin, G. and Caiafa, C., "Transport Airplane Crash Simulation, Validation and Application to Crash Design Criteria," *Energy Absorption of Aircraft Structures as an Aspect of Crashworthiness*, AGARD Conference Proceedings No. 443, Luxembourg, 1988, pp. 16-1 - 16-23

27. Bolukbasi, A.O., "Crash-Resistant Rotorcraft Preliminary Design Optimization," *Proceedings of the AHS 47th Annual Forum*, Phoenix, AZ, 1991,, pp. 1237-1248.

28. Toi, Y. and Yang, H.-J., "Finite Element Crush Analysis of Framed Structures," *Computers and Structures*, Vol. 41, No. 1, 1991, pp. 137-149.

29. Whitney, J.M., *Structural Analysis of Laminated Anisotropic Plates*, Technomic Publishing, Dayton, OH 1987.

30. Zhao, X., Tauchert, T.R. and Lu, W.Y., "Postbuckling Response of Elastically Supported Columns," *International Journal of Non-Linear Mechanics*, Vol. 26, No. 5, 1991, pp. 585-594.

31. Buskell, N., Davies, G.A.O. and Stevens, K.A., "Postbuckling Failure of Composite Panels," *Composite Structures 3*, ed. by I.H. Marshall, pp. 290-314.

32. Shin, D.K., Griffin, O.H. Jr. and Gürdal, Z., "Postbuckling Response of Laminated Plates Under Uniaxial Compression," *International Journal of Non-Linear Mechanics*, Vol. 28, No. 1, 1993, pp. 95-115.

33. Kweon, J.H. and Hong, C.S., "An Improved Arc-Length Method for Postbuckling Analysis of Composite Cylindrical Panels," *Computers and Structures*, Vol. 53, No. 3, 1994, pp. 541-549.

34. Jones, R.M., "Buckling of Circular Cylindrical Shells with Multiple Orthotropic Layers and Eccentric Stiffeners," *AIAA Journal*, Vol. 6, No. 12, Dec. 1968, pp. 2301-2305.

35. Soong, T-C., "Buckling of Cylindrical Shells with Eccentric Spiral-Type Stiffeners," *AIAA Journal*, Vol. 7, No. 1, Jan. 1969, pp. 65-72.

36. Steen, E., "Elastic Buckling and Postbuckling of Eccentrically Stiffened Plates," *International Journal of Solids and Structures*, Vol. 25, No. 7, 1989, pp.. 751-768.

37. Sheinman, I. and Frostig, Y., "Postbuckling Analysis of Stiffened Laminated Curved Panels," *Journal of Engineering Mechanics*, Vol. 116, No. 10, Oct. 1990, pp. 2223-2236.

38. Wu, D.L. and Zhang, Z., "Nonlinear Buckling Analysis of Discretely Stiffened Composite Cylindrical Shells," *Composite Structures*, Vol. 18, 1991, pp. 31-45.

39. Yoda, T. and Atluri, S.N., "Postbuckling Analysis of Stiffened Laminated Composite Panels, Using a Higher-Order Shear Deformation Theory," *Computational Mechanics*, Vol. 9, 1992, pp. 390-404.

40. Moradi, B. and Parsons, I.D., "Dimensional Analysis of Buckling of Stiffened Composite Shells," *Journal of Engineering Mechanics*, Vol. 118, No. 3, March 1992, pp. 557-574.

41. Sherbourne, A.N. and Bedair, O.K., "Plate-Stiffener Assemblies in Uniform Compression. Part II: Postbuckling," *Journal of Engineering Mechanics*, Vol 119, No. 10, Oct. 1993, pp. 1956-1972.

42. Boitnott, R.L., Starnes, J.H. Jr. and Johnson, E.R., "Nonlinear Response and Failure of Pressurized Composite Curved Panels," *Journal of Aerospace Engineering*, Vol. 8, No. 3, July 1995, pp. 129-138.

43. Dawe, D.J., Lam, S.S.E. and Azizian, Z.G., "Finite Strip Post-Local-Buckling Analysis of Composite Prismatic Plate Structures," *Computers and Structures*, Vol. 48, No. 6, 1993, pp. 1011-1023.

44. Loughlan, J., "A Finite Strip Analysis of the Buckling Characteristics of Some Composite Stiffened Shear Panels," *Composite Structures*, Vol. 27, 1994, pp. 283-294.

45. Scott, M.L., "Non-Linear Finite Element Modelling of an Integrally Stiffened Composite Panel," *Composite Structures*, Vol. 29, 1994, pp. 213-218.

46. Falzon, B.G and Steven, G.P., "Postbuckling Behaviour of Hat-Stiffened Thin-Skinned Carbon-Fibre Composite Panels," Proceedings of the 36th AIAA/ASME/AHS/ASC Structures, Structural Dynamics, and Materials Conference, New Orleans, LA, April 1995.

47. Renze, S.P. and Laananen, D.H., "Buckling Behavior of Bead-Stiffened Composite Panels," *Composites Science and Technology*, Vol. 50, 1994, pp. 157-166.

48. Chen, V.L., Wu, X.X. and Sun, C.T., "Prediction of Buckling Loads of Stiffened Composite Panels," *Impact and Buckling of Structures*, ASME AD Vol. 20, 1990, pp. 61-69.

49. Sandhu, J.S., "Experimental and Finite Analysis of Composite Geodetic Shells," Ph.D. Thesis, University of London, 1989.

50. Sandhu, J.S., Stevens, K.A. and Davies, G.A.O., "Torsional Buckling and Post-buckling of Composite Geodetic Cylinders with Special Reference to Joint Flexibility," *Composite Structures*, Vol. 15, 1990, pp. 301-322.

51. Parton, V.Z. and Kudryavtsev, B.A., *Engineering Mechanics of Composite Structures*, CRC Press, 1993.

52. Kalamkarov, A.L., *Composite and Reinforced Elements of Construction*, Wiley & Sons, 1992.

53. Meyer, R.R., "Buckling of 45° Eccentric-Stiffened Waffle Cylinders," *Journal of the Royal Aeronautical Society*, Vol. 71, July 1967, pp. 516-520.

54. Lee, R.-L. and Lu, S.Y., "General Instability of Inclined-Stiffened Cylinders Under Bending," *Journal of Applied Mechanics*, Sept. 1969, pp. 403-407.

55. Hayashi, T., "Buckling Strength of Cylindrical Geodesic Structures," *Composite Materials; Mechanics, Mechanical Properties and Fabrication*, Proceedings of Japan-U.S. Conference, Tokyo, 1981, pp. 428-435.

56. Rehfield, L.W., Reddy, A.D., Yehezkely, O., and Armanios, E., "Buckling of Continuous Filament Composite Isogrid Panels: Theory and Experiment," *Progress in Science and Engineering of Composites*, Proceedings of ICCM-IV, Tokyo, 1982, ed. by Hayashi, T., Kawata, K. and Umekawa, S., pp. 545-553.

57. Slysh, P., Dyer, J.E., Furman, J.H. and Key, J.E., "Isogrid Structural Tests and Stability Analyses," *Journal of Aircraft*, Vol. 13, No. 10, Oct. 1976, pp. 778-785.

58. Zhimin, Z. and Ming, F., "An Analysis of Nonlinear Post-Buckling for Laminated Composite Cylindrical Shells with Inside Triangular Isogrid Stiffeners," Proceedings of the 7th ICCM-VII, Guangshou, PRC, pp. 236-243.

59. Al-Shareedah, E.M. and Seireg, A.A., "Use of Undetermined Multipliers in the Design of Stiffened Plates," *Computers in Mechanical Engineering*, Vol. 4, No. 5, March 1986, pp. 57-64.

60. Phillips, J.L. and Gürdal, Z., "Analysis and Optimum Design of Geodesically Stiffened Composite Panels," *Composite Materials: Design and Analysis*, Proceedings of the 2nd International Conference on Computer Aided Design in Composite Material Technology, Brussels, Belgium, 1990, pp. 509-527.

61. Gendron, G., "Optimal Design of Geodesically Stiffened Composite Cylindrical Shells", Ph.D. Dissertation, Virginia Polytechnic Institute and State University, Blacksburg, VA, 1991.

62. Tsai, S.W., *Composites Design 1986*, Think Composites, Dayton, OH, 1986.

63. Chang, F.-K. and Chang, K.-Y., "A Progressive Damage Model for Laminated Composite Containing Stress Concentrations," *Journal of Composite Materials*, Vol. 21, Sept. 1987, pp. 834-855.

64. Tolson, S. and Zabaras, N., "Finite Element Analysis of Progressive Failure in Laminated Composite Plates," *Computers and Structures*, Vol. 38, No. 3, 1991, pp. 361-376.

65. Bolukbasi, A.O. and Laananen, D.H., "Prediction of Energy Absorption Capability of Composite Stiffeners," *Journal of the American Helicopter Society*, Oct. 1993, pp. 80-84.

66. Renieri, M.P. and Garrett, R.A., "Investigation of the Local Buckling, Postbuckling and Crippling Behavior of Graphite/Epoxy Short Thin-Walled Compression Members," Report MDS A7091, McDonnell Aircraft Company, St. Louis, MO, July 1981.

67. Hall, S.R., "Iterative Preliminary Design Tools for Composite Structures," *Composite Structures*, Vol. 16, 1990, pp. 103-123.

68. Hall, S.R. and Simpson, D.L., "The Development of an Iterative Advanced Composite Structural Design Capability," *Canadian Aeronatics and Space Journal*, Vol. 35, No. 2, June 1989, pp. 72-75.

69. Haftka, R.T. and Gürdal, Z., *Elements of Structural Optimization*, Kluwer Academic Publishers, 1992.

70. Bennet, J.A., Lin, K.H. and Nelson, M.F., "The Application of Optimization Techniques to Problems of Automobile Crashworthiness," *SAE Transactions*, Vol. 86, 1977, pp. 2255-2262.

71. Song, J.O., "An Optimization Method for Crashworthiness Design," Proceedings of the6th International Conference on Vehicle Structural Mechanics, Detroit, MI, 1986, pp. 39-46.

72. Sen, J.K., "Designing for a Crashworthy All-Composite Helicopter Fuselage," Proceedings of the AHS 40th Annual Forum, Arlington, VA, May 1984, pp. 56-66.

73. Kecman, D., Sadeghi, M.M. and Hardy, R.N., "Early Design Stages in the Development of Crashworthy Structures," *Crashworthiness and Occupant Protection in Transportation Systems*, ASME AMD, Vol. 169, 1993, pp. 83-96.

74. Lust, R., "Structural Optimization with Crashworthiness Constraints," *Structural Optimization*, Vol. 4, 1992, pp. 85-89.

75. Sadeghi, M.M., "Crashworthiness Design Methods Applicable at Concept Stage," *Energy Absorption of Aircraft Structures as an Aspect of Crashworthiness*, AGARD Conference Proceedings No. 443, Luxembourg, 1988, pp. 4-1 - 4-21.

76. Smith, R.A., "Crashworthiness Moves from Art to Science," *Railway Gazette International*, April 1995, pp. 227-230.

77. Butler, R., Tyler, A.A. and Cao, W., "Optimum Design and Evaluation of Stiffened Panels with Practical Loading," *Computers and Structures*, Vol. 52, No. 6, 1994, pp. 1107-1118.

78. Tripathy, B. and Rao, K.P., "Stiffened Composite Axisymmetric Shells--Optimum Lay-Up for Buckling by Ranking," *Computers and Structures*, Vol. 46, No. 2, 1993, pp. 299-309.

79. Williams, F.W., Kennedy, D., Butler, R. and Anderson, M.S., "VICONOPT: Program for Exact Vibration and Buckling Analysis or Design of Prismatic Plate Assemblies," *AIAA Journal*, Vol. 29, 1991, pp. 1927-1928.

80. Stroud, W.J. and Anderson, M.S., "PASCO: Structural Panel Analysis and Sizing Code, Capability and Analytical Foundations," NASA TM-80181, 1981.

81. Bushnell, D., "PANDA--Interactive Program for Minimum Weight Design of Stiffened Cylindrical Panels and Shells," *Computers and Structures*, Vol. 16, No. 1-4, 1983, pp. 167-185.

82. Vanderplaats, G.N., "CONMIN--a FORTRAN Program for Constrained Function Minimization," NASA TM-X-62-282, 1975.

83. Vanderplaats, G.N., "ADS--a FORTRAN Program for Automated Design Synthesis, Version 3.00," *Engineering Design Optimization*, Santa Barbara, CA, 1987.

84. Goldstein, D.E., *Genetic Algorithms in Search, Optimization, and Machine Learning*, Addison-Wesley Publishing, 1989.

85. Kogiso, N., Watson, L.T., Gürdal, Z. and Haftka, R.T., "Genetic Algorithms with Local Improvement for Composite Laminate Design," *Structures and Controls Optimization*, ASME AD, Vol. 38, 1993, pp. 13-28.

86. Nagendra, S., Jestin, D., Gürdal, Z., Haftka, R.T. and Watson, L.T., "Improved Genetic Algorithm for the Design of Stiffened Composite Panels," *Computers and Structures*, Vol. 58, No. 3, 1996, pp. 543-555.

87. Rao, S.S., "Genetic Algorithmic Approach for Multiobjective Optimization of Structures," *Structures and Controls Optimization*, ASME AD, Vol. 38, 1993, pp. 29-38.

88. Hyer, M.W. and Cohen, D., "Calculation of Stresses in Stiffened Composite Panels," *AIAA Journal*, Vol. 26, No. 7, July 1988, pp. 852-857.

89. Morris, A.J., "A Summary of Appropriate Governing Equations and Functionals in the Finite Element Analysis of Thin Shells," *Finite Elements for Thin Shells and Curved Members*, Wiley, London, 1976, pp. 15-39.

90. Scordelis, A.C. and Lo, K.S., "Computer Analysis of Cylindrical Shells," *Journal of the American Concrete Institute*, Proc. Vol. 61, No. 5, May 1964, pp. 539-560.

91. Bogner, F.K., Fox, R.L. and Schmit, L.A., "A Cylindrical Shell Discrete Element," *AIAA Journal*, Vol. 5, No. 4, April 1967, pp. 745-750.

92. Zienkiewicz, O.C. and Taylor, R.L., *The Finite Element Method: Volume 2*, McGraw-Hill, 1991.

93. Reddy, J.N., *An Introduction to the Finite Element Method*, McGraw-Hill, 1993, pp. 516-520.

94. Heki, K. and Saka, T., "Stress Analysis of Lattice Plates as Anisotropic Continuum Plates," Proceedings of 1971 IASS Pacific Symposium Part II on Tension Structures and Space Frames, Tokyo, pp. 663-674.

95. Saka, T. and Heki, K., "Limit Analysis of Lattice Plates," Proceedings of 1971 IASS Pacific Symposium Part II on Tension Structures and Space Frames, Tokyo, pp. 675-690.

96. Ozaki, M., "A Practical Method for the Analysis of Space Framework Plates and Shells," Proceedings of 1971 IASS Pacific Symposium Part II on Tension Structures and Space Frames, Tokyo, pp. 699-712.

97. Noor, A.K., Anderson, M.S. and Greene, W.H., "Continuum Models for Beam- and Platelike Lattic Structures," *AIAA Journal*, Vol. 16, No. 12, Dec. 1978, pp. 1219-1228.

98. Noor, A.K. and Nemeth, M.P., "Analysis of Spatial Beamlike Lattices with Rigid Joints," *Computer Methods in Applied Mechanics and Engineering*, Vol. 24, 1980, pp. 35-59.

99. Noor, A.K. and Nemeth, M.P., "Micropolar Beam Models for Lattice Grids with Rigid Joints," *Computer Methods in Applied Mechanics and Engineering*, Vol. 21, 1980, pp. 249-263.

100. Voleti, S.R., Chandra, N. and Miller, J.R., "Global-Local Analysis of Large-Scale Composite Structures Using Finite Element Methods," *Computers and Structures*, Vol. 58, No. 3, Feb. 3, 1996, pp. 453-464.

101. Cook, R.D., Malkus, D.S., and Plesha, M.E., *Concepts and Applications of Finite Element Analysis*, John Wiley & Sons, 1989.

102. Boitnott, R.L., Fasanella, E.L., Carden, H.D. and Calton, L.E., "Impact Response of Composite Fuselage Frames," General Aviation Aircraft Crash Dynamics, SAE Publication SP-716, 1987.

103. Farley, G.L., "Energy Absorption of Composite Materials," *Journal of Composite Materials*, Vol. 17, May 1983, pp. 267-279.

104. Reddy, A.D., Rehfield, L.W., Haag, R.S. and Widman, C.G., "Compressive Buckling Behavior of Graphite/Epoxy Isogrid Wide Columns with Progressive Damage," *Compression Testing of Homogeneous Materials & Composites*, ASTM STP 808, 1983, pp. 187-199.

105. Bruhn, E.F., *Analysis and Design of Flight Vehicle Structures*, S.R. Jacobs & Associates, Inc., 1973.

106. Gerard, G. and Becker, H., "Handbook of Structural Stability: Part I - Buckling of Flat Plates," *NACA TN 3781*, July 1957.

107. Nemeth, M.P., "Importance of Anisotropy on Buckling of Compression-Loaded Symmetric Composite Plates," AIAA Journal, Nov. 1986, pp. 1831-1835.

108. Timoshenko, S.P. and Gere, J.M., *Theory of Elastic Stability*, McGraw-Hill, 1961.

109. Whitney, J.M., *Structural Analysis of Laminated Anisotropic Plates*, Technomic Publishing Co., 1987.

110. Wittrick, W.H., "Symmetrical Buckling of Right-Angled Isosceles Triangular Plates," *The Aeronautical Quarterly*, Vol. V, Aug. 1954, pp. 131-143.

111. Cox, H.L. and Klein, B., "The Buckling of Isosceles Triangular Plates," *Journal of the Aeronautical Sciences*, May, 1955, pp. 321-325.

112. Sensmeier,M.D., Griffin, O.H. Jr., and Johnson, E.R., "Static and Dynamic Large Deflection Flexural Response of Graphite-Epoxy Beams," *NASA Contractor Report 4118*, March 1988.

113. Griffin, O.H. Jr., Johnson, E.R., and Sensmeier, M.D., "Nonlinear Response of Graphite-Epoxy Wide Columns Subject to Eccentric Load," *Journal of Applied Mechanics*, Vol. 60, No. 1, March 1993, pp. 101-108.

114. Soedel, W., *Vibrations of Shells and Plates*, Marcel Dekker, Inc., 1993.

115. Holland, J.H., *Adaptation in Natural and Artificial Systems*, University of Michigan Press, Ann Arbor, MI., 1975.

116. The Boeing Company, World Wide Web home page, URL *http://www.boeing.com/*, August 1996.

Vita

Mark David Sensmeier was born on May 4, 1963 in Lafayette, Indiana and was raised in Alliance, Ohio by his parents, Paul and Susie Sensmeier. After graduating from Marlington High School in May 1981, he attended Purdue University and graduated in May 1985 with a Bachelor of Science in Aeronautical and Astronautical Engineering with Highest Distinction. In September 1985, he enrolled in the Engineering Science and Mechanics graduate program at Virginia Polytechnic Institute and State University to pursue a Master's Degree. He completed studies at Virginia Tech and a three month residency at NASA Langley Research Center in Hampton, Virginia, as part of the NASA-Virginia Tech Composites Program. From June 1987 through May 1993, he worked as an Advanced Materials Behavior Engineer in the Engineering Materials Technology Laboratories at GE Aircraft Engines in Evendale, Ohio. In May 1993, he re-enrolled in the Engineering Science and Mechanics graduate program at Virginia Tech to pursue a Doctoral Degree.

Mr. Sensmeier has been married to the former Laura Ann Allison of Winchester, Tennessee since May 23, 1987. They have one son, Steven Kelso, who was born in 1991.